Stability Assessment of Salt Cavern Roof Beam for Compressed Air Energy Storage in South-Western Ontario

by

Mohammad Mahdi Fazaeli

A thesis
presented to the University of Waterloo
in fulfillment of the
thesis requirement for the degree of
Master of Applied Science
in
Civil Engineering

Waterloo, Ontario, Canada, 2017

AUTHOR'S DECLARATION

I hereby declare that I am the sole author of this thesis. This is a true copy of the thesis, including any required final revisions, as accepted by my examiners. I understand that my thesis may be made electronically available to the public.

ABSTRACT

Due to the intermittent nature of renewable energy sources, application of energy storage systems is an important part of the development in support of clean technologies. Compressed Air Energy Storage (CAES) plants can provide utility scale storage by compressing air into a reservoir during off-peak period and generating electricity by expanding the air when energy demand is high. CAES is a proven technology that offers various services to the power network and provides flexible load management; however, site selection is a critical step during the design process of a plant.

Salt deposits are recognized as potentially suitable geological layers for a compressed air energy storage system. In south-western Ontario, salt beds of the Salina Group of the Michigan basin provide suitable salt deposits for the excavation of storage caverns. Only two salt beds of the Salina Group are thick enough for excavation of a cavern, these are known as the unit A2 and unit B salt beds.

In the case of an underground storage system, stability and serviceability of the storage cavern must be investigated using geomechanical models. Geomechanical issues may cause serious damage to the cavern, which could stop the system from functioning. The stability of the cavern roof layer has been investigated using voussoir beam theory. This method has been widely used to model rock mass behavior around underground openings. The results of the analytical solution have been validated against an existing case and verified by using a Universal Distinct Element Code (UDEC). The stress distribution within roof beams is investigated and upper and lower limits of roof size have been determined. Based on the findings from numerical analyses, assumptions of the voussoir method oversimplify the problem and cause inaccurate results. Hence, the selected iterative solution has been modified using a nonlinear approach.

The updated procedure significantly enhanced the consistency of the results obtained from analytical solution with numerical models. To demonstrate validity of the modifications, a systematic parametric study has been included by using a wide range of beam parameters. The impact of creep behavior of the roof beam was examined by adding the deformation due to steady state creep to the elastic response of the beam. Also, the effect of the pressure difference around the cavern roof has been examined to determine maximum and minimum pressure inside the cavern with respect to size of the roof layer.

ACKNOWLEDGEMENT

I gratefully acknowledge financial support by the Natural Sciences and Engineering Research Council (NSERC) of Canada. I would like to thank my advisors, Dr. Maurice Dusseault and Dr. Dipanjan Basu for their support.

TABLE OF CONTENTS

LIST OF FIGURES

LIST OF TABLES

CHAPTER 1 – Compressed Air Energy Storage; Overview and Concepts

1.1 Introduction

Energy storage technologies allow a system to generate energy at one time and use at another. They can provide different types of services to increase the efficiency of a network. For these technologies to be effective cheap off-peak electric energy (when available) can be used to run the storage system and during the on-peak period, when the price is high, the stored energy is sold to the network. Storage capability allows better utilization of renewable energies such as wind and solar power based on their availability. Due to the intermittent nature of the renewable energy sources, energy storage services can become an important key element for the stability and reliability of the power network. Other than price arbitrage and peak shaving, storage systems can provide the grid operators with ancillary services including, regulation, spinning reserve and voltage support.

Energy storage technologies can be divided into seven categories: fossil fuel storage, mechanical, thermal, chemical, biological, electrical and electrochemical storage systems. Among these methods, electrochemical storage (such as flow and rechargeable batteries), thermal storage (such as solar pond and molten salt storage) and mechanical storage (such as pumped-hydro power plant, flywheel and compressed air energy storage) are the most popular type of storage. In order to find the best option for utility scale storage, several factors must be taken into account including efficiency, environmental impact, lifetime, economics, space and required material such as turbomachinery.

Among all the developed technologies, compressed air energy storage (CAES) and pumped-hydro power plants are well established and they can provide significant energy storage (in the thousands of MWhs) at relatively low costs. CAES has high flexibility and efficiency for load management at utility and regional levels; however, it has certain limitations of geographic location and is not a simple system like batteries. It stores large quantities of low-cost off-peak energy in the form of compressed air and generates on-peak electricity by expansion of preheated air. Design of a CAES plant needs a deep understanding of electrical, thermodynamical and geomechanical aspects of the system. One of the key elements is design of a suitable underground reservoir for storing the compressed air, which depends on the site geological characteristics. This study focuses on the stability assessment of underground caverns for a CAES project in south-western Ontario, Canada.

In this chapter, the concept of CAES, advantages, limitations and potential sites are described. Then, the characterizations of the desired site in south-western Ontario are discussed.

1.2 Compressed Air Energy Storage (CAES)

CAES is a proven technology that can provide utility scale storage for long duration with fast amp rates. CAES uses off-peak electricity to compress and store ambient air in a reservoir under or above ground. During the on-peak period, the compressed air is used to charge the turbines and generate electricity. The compressed air has high temperature, which can involve thermal limitations with potential for damage to storage reservoirs. Therefore, it must be cooled before storage. On the other hand, when air is withdrawn, it must be heated before going to turbines to provide enough heating value. If heat can be retained during compression to reheat the air during expansion, efficiency of the plant noticeably increases. This is called adiabatic storage, in which heat can be stored in a solid such as stone or fluid such as hot oil. Although, it is easier to burn fuel such as natural gas to heat the compressed air, it decreases the thermal efficiency to lower than 60%. This method is called diabatic storage, in which heat goes into the atmosphere as waste. Figure 1.1 illustrates a typical CAES plant design concept.

CAES was first investigated in the 1970s, to meet peak demand while maintaining constant capacity factor in the nuclear power industry. The first and longest CAES plant in the world has been operated in Huntorf, Germany. The other plant that has been successfully built is a 110 MW_{ac} plant near McIntosh, Alabama, USA. Several CAES projects in other countries have been started but not completed for technical and nontechnical reasons.

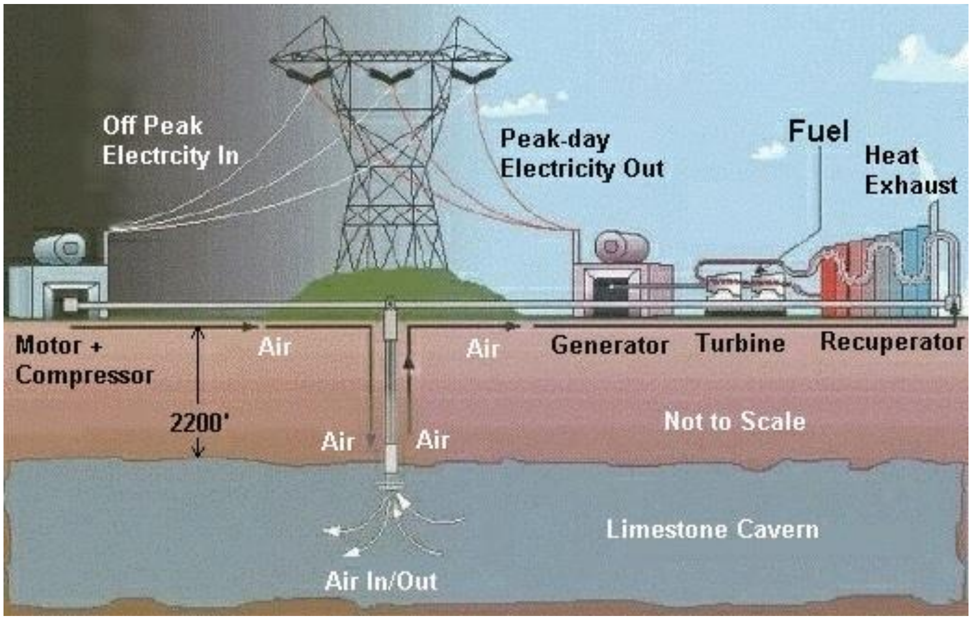

Figure 1.1 Typical Compressed Air Energy Storage Plant (Technology Insights, 2003)

The compressed air can be stored in an underground reservoir or aboveground gas pipes or pressure vessels. Aboveground CAES can be useful for short periods of time with low capacity, while underground reservoirs provide the network with long storage and higher volume capacity. In case of underground storage, location of the plant depends on a suitable geological formation. It must have enough depth to ensure safety and required air pressure while excavating is feasible and economical. Also, risk of air leakage and reaction of minerals with air must be minimal. Salt, impervious and hard rocks and porous rocks such as porous rock aquifers and depleted gas or oilfields are suitable sites for air storage.

Salt formations have been used for storage and waste disposal for many years. Rock salt has very low permeability. It shows visco-elasto-plastic behavior and has the ability of self-healing, which closes all the joints and cracks. These features make salt beds and domes suitable for CAES with minimal risk of air leakage. The compressed air in both Huntorf and McIntosh CAES plants is stored in salt domes.

Compressed air energy storage systems have multiple advantages, which make them more suitable option for the grid than other technologies.

- CAES can provide large scale energy storage (in the hundreds to thousands of MWhs) at low costs.
- It is a commercial system that has been operated successfully in two different sites.
- CAES provides a flexible system that can be optimized based on the grid conditions and economics at each site.
- Fast startup time in a CAES system provides utility engineers with flexible load management as the maximum capacity can be reached within a few minutes.
- For underground storage, a small area on the surface is required and has minimum impact on the environment.

Moreover, in comparison with similar technologies such as pumped-hydro plant, CAES provides significant advantages during the operation but they are not in the scope of this research. In spite of the numerous CAES advantages, it is not widely used by energy storage and green-tech companies. One reason is geography and locational limitation and also lack of awareness of its economic and technical feasibility. Key features and charging and discharging characteristics of CAES are summarized in Table 1.1and Table 1.2 (Based on the 110 MW_{ac} McIntosh Plant).

Table 1.1 Key CAES Features (Technology Insights, 2003)

Feature	Parameter Range
Space requirements	100-MW_{ac} plant needs about 1 acre
Effective Efficiency	85%
Life	30 years
Maintenance requirements	Same as simple cycle combustion turbine
Environmental impact	Minimal (NO_x is below 5 ppm)
Auxiliary equipment needs	Water if wet cooling is used; no water if dry cooling fans are used
Power conditioning needs	None

Table 1.2 Typical Charging and Discharging Characteristics (Technology Insights, 2003)

Characteristic	Charging (Compression Mode)	Discharging (Generation Mode)
Electrical energy input	0.75 kWh input for every 1 kWh of output	N/A
Heat consumption with fuel	N/A	4,100 Btu/kWh of the net plant output
Storage capacity	1,950 MWh	2,600 MWh
Response time, standby to full power	4 minutes	Nominal: 10-12 minutes Emergency: 5-7 minutes
Response time	Approx. 20 minutes	N/A

Underground storage in geological layers might be considered as risky and precarious by utility engineers. In addition, site selection is limited and critical, which makes CAES feasible at specific locations with suitable geological formations. Another limitation of CAES is that it cannot be mass-produced. CAES plants must be individually designed, operated and developed.

Other than Huntorf in Germany and McIntosh in Alabama, several CAES plants have been initiated but not completed, such as a 1,050 MW_{ac} plant using salt formations in the Donbas area of Russia/Ukraine or a 100 MW_{ac} plant using a hard rock cavern in Luxembourg. There are several other ongoing CAES projects such as Norton plant in Ohio or Matagorda plant in Texas. In Canada, a pilot plant has been initiated in south-western Ontario (at Goderich area) using salt caverns. These caverns were already excavated for salt production and abandoned. The salt cavern will be able to store enough electricity to power around 1,000 homes and was commissioned by Ontario’s government-owned electrical system operator (Hydrostor Inc. and NRstor Inc., 2017).

1.3 Geomechanics of CAES

In order to develop an underground CAES project, a systematic geological and geomechanical analyses are required to ensure stability and serviceability of the storage reservoir. The strength and constitutive response of geological materials, in-situ stresses and permeability are crucial factors in design of storage caverns. Therefore, various field tests such as hydraulic/hydrofrac testing are required. For instance, many core samples were extracted and analyzed to determine the salt characteristics during development of the McIntosh plant. Geomechanical issues limit cavern size, shape, spacing, and operating pressures. Thus, geomechanical models based on geological data are inevitable.

Both Huntorf and McIntosh plants use solution-mined cavities in salt domes as their storage reservoirs. Salt domes provide large volume with lower risk of instabilities during operations. For most of salt formations, solution mining techniques can be applied to create the caverns. This is a reliable, low cost route for developing a storage volume of the required size; however, providing adequate supply of fresh water and brine disposal are serious issues. Salt deposits are the primary options for storage and waste disposal plants. Due to the specific characteristics of rock salt, salt deposits are the most suitable formations for CAES plants. The key characteristics of rock salt can be summarized as

- Very low permeability; an impervious stratum such as salt can seal the reservoir and keep the compressed air with no leakage.
- Ability of self-healing; healing (or annealing) mechanisms can reverse the damage process and interconnect fracture surfaces and close micro-fractures.
- Simple mining operation; salt can be excavated using regular drilling techniques.
- Relatively high thermal conductivity; rock salt has a high thermal conductivity that leads to rapid heat dissipation via conduction.
- Wide geographic distribution; salt formations can be found at many locations

1.3.1 Domes and bedded salt formations

Storage caverns can be excavated in both salt beds and domes; however, creating a cavern in salt domes is more convenient. Salt domes are diapir-shaped structures created due to upward movement of evaporite minerals into surrounding rocks. It is caused by buoyancy due to lower density of salt and its plastic behavior at high pressure and temperature. During deformation, brine within the salt crystals is squeezed out. This process leads to relatively low water content. The center part of the diaper is more deformable; whereas, rock mass laminations around the edges of the diapir are carried along upward and broken during the migration of salt (Hansen et al., 2016). Domes usually provide more storage volumes with less risk of instability.

In contrast, salt beds are thin and laterally extensive deposits, which have not been affected by tectonic deformations. Therefore, bedded salt tends to contain higher water content, which leads to lower strength and faster creep rate than domal salt. Salt beds usually have high concentration of impurities. Design of a cavern in salt beds could be troublesome since large caverns need long aspect ratio which could cause roof stability issues. Moreover, salt beds often contain non-salt inter layers that could collapse into the caverns and lead to volume loss and instability (Succar and Williams, 2008).

1.3.2 Natural gas and compressed air storage

The process of air storage in salt caverns causes some geomechanical issues regarding to cavern stability, such as cavern shrinkage and roof layer instability. There are currently many gas storage in operation around the world. Thus, there is a good understanding of geomechanical design of natural gas storage cavities; however, there are several differences between gas and compressed air storage in salt caverns. These differences make the geomechanical design of a CAES plant more critical.

The first reason is the cyclic loading due to compression and expansion of air in CAES is a multiple of turnover between gas injection and withdrawal in the gas storage system. During summer, gas would be injected into the caverns and during winter, when energy is required, it would be extracted from the caverns. In CAES systems, compression and decompression of air takes place based on the on and off peak hours in a day. In this condition, the inside pressure of the salt cavern goes up and down with higher frequency.

This process strongly affects creep behavior of salt, as deviatoric stresses change with pressure.

The maximum cavern pressure must be kept less than in-situ stresses around the cavern to avoid fracturing; however, it is usually set in reference to the capacity of the turbines. For deep caverns, even high pressures inside the cavern do not make any stability issue but turbine input pressure is limited. In a natural gas system, high pressure gas can be stored in the cavern and only needs to be decompressed at the input side of the turbine to meet the conditions. Since natural gas has a high energy content, loss of energy due to expansion is negligible. In contrast, decompression of air before charging the turbine causes loss of energy and efficiency. Therefore, the inside pressure of the cavern for a CAES plant is usually lower than the cavern pressure for a natural gas storage system. Lower inside pressure leads to higher deviatoric stress and creep rate. This process causes cavern closure that might cause surface subsidence or significant cavern volume loss.

The compression and decompression of air is accompanied with temperature fluctuations in the cavern. The change of fluid temperature is given approximately by 1.3° per bar pressure (Düsterloh and Lux, 2010). Heating and cooling of rock salt induce thermal compressive and tensile stresses, respectively. Long periods of storage in natural gas systems allow heat transmission between gas and rock salt, which reduces thermal induced stresses. Whereas, frequent injection and withdrawal in a CAES plant causes significant thermal induced stresses in surrounding rocks.

1.3.3 Geomechanical parameters

Geomechanical design parameters strongly affect stability, serviceability and tightness of the storage reservoir as well as surface subsidence due to excavation. The goal of the geomechanical modeling is to take different parameters into account to design a stable and operative storage cavern. The design parameters can be summarized as

- Depth of the cavern (regarding pressure and temperature gradient)
- Cavern geometry and volume (including height and diameter)
- Minimum and maximum pressure inside the cavern
- The distance between storage caverns (cavern spacing)
- The distance between caverns and geological interfaces
- Convergence of salt cavern (due to rock salt creep)
- Operation pattern (frequency of cycles and rate of injection and withdrawal)
- Rock salt damage (due to high stress concentration)
- Span to thickness ratio of cap rock layer and non-salt interlayers

Prediction of the impact of these factors on the response of salt caverns is necessary. For this purpose, empirical, analytical and numerical methods have been applied. Since rock mass behavior cannot be explicitly defined, correlation between parameters that affect rock mass response should be investigated. All assessment methods are based on these effective parameters, such as geological and mechanical properties. The analytical methods use theory to show which explicit parameters influence opening stability, while empirical methods through rock mass classification and experience use implicit parameters to define the explicit parameters in an attempt to represent the factors influencing the opening stability (Capes, 2009).

1.4 Site characteristics

In order to investigate the mechanical response of a salt cavern, geology and in-situ stress field and constitutive laws of materials must be determined. Therefore, a combination of data from rock mass classification, numerical modeling, observations, and case histories are required.

1.4.1 Site geology in south-western Ontario

Several salt basins cover a large area of North America (Figure 1.2). Salt deposits in south-western Ontario are located on the east margin of the Michigan Basin. The Michigan Basin forms a bowl-shaped structure. The center part of basin is deep and thick, whereas, it is shallow and thin on the edges. Michigan Basin contains two groups of salt beds: the Salina Group and Detroit River Group. Salina Group salt beds are relatively continuous and extensive. They are thick (900 m thick) at the center part of the basin and thin on the edges. In contrast, the younger salt beds in the Detroit River Group are relatively thinner (450 m thick) and are less geographically widespread.

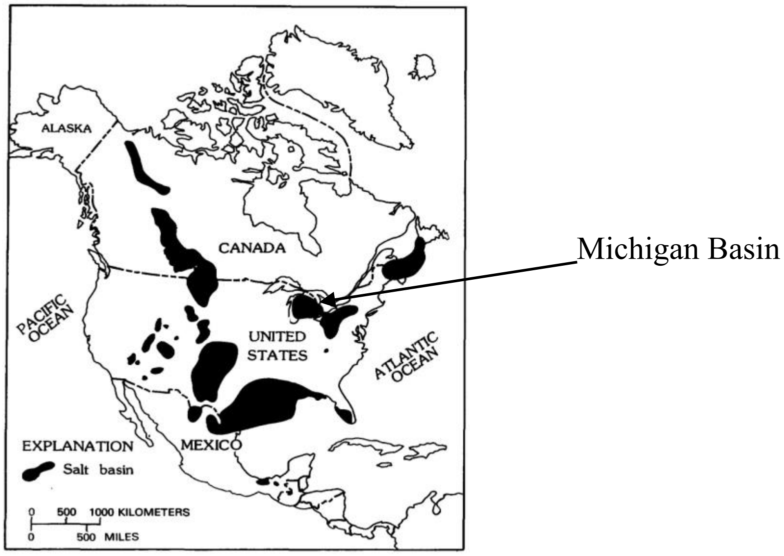

Figure 1.2 Major salt basins of North America (Ege, 1984)

The Windsor, Chatham, and Sarnia-Goderich areas are three main areas of south-western Ontario underlain by salt. Salt beds of this region belong to Salina Formation of Silurian age. Depth and thickness of salt beds varies from site to site. The uppermost salt beds are found approximately $270 - 490\ m$ below the surface. The shallowest salt beds are found at Kincardine at $270\ m$ depth (Hewitt, 1962). Figure 1.3 illustrates a typical geological section of the Salina Formation in south-western Ontario.

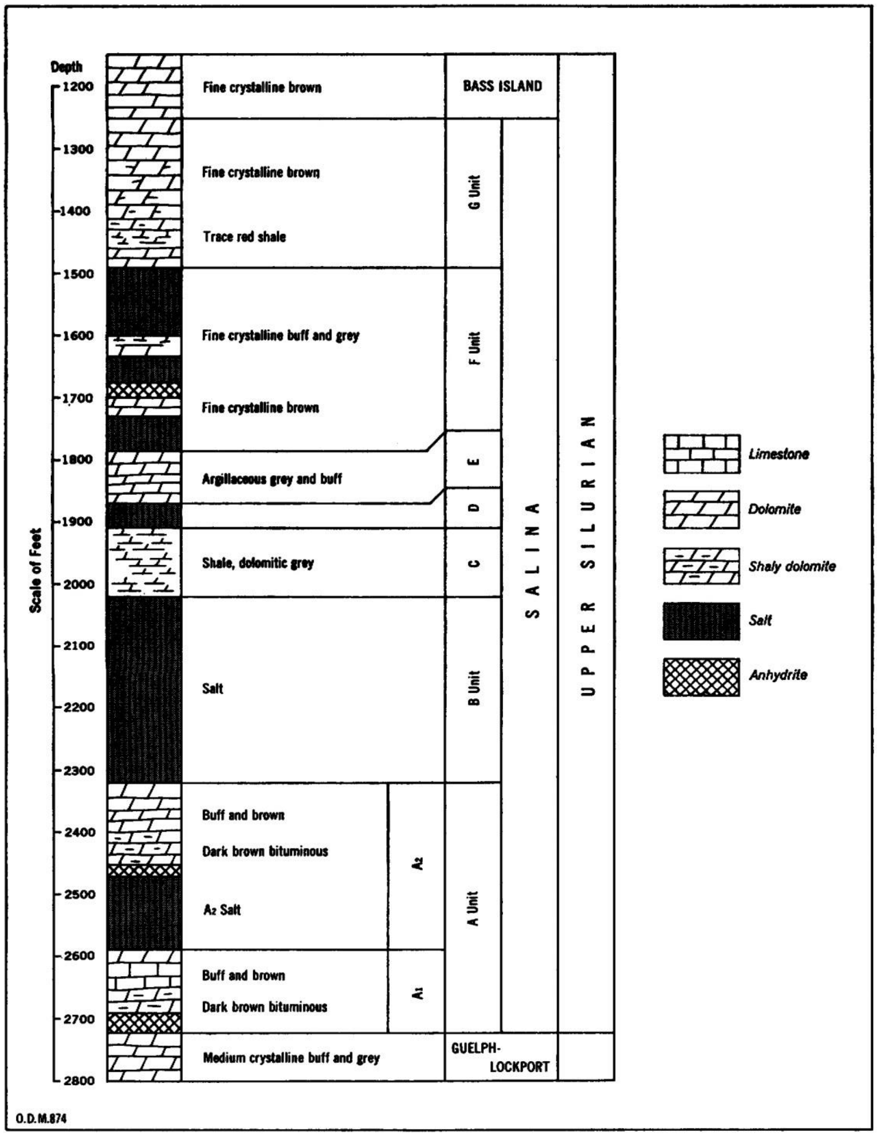

Figure 1.3 Generalized columnar geological section of the Salina Formation (Grieve, 1955)

The Salina Formation is divided into seven lithological units (A to G), in which unit A is the oldest and unit G is the youngest deposit (Landes, 1945a). It must be noted that unit A is also subdivided into A1 and A2 parts with similar properties. Each unit has different thicknesses (from $15m$ to $90m$) and various minerals (such as salt, shale and dolomite). Table 1.3 summarizes the characteristics of each unit.

Table 1.3 Subdivisions of the Salina formation (Hewitt, 1962)

Formation	Unit	Description
Upper Salina	G	Fine crystalline brown dolomite, shaly dolomite, some anhydrite, red shale (no salt)
	F	Thick beds of salt separated by shaly and fine crystalline dolomite
	E	Thin layer of dolomite (no salt)
	D	Mainly pure salt
	C	Dolomatic grey shale (no salt)
	B	Thickest unit, mainly salt with thin dolomite layers
Lower Salina	A2	Fine to medium grey dolomite; dark bituminous shale; lower part contains a thick layer of salt
	A1	Fine to dense, grey to dark dolomite with dark-grey bituminous shale; Anhydrite at base

Salt beds in the Sarnia-Goderich area are the most widespread salt deposits in Ontario. As Table 1.3 indicates, salt can be found in units A2, B, D and F. Due to shallow depth of unit D and F, they are not desired for a CAES plant, as the required maximum inside pressure cannot be provided. Also, since unit D is very thin and salt deposits in unit F are separated, only unit A2 and B provide a suitable location for excavation. Therefore, unit

A2 and unit B in both Sarnia and Goderich sites have been selected for implementation of CAES system. The Goderich site is spread closer to the edge of the basin and salt beds are relatively thinner. According to Hewitt (1962) unit B salt beds in Sarnia have the greatest thickness ($90m$) while A2 unit in Goderich is the thinnest salt bed ($25m$). Thickness and depth of each unit is summarized in Table 1.4.

Table 1.4 Depth and thickness of the potential deposits for CAES in south-western Ontario (Hewitt, 1962)

Formation	Site	Salt unit	Top depth (m)	Bottom depth (m)	Thickness (m)
Salina	Sarnia	B	610	700	90
		A2	750	790	40
	Goderich	B	390	460	70
		A2	510	535	25

1.4.2 Rock mass classification

The behavior of a rock mass is governed by its properties and the condition that rock mass is exposed to, such as in-situ stress. A rock mass is extensively dominated by various joint sets. Therefore, properties of rock material and joints are both critical in rock mass assessment. Overall, in the design process of an underground excavation, three types of parameters must be taken into account: 1) material parameters, such as elastic modulus and strength; 2) joint parameters, number of joint sets, spacing and orientation; and 3) boundary conditions, such as in-situ stress and groundwater pressure.

Among all influencing factors, degree of jointing, joint friction and stress are the most important factors on rock mass stability. Degree of jointing represents the joint patterns, while joint friction strongly depends on joint roughness, thickness and type of mineral filling. Stability also depends on the magnitude of vertical stress due to overburden and tectonic stresses due to topography with respect to rock strength (www.ngi.no).

Rock mass classification systems are useful to estimate rock mass characteristics and provide a simple scheme to understand the rock mass quality using quantitative data. They have been widely used as engineering design aid in underground construction projects. They can provide input data for analytical and numerical methods during design process. There is not enough information on properties and conditions of rock mass at early stages of a project. Therefore, classification systems must be updated with site investigations. Classification systems can be qualitative (descriptive), such as GSI (Geological strength index) and Rock Load systems or quantitative, such as Rock Mass Quality (Q), Rock Mass Rating (RMR) and Rock Structure Rating (RSR) systems.

1.4.2.1 The Q-system

Barton et al. (1974) introduced Q-system as an index for evaluation of the tunneling quality of rock mass. It was initially developed based on extensive case history analyses of underground excavation stability. The Q-system has been widely used for classification of the rock mass around an underground opening, field mapping and as a guideline in rock support design process (www.ngi.no). It also provides a first-order assessment of the stability of an underground opening in jointed rock mass. High Q values indicate good stability of the excavation, whereas low values give poor stability. The numerical value of the index varies from 0.001 to 1000 and can be calculated by

$$Q = \frac{RQD}{J_n} + \frac{J_r}{J_a} + \frac{J_w}{SRF} \tag{1.1}$$

where RQD is the rock quality designation, J_n is the joint set number, J_r is the joint roughness number, $J_a$is the joint alteration number, J_w is the joint water reduction factor, and SRF is the stress reduction factor.

The Q index depends on six parameters that are determined by geological mapping or core logging and using tables that assign numerical values to different situations. These parameters can be divided into three main factors: 1) degree of jointing ($\frac{RQD}{J_n}$), which represents structure of the rock mass and measures block size; 2) joint friction ($\frac{J_r}{J_a}$) representing inter-block shear strength which depends on roughness and frictional characteristics of the joint walls or filling materials; and 3) active stress ($\frac{J_w}{SRF}$) is an empirical factor describing active stress parameters using water pressures and flows and in situ stress state.

The value of RQD is calculated as percentage of sum of the length of all core pieces more than $10\ cm$ long with respect to the total core length (between 0 and 100). The value of J_n represents joint set number but it is not exactly same as the number of joint sets. It can take a value between 0.5 and 20. The value of J_r depends on joint wall surfaces, infill and orientation and it can have a value between 0.5 to 4. The value of J_a is strongly dependent on thickness and strength of joint infill (between 0.75 and 20). The inverse tangent of the value of $\frac{J_r}{J_a}$could estimate the actual friction angle for various combinations of wall roughness and joint infill materials.

In addition, the value of J_w can be calculated based on inflow and water pressure in underground openings. Water within joints can soften or wash out the mineral infill and reduce friction. It must be noted that water pressure causes reduction of normal stress and leads to higher risk of shear failure. It takes values between 0.05 and 1, while a low value leads to serious stability issues. Stress reduction factor (SRF) describes the relation between stress and rock strength around an opening. It can be obtained using the ratio of rock uniaxial compressive strength (UCS) to major principal stress (σ_1) or the ratio of maximum tangential stress (σ_θ) to UCS. Tables that indicate numbers of each parameter can be found in any reference regarding rock mass classification and properties.

Using the Q-system one could evaluate dimensions of underground opening and safety requirements for support design. Numerous empirical correlations have been proposed to determine other decisive factors of rock mass, such as correlations for deformation modulus (E_m), Poisson's ratio (ν), friction angle (ϕ_m) and cohesion (C_m) of the rock mass.

1.4.2.2 Rock mass properties

Salt beds of unit A2 and B in Sarnia and Goderich are the most suitable options for CAES in Ontario. Each unit contains different minerals and has different mechanical properties. Therefore, data from field mapping and core logging tests are required. Table 1.5 summarizes some of properties of the desired geological layers. These data are mainly obtained from core logging, field and laboratory testing and published by Intera Engineering Ltd. (2011). The purpose of their geoscientific characterization study was to investigate feasibility of implementation of a deep geologic repository for a Low and Intermediate

Level Waste (L&ILW) disposal plant in south-western Ontario; however, the collected geoscientific data can be used for design of a cavern for CAES system.

Table 1.5 Summary of the rock mass properties (Intera Engineering Ltd., 2011)

Parameter	Value				Unit
	Unit A2 evaporite	Unit A2 carbonate	Unit B evaporite	Unit B carbonate	
Bulk density, $\rho_{b_{wet}}$	2,710	2,680	2,800	2,560	$\frac{kg}{m^3}$
Uniaxial compressive strength, UCS	$-$	60×10^6	$-$	8×10^6	Pa
Crack initiation	$-$	45	$-$	32	$\%UCS$
Crack damage	$-$	80	$-$	44	$\%UCS$
Young's modulus, E	$-$	23×10^9	$-$	3×10^9	Pa
Poisson's ratio, ν	$-$	0.2	$-$	0.4	$-$
Rock quality designation, RQD	96	96	97	97	%
Natural fracture frequency, NFF	0.4	0.4	0.5	0.5	m^{-1}

These data are considered as the inputs in models and solutions developed in this study. The density of overburden is assumed to be $2{,}600\ \frac{kg}{m^3}$ and vertical stress can be calculated depending on the depth of each layer as follows

$$\sigma_v = \rho g h \tag{1.2}$$

In order to assess stability of the roof layers, deformation modulus, E_m, and strength of the rock mass must be determined. Uniaxial compressive strength, UCS, of the carbonates on top of the salt beds can be found in Table 1.5; however, to calculate deformation modulus, the value of Q-index must be determined for both unit A2 and unit B roof beds. It is reasonable to assume three joint sets cutting through laminations in the rock mass, which leads to $J_n = 9$. Also, joint wall surfaces are assumed to be rough, undulating and unaltered ($J_r = 3$ and $J_a = 1$). When formation pressure is high around an underground excavation ($> 1\ MPa$), then joint water reduction factor, J_w , is approximately 0.2. Depending on the ratio of rock uniaxial compressive strength to major principal stress, the stress reduction factor, SRF, would be in range of 5 to 50 for unit A2 and 200 to 400 for unit B carbonate layers. The value of Q-index can be calculated using equation (1.1). It is 0.0427 for unit A2 and 0.0054 for unit B carbonates, approximately.

The value of deformation modulus can be determined using the correlation proposed by Barton (1995)

$$E_{rm} = 10 \times Q^{1/3} \tag{1.3}$$

Replacing the values of Q in equation (1.3), gives the values of $3.5\ GPa$ and $7.75\ GPa$ for unit A2 and unit B carbonates, respectively. It must be noted that for parameters without field data, conservative values have been assumed to ensure the reliability of stability analyses. Knowing the deformation modulus, the joint normal stiffness can be obtained by following equation (Barton, 1995).

$$k_n = \frac{E_i E_{rm}}{S_j (E_i - E_{rm})} \tag{1.4}$$

where k_n and S_j are the joint normal stiffness and spacing. Also E_i and E_{rm} represent intact rock and rock mass modulus, respectively.

CHAPTER 2 – Analytical Design Methods

Analytical design methods study the possibility of the stress driven and gravity driven failures around underground excavations. These methods are based on the relationship between stresses and rock mass properties. For gravity driven failure, joint properties such as tensile strength and joint spacing and orientations are the most critical parameters for design considerations. Intact rock behavior is controlled by applied stress state and rock strength. It must be noted that each method is based on some assumptions. Therefore, results need to be validated against field data (Shabanimashcool, 2012).

Upon removal of rock during excavation, load is carried by rock in other zones which creates zones of high stress concentration. Gravity driven failures may occur due to gravitational load depending on the local stress field, rock mass classification, and orientation of bedding planes. Therefore analysis of the stability of the underground opening is required. It consists of kinematic wedge failure, beam and plate buckling analysis and voussoir beam analysis (Capes, 2009). Analysis of the stress driven failure includes failure criteria such as Mohr-Coulomb, and Hoek-Brown. Although Mohr-Coulomb criterion is best way to describe the physics of the problem, it could lead to conservative predictions as the intermediate stress is ignored. The input parameters of Hoek-Brown criterion are more consistent with rock mass properties. On the other hand, a 3D criterion such as Mogi–Coulomb criterion seems to give a proper accounting of the strengthening effect of the intermediate stress (Al-Ajmi & Zimmerman, 2006).

Empirical methods along with statistical analysis are very important in rock mechanics. These methods are based on the experience and consider the most critical parameters on stability of domain, such as stress field, mechanical properties of rock and joints and geometry of the excavations. Since the results are strongly dependent on engineering skills including knowledge, observation, and interpretation, they must be validated against the field data to check the applicability of the methods. Also, these methods are based on the data obtained from specific sites. Therefore they might be unreliable for design analysis in other sites. In this chapter, analytical design methods for gravity driven failures are presented.

2.1 Kinematic Analysis

The rock medium around an excavation is always cross-cut by different joint sets. Intersection of joints may create wedge geometries which can be potential zones of failure. If the gravitational load is greater than the resisting force due to cohesion and frictional strength between joint walls, small zones wedges among joints would fall from the stope wall. Existence of faults could lead to similar process of failure; however, in this case, large scale failures are expected. Kinematic wedge analysis investigates the potential zones of failure due to joint intersections.

2.2 Beam Failure and Plate Buckling Analysis

Obert and Duval (1967) thoroughly studied beam failure and plate buckling analysis. Their studies have been widely used in civil engineering for design and stability assessment of tunnel roofs. The medium is considered as continuous, homogeneous, isotropic, and linear elastic. In this condition, deformation of the beam and plate can be determined by analyzing the effect of gravitational load, geometrical parameters and mechanical coefficients. Since many joints cut through bedding planes, the medium usually consists of different blocks which make it discontinuous. Also existence of joints would reduce or completely eliminate the tensile strength of rock mass. This is against the assumption of beam and plate analysis that considered a continuous medium with tensile strength. Therefore, conventional methods are incapable of modeling the rock mass behavior (any jointed rock mass) around an underground opening.

2.3 Rock Mass Failure Criterion

Behavior of a rock mass can be modeled using the relationship between stress field and rock strength. Failure criteria have been introduced and used by many researchers for different stress states and rock properties. These failure criteria identify the maximum stress values that the rock mass can withstand. Once the applied stress state exceeds the limit, various types of failure could occur. Compressional failure happens when minimum principal stress, σ_1, is relatively high while a low value of σ_1 leads to tensile failure.

Among the presented criteria, Mohr-Coulomb and Hoek-Brown are the most common criteria in geotechnical engineering. They simply develop a relationship between minimum and maximum principal stresses, σ_1 & σ_2, and rock strength. Mohr-Coulomb criterion can only model the behavior of intact rock or failure along one discontinuity. Hoek and Brown (1980) presented input data for design of underground excavations. Their criterion estimates the brittle failure of intact rock and models the jointed rock mass behavior. Hoek-Brown criterion modified the Mohr-Coulomb by considering a nonlinear increase in the peak strength of a rock mass.

The Mohr-Coulomb is the best way to understand the physics of the problem. The failure envelope is the response of the rock to stress state and obtained from a plot of shear strength versus normal stress. Failure occurs when stress is greater than the cohesion and frictional resistance. Tensile cutoff determines the upper limit for strength of the rock against tensile failure. The Mohr-Coulomb relation is also used to represent the residual strength which is the minimum strength reached beyond the peak (Goodman, 1989). Both criteria are based on the empirical insights and theoretical relation of lab testing on core samples.

2.4 Voussoir Beam Analysis

In a rock mass surrounding an underground excavation, different joint sets always crosscut the bedding planes and laminations. These joints allow tensile stresses to develop in the rock mass. In this condition, tensile stresses create new cracks or extend other joints. Conventional beam and plate theories cannot model the behavior of a discontinuous rock mass. Voussoir beam theory has been commonly used for stability assessment of excavations where the joints are almost perpendicular to the bedding planes. In classical beam theories such as Euler and Timoshenko, the beam is assumed to be fixed at the hinges. This leads to a closed-form solution for stress and deflection analysis. In contrast, the voussoir beam method takes the effect of joints into account and lets the beam displace at the abutments or mid-span. Therefore, it is statically indeterminate. In order to solve the set of equations, a trial and error procedure must be followed or some of the unknown parameters must be reduced.

2.4.1 Concepts and background

Bedding planes usually cut through the stratified rock mass and coincide with the immediate roof and floor of the excavation (Brady & Brown, 2004). The stability of the immediate roof layer is the most important factor in design of an underground excavation. These laminations can be the result of sedimentary layering, extensile jointing, fabric created through metamorphic or igneous flow processes or through excavation-parallel stress fracturing of massive ground (Diederichs & Kaiser, 1999a). Bedding planes and other discontinuity with different orientations strongly affect the response of the rock mass to the stress field.

Based on the results published by Fayol (1885), deflection of the layers on top of underground strata does not depend upon other layer's deformation. He used stacks of wooden beams to examine the deformation process of bedding planes. It was noted that gravitational load tends to be transferred laterally to the abutments rather than vertically to the lower beam. This process leads to separation of the laminations upon deflection such that the immediate roof layer only deforms under its own weight. Therefore stability of the excavation highly depends on the behavior of the immediate roof beam. The process of lateral transmission of stress is described as arching effect, which could mobilize the friction between bedding planes and decouple the rock beds above and below the arch.

Arching enables the beam to deform to some extent before failure. The moment generated by deformation compensates the moment due to gravitational load and makes the beam stable. In other words, in a confined situation the ultimate strength of the beam is larger than the strength that conventional elastic theories assume. This is the reason that classical beam theories underestimate the stability of roof layer.

Arching theories must be separated for underground cavern design into two types of arching action: the arching action by which most of the ground load above the opening is transferred to the sides, and arching action which enables the rocks in the immediate roof to span the opening (Sterling & Nelson, 1978). In theoretical analysis of the roof stability, the immediate roof behavior is more important than the behavior of a high ground arch. Although the behavior of a high ground arch is consequential in estimating the rock load that is exerted over the immediate roof, many indeterminate parameters make it too complicated for analysis. The immediate roof behavior is more important and amenable to stability analysis (Figure 2.1).

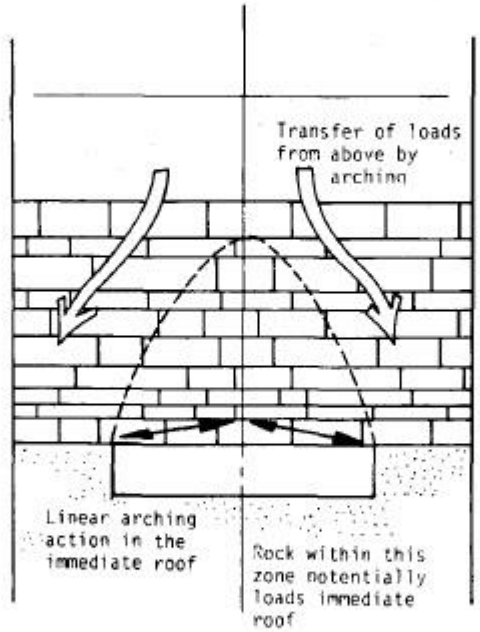

Figure 2.1 Arching action in bedded and jointed cavern roof (Sterling & Nelson, 1978)

In another attempt to understand the behavior of the roof layer, Bucky and Taborelli (1938) designed a new experiment for intact rocks. They observed that, at some stage, tensile stresses create a fracture in the middle of the beam. They increased the span of the beam and noticed that the previous fracture was closed and new fracture at mid-span was created. It was concluded that the vertical joints at mid-span control the deformation and stability of the beam. In this condition, rock mass can be considered as a discontinuous medium which consists of individual rock blocks. These blocks are called voussoirs (arch-stone) and the beam composed of voussoirs is called voussoir beam (Figure 2.2). The origin of this name comes from architecture of the ancient Rome. This term has been used to name the constituent stone blocks of an arch in masonry bridge construction.

Evans (1941) proposed the notation of the voussoir beam for the first time and organized the concepts of the theory. He solved a set of equations and investigated the relation between deflection, gravitational load and lateral thrust. Evans also established an analytical solution for roof stability assessment. The voussoir beam, in this context, is assumed to have zero tensile strength. It deforms elastically under compressive stress. When vertical joints have rough surfaces, friction can transmit the vertical load and a compressive arch structure would be generated within the beam. The arch is assumed to be confined by surrounding rocks at the abutments. For simplification, the arch zone is considered to have a constant thickness within the beam and it is equal to half of the thickness of beam. Also, the stress distribution at the abutments and mid-span forms a triangle.

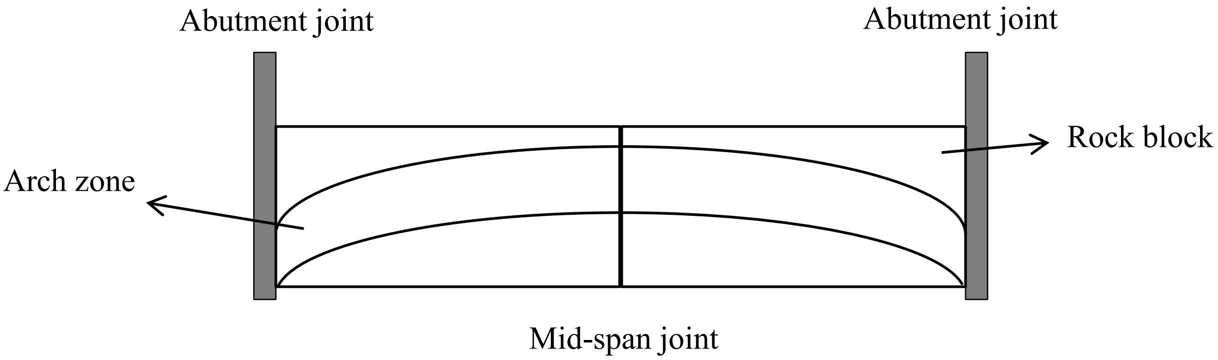

Figure 2.2 The voussoir blocks and joints

Evans pioneered a solution to investigate response of the roof layer and proposed a new method to examine rock mass behavior around underground excavations; however, he made some mistakes in the statics of the method which have been rectified by other researchers. He also oversimplified the problem by bringing unnecessary and inaccurate assumptions into the calculations. For instance, he assumed a constant large thickness for the compressive arch within the beam equal to half of the thickness; however, Beer and Meek (1982) claimed that the assumption of an identical thickness for arch at both abutments and mid-span cannot characterize the buckling criterion. Also, the assumption of a linear stress distribution at the abutments and mid-span was numerically found to be inaccurate.

Wright and Mirza (1963) examined the behavior of cracked voussoir beams using photoelastic models and claimed that the maximum compressive stress within the beam is multiple of that calculated by Evans and the thickness of the arch is less than half the thickness of the beam. Wright (1972) established physical models using limestone blocks and bricks. He also investigated the response of the beam numerically using finite element models.

Barker and Hatt (1972) conducted a two dimensional finite element model for intact and cracked roof beams. They concluded that classical beam theories give reasonable results for intact beams; while the concept of voussoir arch must be considered for cracked beams. Moreover, since voussoir theory only considers a single roof layer and does not include the interaction between roof beds, it would lead to conservative prediction of stability. It was declared that finite element analysis leads to higher and more realistic factors of safety as the effect of cohesion and interaction between roof beds are taken into account.

A constrained-beam testing apparatus was designed by Sterling and Nelson (1978) to examine the ultimate load bearing capacity of rock beams. The sample was under transverse load and deflection, lateral thrust and eccentricity of the lateral thrust were detected. Their observations proved that the behavior of the roof beam can be modeled elastically.

Figure 2.3 illustrates the vertical load-deflection curve of a limestone beam. When transverse load was applied, the intact beam deformed elastically until a tensile crack grew at mid-span, which decreased the strength of the beam. The experiment was set to increase the displacement at a constant rate. This led to drop of the load to point 2. Creation of the compressive arch enabled the beam to carry the vertical load. The cracked beam showed elastic behavior with less stiffness (point 3 to 7). Due to crushing at the abutments and mid-span, response of the beam was nonlinear from point 7 to 10. This was immediately before reaching the ultimate load capacity at point 10, which was followed by a noticeable relaxation. After this point, deflection of the beam decreased the load capacity and caused severe cracking and crushing at edges and mid-span (point 11 to 17). The ultimate failure of the beam occurred at point 17 by growing diagonal cracking.

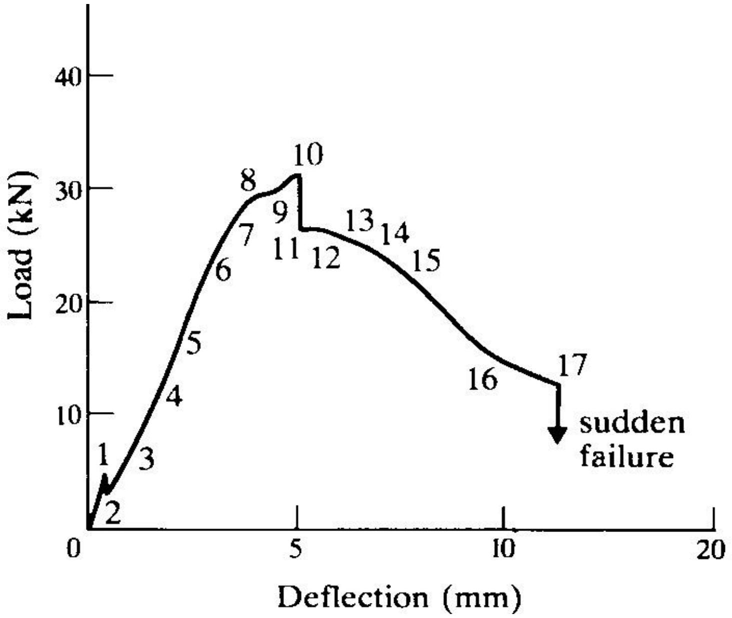

Figure 2.3 Vertical load vs. deflection (Sterling & Nelson, 1978)

Their study clarified the potential failure mechanisms in a rock bed. Sterling (1980) also investigated the impact of mechanical and geometrical parameters such as length, shape, stiffness, loading and support conditions on response of the roof beams.

Beer and Meek (1982) conducted their study based on the voussoir beam method introduced by Evans (1941) and presented design curves for safe roof beams. Also, square and rectangular roof plates were considered and the initial assumption regarding the thickness of the arch was rectified.

An iterative solution was presented by Brady and Brown (1985) based on the updated version of voussoir method published by Beer and Meek (1982). Sepehr and Stimpson (1988) also numerically verified the formation of parabolic compressive zone within the roof beams using a nonlinear finite element model. Stimpson (1989) introduced a new type of failure and called it "2-hinge" collapse mechanism. It was observed that the ultimate collapse of the immediate roof beam occurred by pivoting about two hinge zones that led to large vertical deflection of the central part of the beam (Figure 2.4).

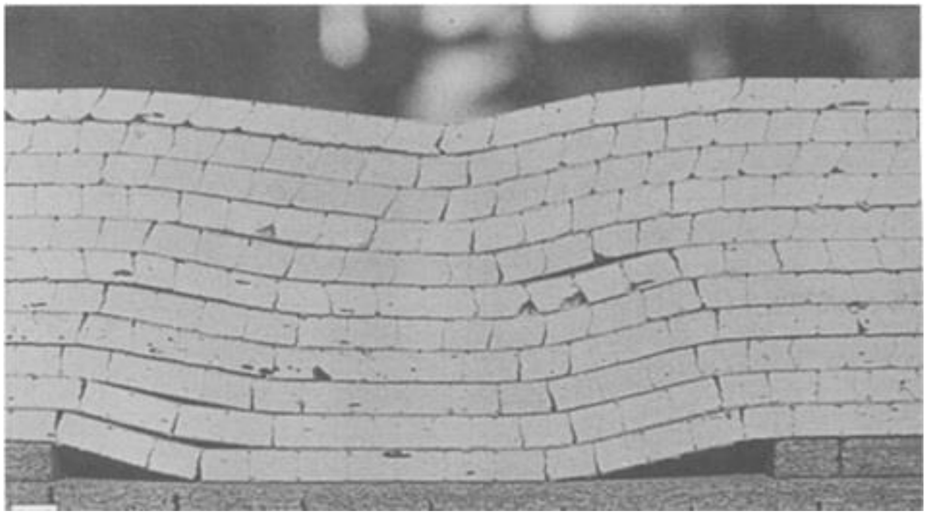

Figure 2.4 Ultimate collapse of a series of cross-jointed roof beams (Stimpson, 1989)

In this context, joint properties such as scale and distribution of roughness of the cross-joints were found to have the most impact on roof stability. The voussoir beam was assumed to be a particular case of 2-hinge mechanism; however, since this type of failure abruptly occurs when critical span is reached, it is not useful for creating stability design curves.

Passaris et al. (1993) and Ran et al. (1994) analyzed shear sliding failure mechanism in jointed roof layers. They used numerical and physical models to verify the proposed equations and investigate effects of geometry and material properties on failure. A finite element model was implemented to simulate nonlinear joints and geometries and a large scale test rig was designed to study the voussoir mechanism. It was concluded that linear analysis cannot model large displacement of the voussoir beam when a relatively high value of transverse load is applied. In this condition, axial thrust must be obtained by a nonlinear function of the transverse load and material geometrical properties.

Following the voussoir method revised by Brady and Brown (1985), Sofianos (1996, 1999) and Diederichs and Kaiser (1999, 1999a, 1999b) extensively studied behavior of the arch zone and modified some of the assumptions regarding arch thickness and stress distribution. They used two different procedures to solve the indeterminate set of equations. Diederichs and Kaiser (1999a) used an iteration method, based on trial and error, to find the unknown parameters of the problem. They accepted linear stress distribution at the edges and mid-span but modified the average stress distribution within the beam and presented a new formula. A Universal Distinct Element Code (UDEC) was generated to verify the method and stability design curves were published for different modes of failure.

Furthermore, effects of internal tensile strength and abutment relaxation on stability of laminated rock masses were investigated.

On the other hand, Sofianos (1996) used the finite element results published by Wright (1974) and derived new formulas to reduce the unknown parameters. He considered equal normal thickness for compressive zones at the abutment and mid-span, which was the arithmetic average of both values. Sofianos and Kapenis (1998) developed a distinct element computer code to explore relations between unknown parameters and validate the stability limits. Moreover, Nomikos and Sofianos (2011) studied the probability distribution of the factor of safety and its probability density and cumulative distribution functions. Their analytical solution enables engineers to analyze the reliability of the supporting structures in underground mining.

It must be noted that since Diederichs and Kaiser (1999a) and Sofianos (1996) used different concepts to solve the indeterminacy issue of the voussoir method, there are noticeable differences between their results. They also applied different boundary conditions on their numerical models. Sofianos (1999) and Diederichs and Kaiser (1999b) discussed the differences of their approaches.

Furthermore, Hatzor and Benary (1998) applied the concept of voussoir beam method to analyze the potential reasons for roof failure of an ancient underground water storage reservoir. They also performed a two dimensional Discontinuous Deformation Analysis (DDA) in which the overlying layers on the immediate roof beam are modeled as well. This leads to a better understanding of load transfer in laminated roof beds. They also investigated the influence of joint spacing and block shape on stability. The minimum required friction angle for roof stability obtained by voussoir analysis and the DDA method is $36°$ and $60°$, respectively. The field data indicated that the friction angle is expected to vary from $38.6°$ to $46.4°$. By comparing the results of voussoir method and DDA with field data, it was concluded that DDA could predict failure of the roof bed by shear sliding while voussoir method was inaccurate and overestimated stability of the beam.

Following the application of DDA in roof stability assessment, Bakun-Mazor et al. (2009) used an integration of a discrete fracture model (geoDFN) with DDA method to analyze stability of an ancient underground quarry. The voussoir analysis, in this study, showed that the roof of the underground quarry must have failed due to snap-through failure; however, the excavation has been completely stable. Therefore, it was concluded that the voussoir method is fairly conservative as it overestimates the deformation.

In the most recent study, Hu (2016) conducted a series of tests to investigate response of the voussoir beam under transverse load. The experimental results were also used to calibrate numerical models, which were performed in $Phase^2$ of Rocscience. Finally, analytical voussoir beam method was applied to analyze the behavior of the joints of segmental concrete liners used in mechanical tunneling.

2.4.2 Modes of failure

Sterling and Nelson (1978) observed different types of failure during his experiment on load capacity of laminated beams. They summarized the failure modes as follows: 1) Compression (or crushing) failure at the center and ends of the beam is commonest failure and likely happens at center of the beam, prior to the abutments; 2) Snap-through (or buckling) failure happens due to large deflection at the center of the beam. As deflection increases, the arm of the resisting moment decreases, which leads to lower resistance against gravitational load; 3) Sliding failure at the abutments happens when the required friction angle is not available; however, Nelson's experiment was not designed to detect this type of failure; 4) Shear failure occurred once during one of the tests but no specific reason was noticed. It suddenly happened before the peak load. 5) Diagonal cracking was likely to happen after the peak load and followed by abrupt failure of the beam. The direction of propagation of the cracks was from top mid-span to bottom ends.

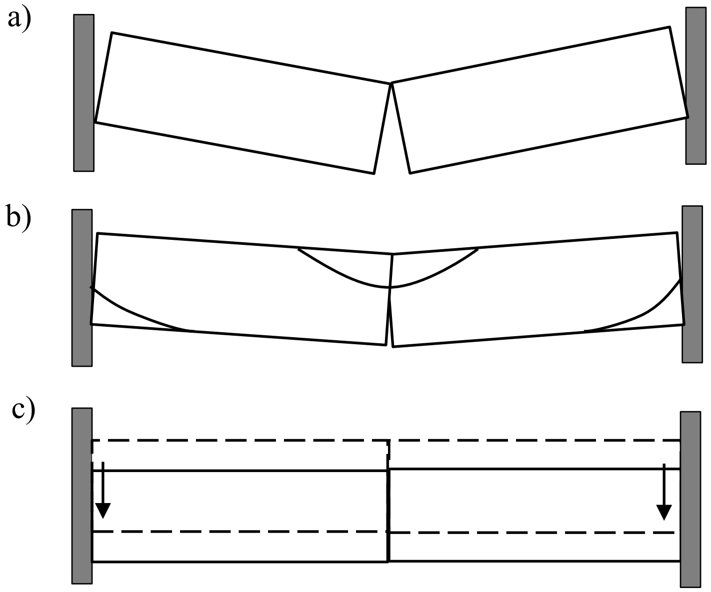

Figure 2.5 Failure modes of the voussoir beam: (a) snap-through; (b) crushing and (c) sliding (Diederichs and Kaiser, 1999a)

It has been observed that sliding failure is critical for beams with relatively low span to thickness ratio, while snap-through failure is likely for high ratios and crushing failure occurs in the mid-range of ratios. According to the previous findings, three major types of failure must be examined for design of excavations in jointed rock masses. These modes of failure are: snap-through failure, crushing at the mid-span and abutments, and sliding at the abutments (Figure 2.5).

In order to investigate the stability of voussoir beams against different modes of failure, factors of safety for each mode must be defined and limits of stability must be specified. Then, purpose of the solution would be to calculate values of factors of safety to find out in what condition voussoir beams are stable.

2.4.3 Design procedure of the voussoir model

A typical roof beam above an excavation with no joints is sketched as a simple elastic beam with a constant cross section and horizontal span and thickness punctuated by s and t (capital letters have been also used in some publications). Distribution of compression and tension are indicated in symmetrical around the centerline of the beam.

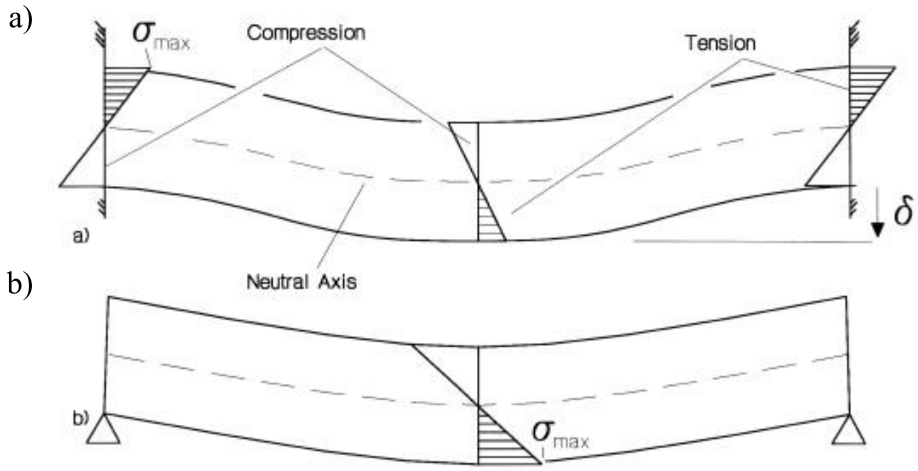

Figure 2.6 Elastic beam with (a) fixed ends and (b) simple (pin) supports (Diederichs and Kaiser, 1999a)

The maximum value of compressive stress would be at the bottom of the abutments and top of the mid-span while maximum tension would occur at the bottom of the mid-span and top of the abutments. By using simple closed form solutions, the maximum stress values and deflection for a simple fixed ends beam (Figure 2.6a) can be calculated as follows

$$\sigma_{max} = \frac{\gamma s^2}{2t} \quad \textbf{(2.1)}$$

$$\delta = \frac{\gamma s^4}{32Et^2} \quad \textbf{(2.2)}$$

where E is the Young's modulus of the rock and γ is the specific weight of the beam. Since the maximum stress at the mid-span is half of the abutments, yield is likely to happen when the maximum tensile stresses exceed the tensile strength of the beam at the top of the abutments. Consequently, vertical fractures become initiated at the abutments and the beam becomes simply supported (Figure 2.6b). The maximum tensile stress can be obtained by

$$\sigma_{max} = \frac{2\gamma s^2}{3t} \quad \textbf{(2.3)}$$

The value of tensile stress is now higher than the prior value of stress at the abutments and rock tensile strength, which leads to a central fracture at the mid-span. This progressive cracking at the abutments, mid-span and other parts of the beam converts any laminated roof structure to a discontinuous medium. Existence of tensile fractures and cross-cut joints make the beam fail to carry tensile stresses but it does not mean that roof beam would collapse. In this condition, a compression arch would be generated from the abutments to the top of the mid-span. Although the thickness of the compression arch is variable, Evans (1941) assumed a normal compressive thickness of $n = 0.5$ for simplification. Diederichs and Kaiser (1999a) claimed that normal compressive thickness is close to 0.75 for stable beam and less than 0.5 for unstable situations.

2.4.3.1 Constitutive law and statics

The voussoir beam geometry for a laminated roof bed before deformation is illustrated in Figure 2.7a. Also forces and notations are indicated in Figure 2.7b for half of span after deformation. Since the voussoir beam is symmetric, half of the beam is taken into account. The main assumption is that lateral thrust is transmitted to the abutments through a parabolic arch within the beam. Load distribution is also assumed to be triangular over the abutment surface of the beam and central section. The horizontal stress is not symmetric through the thickness of the beam. Therefore, closed form solutions cannot examine the response of the beam.

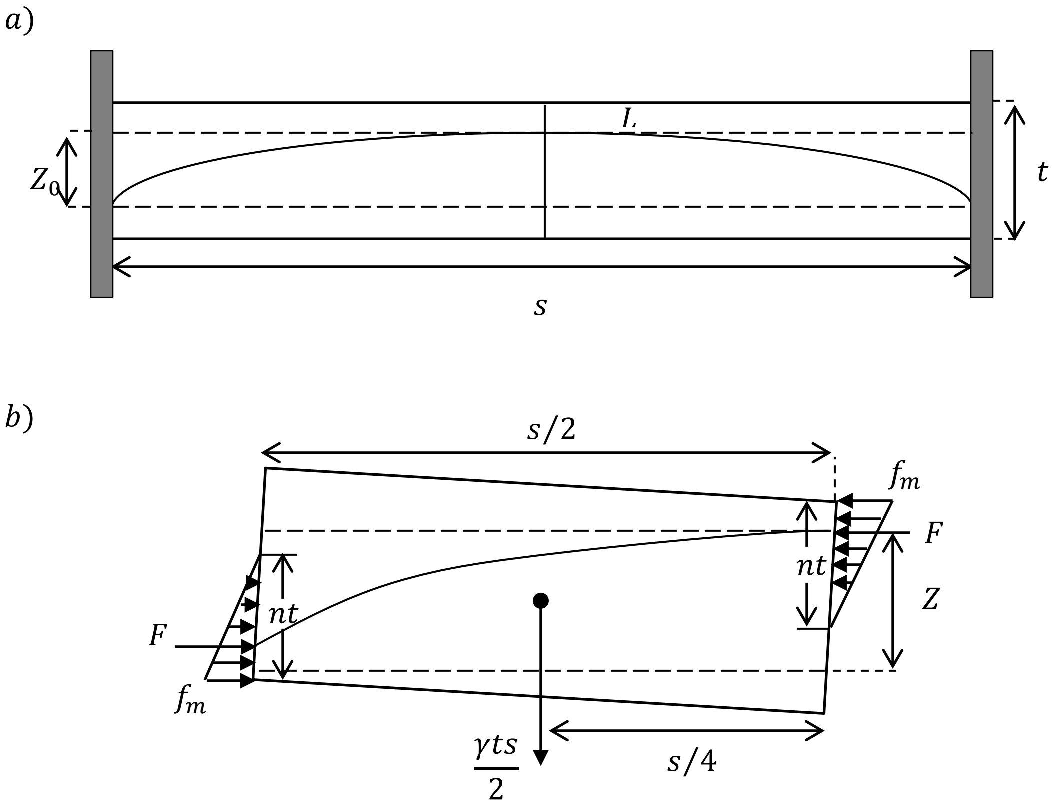

Figure 2.7 Initial geometry of a voussoir beam (a); and notation for analysis of a deformed half-span beam (b)

The roof beam of span s, thickness t and unit weight γ, is under its own weight W, while the average thickness of the arch, nt, and the ultimate moment arm, z, between the reaction forces, F, at the mid-span and at the abutments are initially unknown. The lateral thrust at the abutments and center of the beam is exerted over the arch thickness $h = nt$ of the beam. All the calculations are based on the unit width of the beam in the out-of-plane direction. As shown in Figure 2.7b, the moment arm due to the couple acting at the center and abutment is Z_0 while after displacement, it would be reduced to Z. Hence, the vertical displacement of the beam is given by

$$\delta = Z_0 - Z \tag{2.4}$$

The initial moment arm, z_0, can be simply calculated as

$$Z_0 = t(1 - \frac{2}{3}n) \tag{2.5}$$

The model assumes reaction force locus forms a parabolic arch. Therefore the length of the arch can be obtained by simple geometric calculations (derivation of the following equation is presented in 0)

$$L = s + \frac{8}{3s}{Z_0}^2 \tag{2.6}$$

For the sake of stability, the moment caused by weight of the beam at the abutment, M_W, must be compensated by a resisting moment, M_R, which rises due to deflection of the beam and operates at the abutment and center of the beam.

$$M_W = \frac{1}{2}\gamma t s^2 \tag{2.7}$$

$$M_R = FZ = \frac{1}{2} f_m n t Z \tag{2.8}$$

where f_m is the maximum compressive stress at the lower part of the abutment and top of the mid-span. Writing the moment balance at the abutment gives

$$\sum M = 0 \tag{2.9}$$

Thus the maximum stress is

$$f_m = \frac{1}{4}\frac{\gamma s^2}{nZ} \tag{2.10}$$

In all the calculations, the specific weight, γ, of the beam can be replaced with an effective specific weight, γ_e. This makes the solution applicable to inclined laminations, which α is the angle from the horizon.

$$\gamma_e = \gamma \cos\alpha \tag{2.11}$$

In order to find the factors of safety, values of maximum stress, f_m, normal thickness of the arch, n, and arm of the arch, z, must be determined. Since the axial stress is not uniformly distributed, an assumption regarding the distribution of the internal stress within the beam must be considered. Brady and Brown (1985) proposed a bilinear variation along a constant arch section as shown in

Figure 2.8. The value of axial stress is maximum at the abutment and mid-span, while it is lowest in the middle of the half beam. It is assumed that the entire thickness is

under compression where the axial stress is lowest and uniformly distributed over beam's thickness. The axial compressive stress applied at the centroid of the abutment and mid-span, σ_c, is

$$\sigma_c = \frac{2}{3} f_m \tag{2.12}$$

Due to force balance, the lateral thrust applied at the abutment, F, is equal to horizontal force in the middle of the half span.

$$\frac{f_m}{2} nt = f_{min} t \tag{2.13}$$

Thus

$$f_{min} = \frac{n}{2} f_m \tag{2.14}$$

Therefore the average stress, f_{av}, along the reaction line can be calculated by

$$f_{av} = \frac{f_m}{2} (\frac{2}{3} + \frac{n}{2}) \tag{2.15}$$

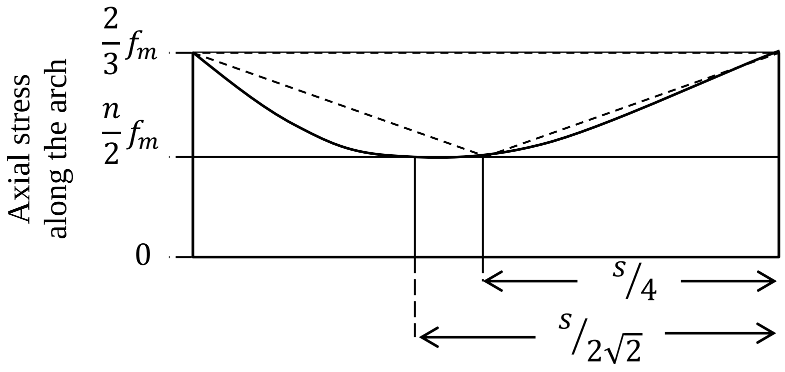

Figure 2.8 Axial stress distribution along the compressive arch; bilinear (dashed line) and quadratic (solid line) variation

Diederichs and Kaiser (1999a) suggested that the entire beam section is under a constant stress where the centerline of the beam crosses the reaction arch line. They assumed a quadratic variation of the stress along the reaction line and proposed the following equation

$$f_{av} = \frac{f_m}{3}\left(\frac{2}{3} + n\right) \tag{2.16}$$

Although they claimed that the stress distribution within the compressive arch is parabolic, the solid line in Figure 2.9 clearly shows that it is not a parabola. The graph of a quadratic function is a curve where any point is at an equal distance from a fixed point and a fixed straight line, which does not match the curve in this figure. It was also expressed that the location of the minimum stress within the arch is not the middle of the half span, as it happens at $\frac{s}{2\sqrt{2}}$ away from mid-span. This is the intersection of the reaction line and centerline.

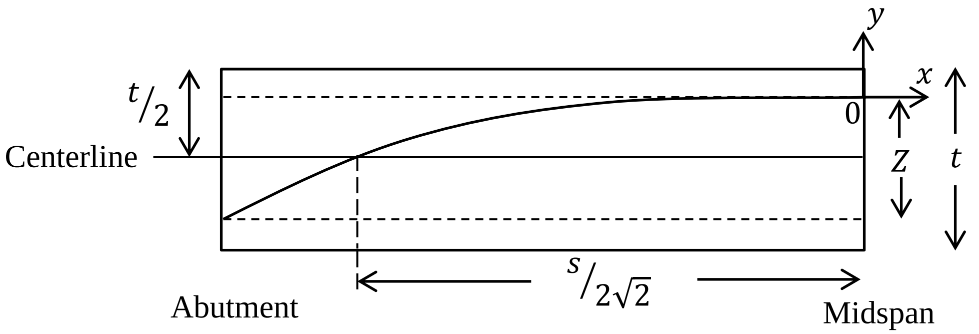

Figure 2.9 Centerline and arch line within the half beam

Following the procedure as presented in 0, the equation of the reaction arch line after deformation would be obtained as

$$y = \frac{-4Z}{s^2}x^2 \tag{2.17}$$

Also equation of the centerline is

$$y = \frac{-Z}{2} \tag{2.18}$$

Thus the intersection is

$$x = \pm\frac{s}{2\sqrt{2}} \tag{2.19}$$

Having the average stress within the beam, elastic shortening of the arch can be obtained by Hook's law

$$\Delta L = L\frac{f_{av}}{E} \tag{2.20}$$

where E is the Young's modulus of the rock mass in the direction parallel to the beam axis. Using the same procedure presented in 0, the length of the arch after deformation, L', can be obtained

$$L' = s + \frac{8}{3s}Z^2 = L - \Delta L \tag{2.21}$$

Rewriting this equation gives

$$Z^2 = \frac{3s}{8}(L - s - \Delta L) \tag{2.22}$$

Combining this with equation (2.6) gives

$$Z^2 = \frac{3s}{8}(\frac{8}{3s}Z_0{}^2 - \Delta L) \qquad \textbf{(2.23)}$$

Rewriting this equation leads to the arm of arch after deflection

$$z = \sqrt{\frac{3s}{8}(\frac{8}{3s}z_0{}^2 - \Delta L)} \qquad \textbf{(2.24)}$$

In order to obtain a reasonable value for the moment arm, Z, a positive value for the term under the square root is necessary. A negative value shows an unstable situation. It means that deflection has exceeded the critical value and subsequently snap-through failure would occur. If it is not possible to find a value for the normal compressive zone, n, between 0 and 1, ultimate collapse of the beam occurs.

The goal of the analysis is to find a pair of values of n and Z which meets all the presented equations. Evans (1941) supposed a constant value of $n = 0.5$ and oversimplified the calculations. Diederichs and Kaiser (1999a) proposed an iterative solution to calculate a pair of values of n and Z which corresponds to the minimum value of the maximum stress at the abutments and mid-span f_m.

In this method, n varies in increments from 0 to 1 and Z is calculated in each increment based on the value of n. When the beam is completely stable, the proposed solution finds the value of Z in each increment; however, the percentage of n values that could lead to a rational value of Z would drop as the span of the beam increases. Eventually, there would be no pair of n and Z values for the given beam. Determining the minimum value of f_m, the vertical displacement, δ, can be specified by calculating the difference between moment arm prior and after deflection.

2.4.3.2 Factors of safety

Based on the response of the beam to the transverse load and rock mass properties, the factors of safety against potential modes of failure can be determined. Crushing failure is most likely to happen at the lower edge and top mid-span of the beam where the maximum compressive stresses are concentrated. When the maximum stress exceeds the strength of the material, crushing failure happens. Thus it is defined as the ratio of unconfined compressive strength of the rock mass with respect to the maximum compressive stress:

$$F.S._{crushing} = \frac{UCS}{f_m} \tag{2.25}$$

A value of $F.S._{crushing}$ less than one represents ultimate crushing failure; however, depending on the material and safety considerations, higher values might be considered as the crushing limit.

The factor of safety against shear sliding can be calculated by analyzing the beam loads along the abutments. Sliding at the abutments happens due to mobilization of a frictional resistance. Since beam is under its own weight, the abutment shear force is

$$V = \frac{1}{2}\gamma st \tag{2.26}$$

This vertical force needs to exceed the shear resistance due to lateral thrust

$$T = F\ tan\varphi = \frac{1}{2}f_m nt\ tan\varphi \tag{2.27}$$

Equating these two equations leads to the factor of safety against shear sliding failure

$$F.S._{slide} = \frac{f_m n}{\gamma s} \; tan\varphi \qquad \textbf{(2.28)}$$

When the value of $F.S._{slide}$ is less than one, ultimate shear failure happens. This mode of failure strongly depends on the span of the beam and joint properties. Therefore, different values other than one can be assumed as shear limit.

Buckling failure happens when vertical displacement of the beam exceeds a certain limit. This limit is specified with respect to the thickness of the beam. The ultimate failure occurs for displacements greater than one quarter of the thickness ($0.25 \times t$). A yield point is also reported which is the onset of the nonlinear behavior of the beam and corresponds to 10 percent of the thickness ($0.1 \times t$).

Diederichs and Kaiser (1999a) also introduced a numerical approach for the factor of safety for buckling. It is defined as the ratio of the values of n with no reasonable solution. As normalized equilibrium arch thickness, n, decreases, the buckling limit, $B.L.$, increases. The ultimate failure happens at value of 100% for $B.L.$, while yield corresponds to $B.L.$ of 35%. It has been observed that stability cannot be achieved if a compressive arch is not generated within the beam to transfer the vertical loads to the abutments. Figure 2.10 shows flowchart of the iterative method proposed by Diederichs and Kaiser (1999a).

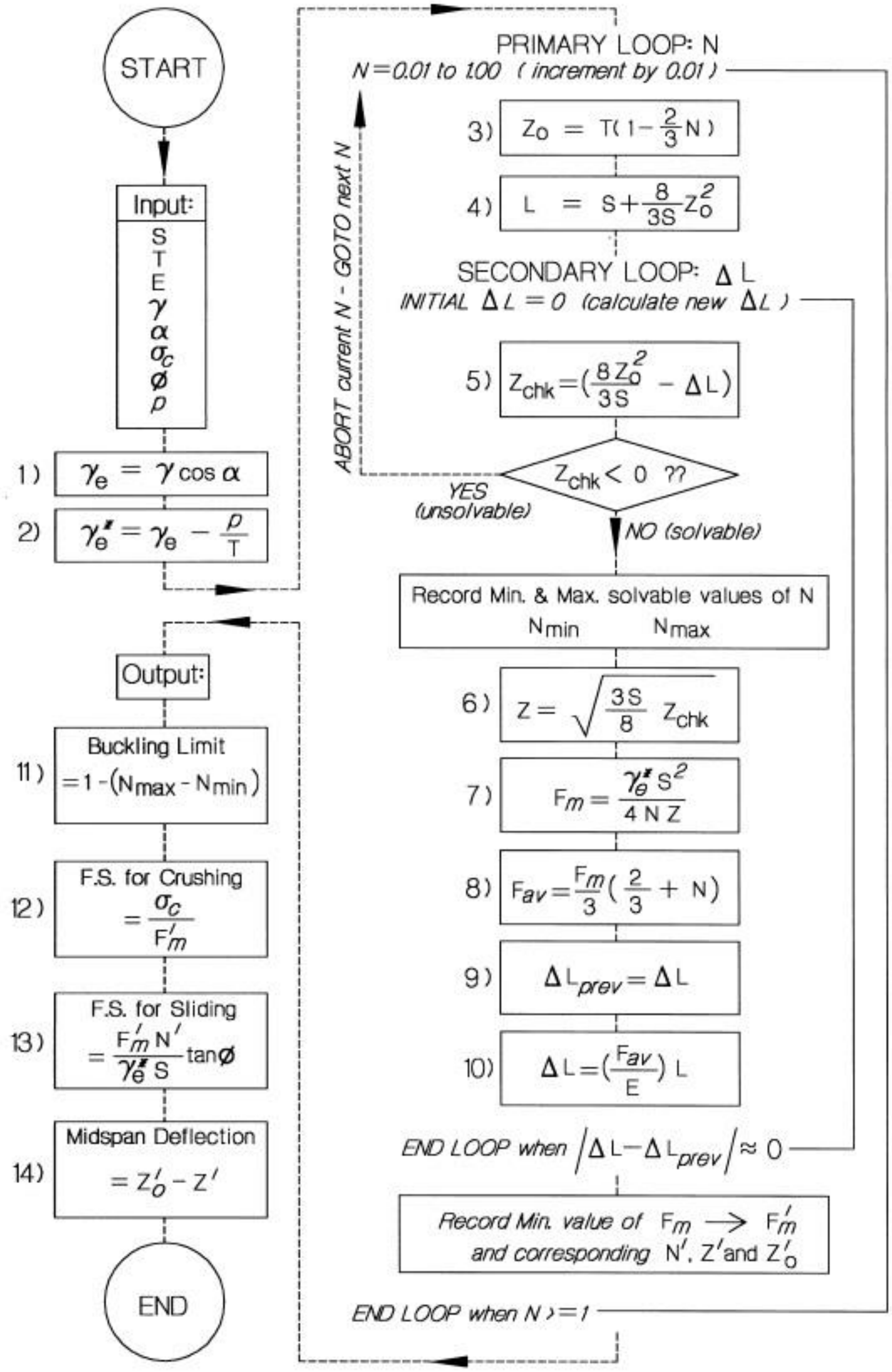

Figure 2.10 Flowchart for the determination of stability and deflection of a voussoir beam (Diederichs and Kaiser, 1999a)

2.4.4 Numerical analysis

Numerical models have been used to investigate accuracy of the voussoir method's assumptions and the proposed formulas. Sepehr and Stimpson (1988), Wright (1972), Barker and Hatt (1972), Passaris et al. (1993) and Ran et al. (1994) performed finite element analyses; whereas, Sofianos and Kapenis (1998) and Diederichs and Kaiser (1999a) used distinct element codes.

Finite element models assume the beam is a continuous medium and model the cracks with thin elements and very low modulus. Finite element method cannot simulate the behavior of discontinuities as separation or opening is not permitted. It is incapable of examining the ultimate collapse of the beam by sliding failure. Thus, it is not suitable to model a jointed rock mass such as voussoir beams. On the other hand, Universal Distinct Element Code (UDEC) provides a 2D implementation of the distinct element method. This numerical computer code, which employs a dynamic relaxation algorithm to solve the systems of equations, allows for the development of large displacements before the collapse of the beam. Therefore, maximum displacement of the beam, stress distribution and opening of the joints can be examined.

The same geometry as physical models is considered for UDEC models. The beam has two blocks of rock attached to the abutment rocks with vertical joints at the abutments and mid-span. Sofianos & Kapenis (1998) considered a model with a deformable beam rock and rigid abutments. Joints have very high stiffness values. Also high shear strength is considered to prevent the beam from sliding. In addition, they assumed zero friction and zero cohesion for the mid-span joint to have both vertical slip and lateral separation. Their model could simulate the stress distribution but considerably underestimated the compressive thickness within the beam and maximum deflection.

Diederichs & Kaiser (1999a) declared that fixed supports or rigid abutments cause stress concentration at bottom edges of the beam which leads to higher moment arm and lower deflection. These boundary conditions make the predictions inaccurate. Hence, they considered elastic deformable blocks for beam and abutments. Joints are elastic (no tension) with purely frictional surfaces. Considering flexible abutments with very high stiffness values led to better predictions that are more consistent with the numerical analysis by Ran et al. (1994).

The numerical models may predict higher thickness values than the analytical solution. It might be due to non-linear distribution of the stress at the abutments and mid-span in UDEC models, while it has been considered triangular in analytical method. However the major reason for difference in results is block overlapping which is allowed in the numerical simulations with UDEC (Itasca consulting group, 2010). This causes the deviation of the numerical results, which is obtained by UDEC, and analytical results. UDEC allows blocks to penetrate into each other with an infinitesimal size (overlapping) to capture the interaction. The block penetration and the following large connection area between the beam and abutments generate the interaction of stress between the blocks in the model. The penetration size depends on the size of the blocks in the model. Therefore larger thickness of the arch within the beam is expected to be generated in the simulations than analytical solution. Overall, it can be concluded that the analytical solution proposed by other researchers can model the behavior of voussoir beams well enough and can be applied to the stability assessment of roof stratum.

2.5 Concluding remarks

Due to the high risk of gravity driven failures during and after excavation, stability assessment is crucial for the design of an underground cavern. The voussoir beam method provides an analytical solution for roof beam stability analysis. Sterling (1980) examined the assumptions of the method and published main conclusions of all previous investigations. The main conclusions of the theory are summarized here

- Cross joints and fractures form a blocky rock mass around an excavation, therefore elastic beams or plates cannot model the behavior of the roof beams
- Load capacity of the roof beam under gravity loading depends on the generation of an arch structure by compressive stresses within the beam and confined by abutting rock
- For a voussoir beam with low span/thickness ratio, the most likely failure mode is shear failure at the abutments
- Roof beds have zero tensile strength and show elastic behavior
- Main potential failure modes are snap-through, crushing at the abutments and sliding failures
- The use of numerical models (such as UDEC) is necessary for verification of the results of the voussoir beam method

The iterative approach presented in the next chapter is based on the work published by Diederichs and Kaiser (1999a), which is a modified version of the model proposed by Brady and Brown (1985).

CHAPTER 3 – Analysis and Results

3.1 Introduction

This chapter describes all the analysis, new assumptions and equations and generated results. It would show that the modified version of voussoir beam significantly improves accuracy of the results. For this purpose, mechanism and assumptions of voussoir beam method have been examined using a Universal Distinct Element Code (UDEC). Parametric study has been done for a wide range of beam parameters and types of rock mass to demonstrate validity of the modifications.

First, an existing case has been used to regenerate the results and verify the iterative solution, which is described in section 3.2. Then, characteristics of the developed model in UDEC have been presented in section 3.3. This section is followed by analyzing the stress distribution process, investigation of arch structure within beams and determining the minimum and maximum axial stresses, using both UDEC and existing voussoir beam method.

Section 3.4 introduces the new assumptions and equations that have been used to improve the method. Then, response of the roof beam is investigated for various rock mass properties and results of numerical simulations, existing and modified voussoir beam method have been compared. Section 3.5 incorporates effect of creep deformation on roof beams using both UDEC and modified voussoir beam method. Also, application of the modified method and UDEC simulations to underground caverns is presented in section 3.6, which includes response of the roof beams to cavern inside pressure.

3.2 Verification of the iterative solution

The procedure indicated in Figure 2.10 has been implemented in MATLAB code (MathWorks, 2016). Due to potential errors in numerical calculations and computer programming, the final results must be verified against data published by previous researchers. Hatzor and Benary (1998) examined the response of a voussoir roof beam by analyzing the stress distribution, deflection and factors of safety. They published the results using simple and clear graphs. Therefore, results of the developed program have been verified against their data.

They have examined the stability of the Tel Beer-Sheva water reservoir (2700 B.P to 3200 B.P). It is located approximately 3 km South – East of the modern city of Beer Sheva. The required geometrical parameters were identified using field mapping and site investigations. Mechanical properties of the intact rock and joints were determined using core samples. The excavation was created in horizontally bedded chalk with three vertical joint sets. Underground rock mass was considered as separate single layers and classical voussoir beam theory was applied. Input parameters are summarized in Table 3.1.

Table 3.1 Voussoir beam parameters considered by Hatzor and Benary (1998)

Parameter	Value	Unit
Young's modulus, E	2000	MPa
Specific weight, W	18.7	KN/m
Unconfined compressive strength, UCS	7	MPa
Friction angle, $\emptyset$	40	°

Different spans ranging from 3 to 9 m were studied and the maximum axial stress, f_m, for various beam thickness was calculated. As Figure 3.1 shows, f_m increases with span and significantly decreases with thickness. For a given span and thickness, the stability against local crushing at hinge zones can be assessed by comparing the maximum axial stress and unconfined compressive strength values. Figure 3.1 clearly shows that data points, generated by computer programming, fairly conform to published results by Hatzor and Benary that are displayed by solid lines. The average error is as low as 3.21%.

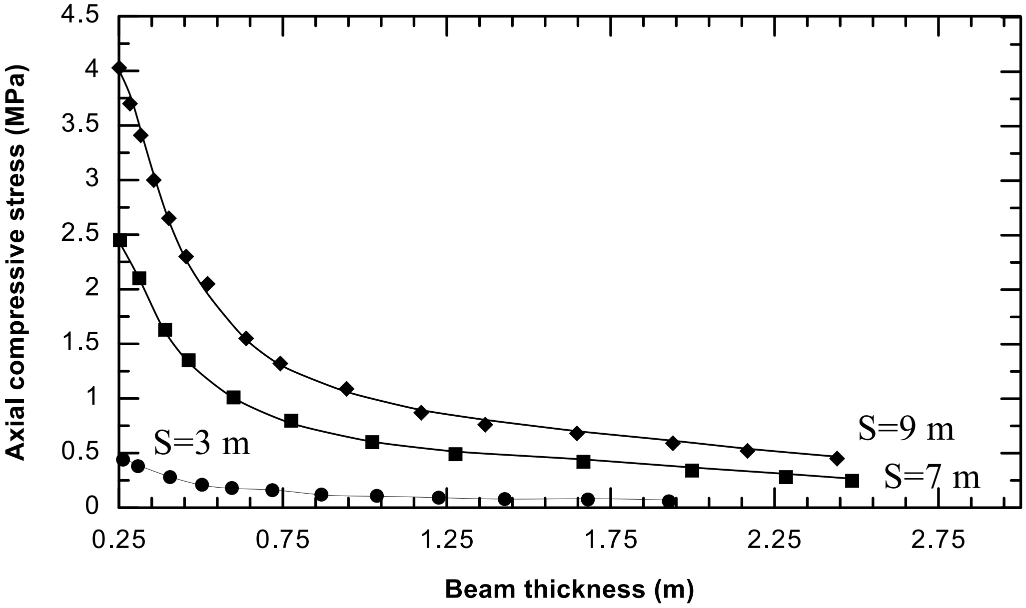

Figure 3.1 Relationship between maximum horizontal compressive stress and beam thickness for span=3, 7 and 9 m; results are published by Hatzor and Benary (solid lines) and generated by programming (data points)

The factor of safety against sliding at the abutments is also studied for various thickness and friction angles. Equation (2.28 shows that shear sliding is directly dependent on friction angle, while thickness of the beam affects the factor of safety by reducing maximum axial stress. For this purpose, a constant span of $7\,m$ with friction angles of $20°, 40°$ and $70°$ has been assumed, while other properties are similar to Table 3.1. As

Figure 3.2 shows, sliding is likely to happen when span/thickness ratio increases and friction angle decreases. Results are fairly consistent as the error is 2.8%.

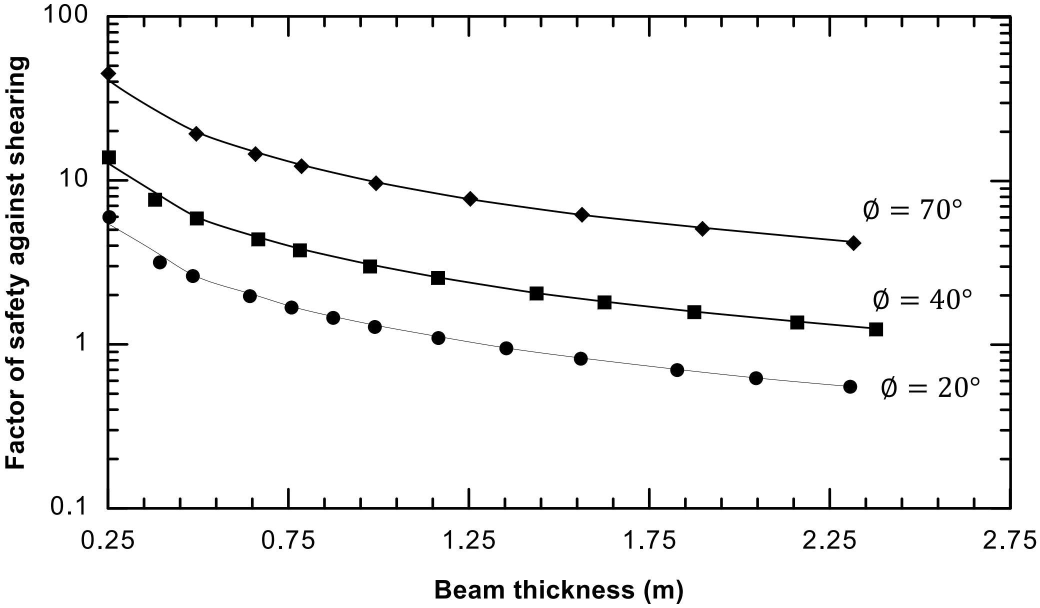

Figure 3.2 Factor of safety against shear along abutments for friction angles of 20°, 40° and 70° and a constant roof span of 7 m ; results are published by Hatzor and Benary (solid lines) and generated by programming (data points)

The stability of same roof beam against failure in compression is also investigated by Tsesarsky and Hatzor (2003). The results of parametric analysis are depicted in Figure 3.3 in which different span and beam thickness values are considered. Figure 3.3 shows that crushing failure is likely when beam span increases and thickness decreases. The average error is 4.54%. Since the results are noticeably greater than the threshold and the selected beams are all stable, error of 4.54% is an acceptable value. It can be concluded that the numerical calculations are trustable as the results are verified against published data. The next step is to verify the voussoir beam method using numerical simulations.

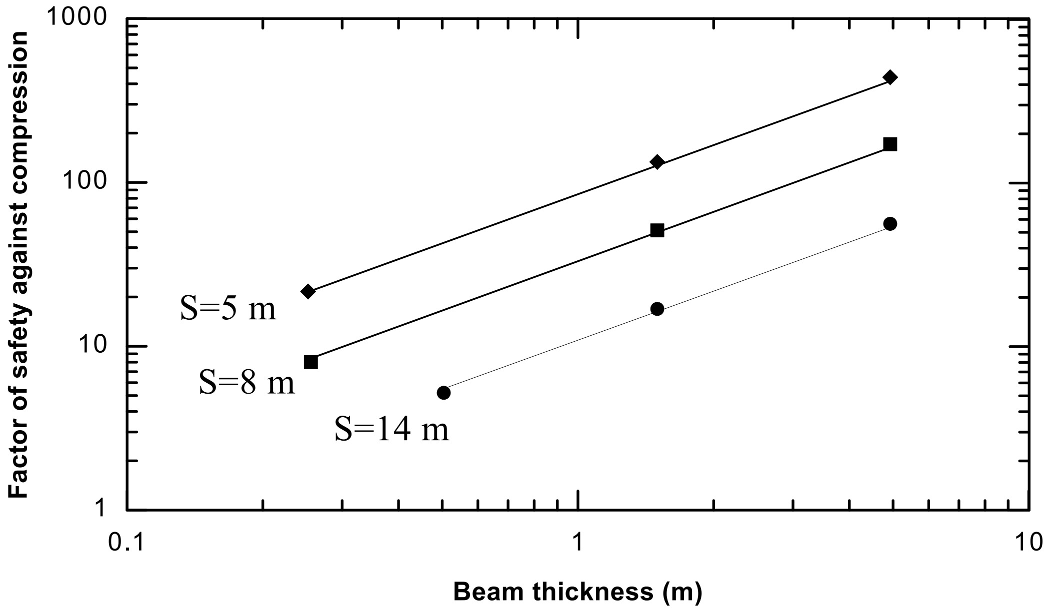

Figure 3.3 Factor of safety against compression for span of $\mathbf{5, 8}$ and $\mathbf{14\ m}$; results are published by Hatzor and Benary (solid lines) and generated by programming (data points)

3.3 Numerical analysis using UDEC

The structural response of the voussoir beam is simulated using a Universal Distinct Element Code (UDEC). One could use this software to investigate the mechanical behavior of a discontinuous medium, such as an underground excavation. Consequently, a blocky roof rock, like a voussoir beam, can be examined by this code. The goal of the simulations is to investigate the displacement, stress distribution and factors of safety within the roof layer for various roof beam parameters and ultimately verify the voussoir beam concepts and accuracy of the modifications.

3.3.1 Model overview

A similar model to the model that Diederichs & Kaiser (1999a) developed has been used. It consists of three deformable elastic blocks. They are discretized and jointed to represent the voussoir beam. The contact of the middle block with abutment rocks makes the joints at the abutments. The third joint is located at the mid-span. If any other joints are added to the model, it affects the rock mass modulus of the beam in classical voussoir analysis. This is critical for comparing the numerical results with voussoir beam analysis. Figure 3.4 shows a typical voussoir beam with boundary conditions. The shaded blocks represent the abutments.

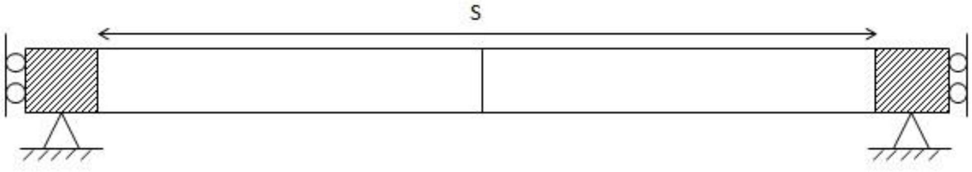

Figure 3.4 Geometry and boundary conditions of the voussoir beam in UDEC

The model is applied to a set of rock and joint properties with a wide range of beam spans and thicknesses. The values of joint stiffness and spacing are assumed regarding the characteristics of the selected rock types. Joint shear and normal stiffness (k_n, k_s) vary based on the quality of the rock mass and how weathered the joints are. Low values of the joint stiffness are for the joints filled with weathered rock with low deformability modulus, while high values of stiffness are for unweathered closed joints.

All the blocks are discretized using triangular zones with a height (x-direction) to width (y-direction) ratio of 2:1. UDEC rounds the block corners to prevent unnatural stress concentrations. This does not simplify the results because the corners are also naturally crushed in a rock mass. The rounding length of the model must be high enough to allow the displacement; otherwise the contact overlap would be greater than the rounding length. When UDEC crashes during the cycling with a "contact overlap too great" error message, it means one block penetrates too far into another. The contact overlap should be less than one half of the rounding length to prevent any error, while more rounding length causes higher unbalanced force and more running time. On the other hand, block edge length is at least twenty times greater than the rounding length, while rounding length must be less than zone edge length. The value of zone edge specifies the maximum length of any edge on a zone. This controls the density of the discretization in each model.

As the result, the length of the elements needs to be optimized to prevent any error and generate accurate results. Since the thickness of the beam is only one meter. It is subdivided into six elements in the y-direction. Number of elements in x-direction is different in each model depending on the beam span. They are discretized in a way to maintain the zone aspect ratio of 2:1.

All the joints are elastic with a frictional surface, no tension and no cohesion. The displacement is controlled by the normal and shear stiffness (k_n, k_s). Since the natural fracture frequency of the rock mass is 0.5 m, the same value has been assumed for joint spacing (S_j) within the beam. Figure 3.5 illustrates two different joint patterns in a typical voussoir beam.

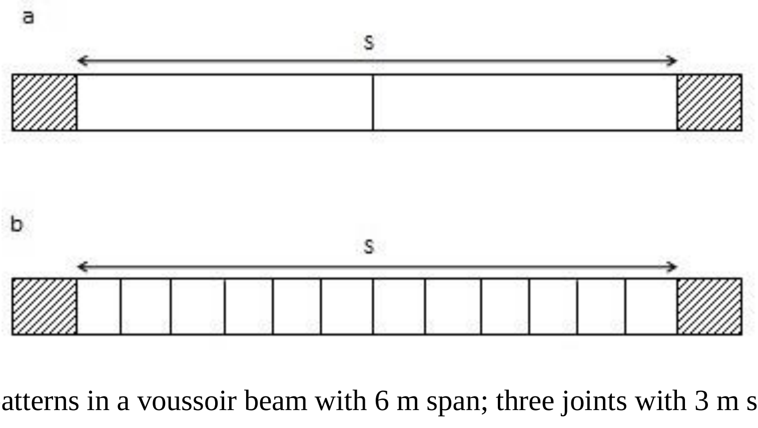

Figure 3.5 Joint patterns in a voussoir beam with 6 m span; three joints with 3 m spacing (a) thirteen joints with 0.5 m spacing (b)

Fracture is a surface of breakage within the rock mass on which there has been no movement. If planes of a fracture move only normal to each other, it would be considered as a joint. Although fractures are not necessarily the same as joints, it is reasonable to assume fractures in a roof layer behave like joints. This makes the model more conservative, as greater displacement is expected with more joints.

The voussoir beams deform under their own weight. Thus, the model is under gravitational load with gravitational acceleration, g, equal to $9.81\ m$. If the effect of surcharge or support pressure is interested, a boundary stress or pressure must be applied on the upper or lower edge of the middle block. Figure 3.6 shows a voussoir beam in UDEC before displacement. The green colour blocks are the abutments. They are not completely fixed but they have a high stiffness value ($200\ GPa$), because fixed blocks do not match with reality and incorrectly cause stress concentration at zone edges. Deformable and stiff abutments prevent stress concentration and provide a better displacement and stress compatibility.

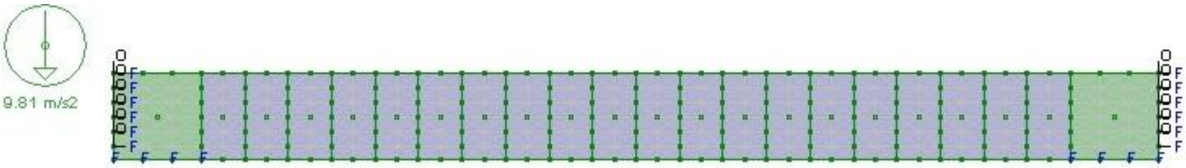

Figure 3.6 A typical discretized voussoir beam model with 10 m span and 0.5 m joint spacing in UDEC

Size of elements in x and y directions are 0.4 and $0.2\ m$, respectively. This is based on a convergence study (Table 3.2 and Figure 3.7). Length of elements, in each step, is reduced to half of its length in the last step, to examine convergence of the results. Table 3.2 shows maximum displacement of the beam for each size of elements and percent of change in the results with respect to previous step. Step two shows a high percent change (23.78%), while element size of step three shows lower change in the results. When size of elements is set to 0.2 and 0.1 in x and y directions (step four), the change drops to below 1%; which shows convergence of the results. Therefore, element size in step three is selected as the optimum value for discretization.

Table 3.2 Convergence of beam displacement

Step	Zone length (x direction × y-direction)	Maximum displacement at mid-span (m)	Percent change (%)
1	1.6 × 0.8	0.01123	-
2	0.8 × 0.4	0.0139	23.78
3	0.4 × 0.2	0.01354	2.62
4	0.2 × 0.1	0.01364	0.77
5	0.1 × 0.05	0.0137	0.44

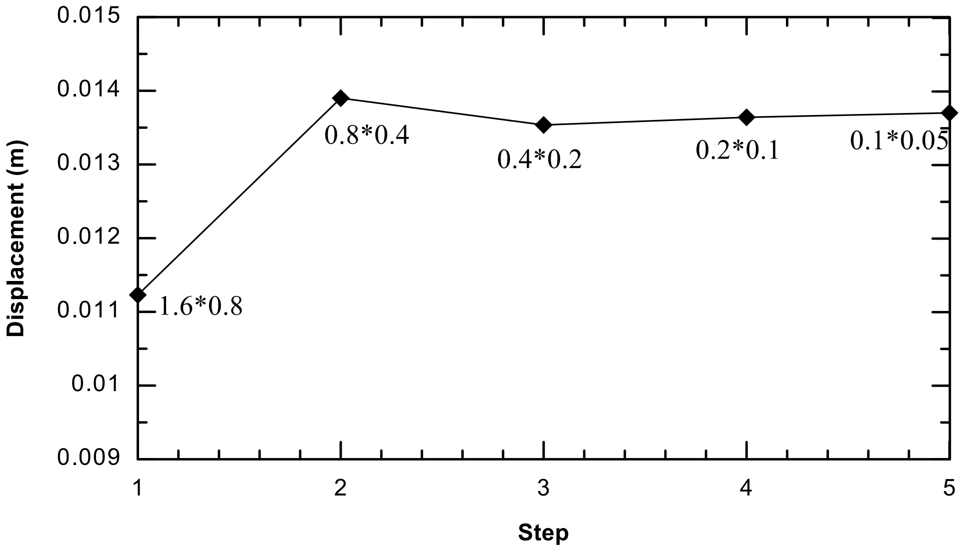

Figure 3.7 Maximum displacement with different zone length

First, the beam is set to deform elastically until the equilibrium is reached. At this stage, all the joints have a non-zero value for tensile strength. Their tensile strength is set to $0.01\ MPa$. Any reasonable and non-zero value works properly at this step. This allows the stress and frictional strength accumulate in the joints. If this stage is removed from the simulation, blocks of rock would drop before the arch stresses are generated. Then, joint tensile strength is set to zero and the beam continues to deform until equilibrium or failure. The value of tension at the initial stage should be a small value, less than one megapascal, because a high tensile strength makes the beam to slip over the abutments and displacement would be the same in all cross sections of the beam.

3.3.2 Stress distribution

It is assumed that the roof beam is deformed under its own weight. It is also noted that upper layers above an excavation tend to transfer gravitational load laterally to the abutments rather than vertically to the lower layer. This is due to generation of an arch-shaped stress distribution within the beam. This arch specifies a compressive zone that transfers the vertical loads to the abutments and makes the beam stable (Figure 2.2).

In order to examine the process of stress distribution and assumptions of the method, different types of voussoir beams are simulated in UDEC. The developed models have rock and joint properties of six different media. The selected rock types are chalk, cap rock layer of unit B in the Salina Group salt beds (shaly carbonate), potash, cap rock layer of unit A2 (shaly carbonate), limestone and dolostone. Input parameters are selected in a way to represent media that are likely to exist around excavations, which voussoir beam method can be applied. It includes the two types of rock that represent the cap rock layers of unit B and unit A2 of the Salina Group of salt beds. This selection covers a range of weak to strong rock masses (from low to high values for density, stiffness, strength, etc.). The beam parameters are summarized in Table 3.3.

The model is allowed to deform elastically under its own weight. Figure 3.8 and Figure 3.9 show the displacement vectors and axial stress contours after deformation for a voussoir beam. Since the maximum displacement is less than 10 percent of thickness ($\delta = 0.01\ m$), the beam is stable. Therefore, the following figures show the response of the beam after equilibrium is reached. The maximum displacement occurs at the middle of the beam within the intermediate joint. Figure 3.9 presents principal stress tensors within beam. As it shows, the major part of the beam is under compression, while small zones at top edge and bottom mid-span are under tension. The bottom edge and top mid-span of the beam are three zones of high compressive stress concentration. The maximum axial stress (σ_{xx}) is greater than 2 MPa at the abutments for this beam properties. The negative sign for stresses in Figure 3.9 indicates that stresses are compressive and positive values show tensile stresses.

Table 3.3 Summary of the beam parameters

Parameter	Chalk	Unit B	Potash	Unit A2	Limestone	Dolostone	Unit
Density (ρ)	2100	2560	2250	2680	2700	2800	Kg/m^3
Young's modulus (E)	2	3	6	23	40	60	GPa
Joint normal and shear stiffness (k_n, k_s)	3.5	8.4	9	8.24	7	10	GPa/m
Joint friction angle (φ)	30	25	30	25	20	35	°
Joint spacing (S_j)	1	0.5	0.5	0.5	1.5	2	m
Unconfined compressive strength (UCS)	7	8	26	60	60	140	MPa
Rock mass modulus (E_{rm})	1.27	1.75	2.57	3.49	8.3	15	GPa

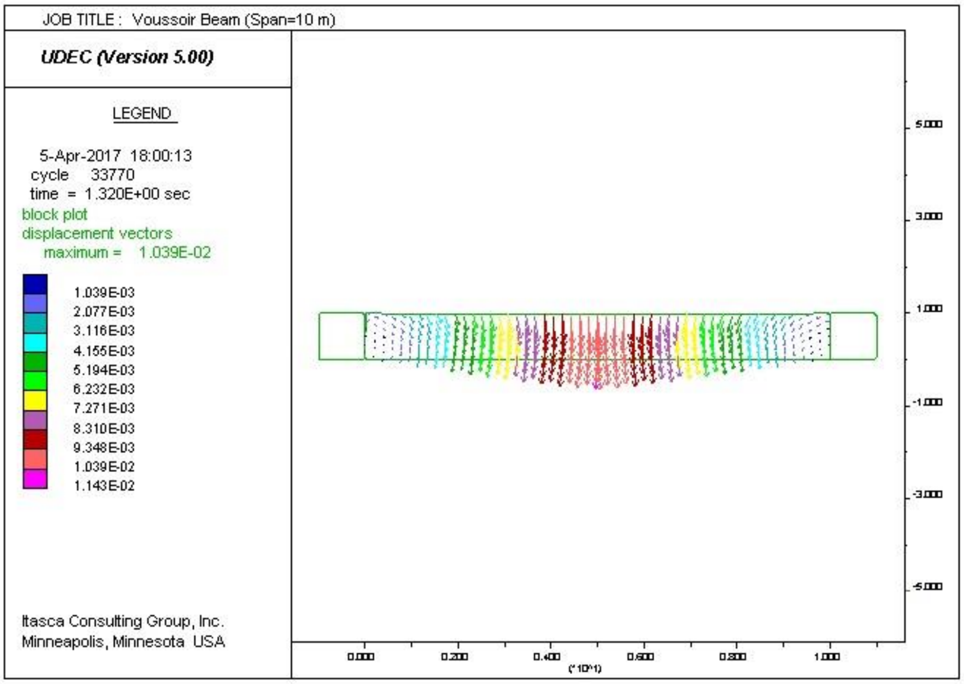

Figure 3.8 Displacement vectors for a voussoir beam (Unit B rock mass, span=10m, thickness=1m)

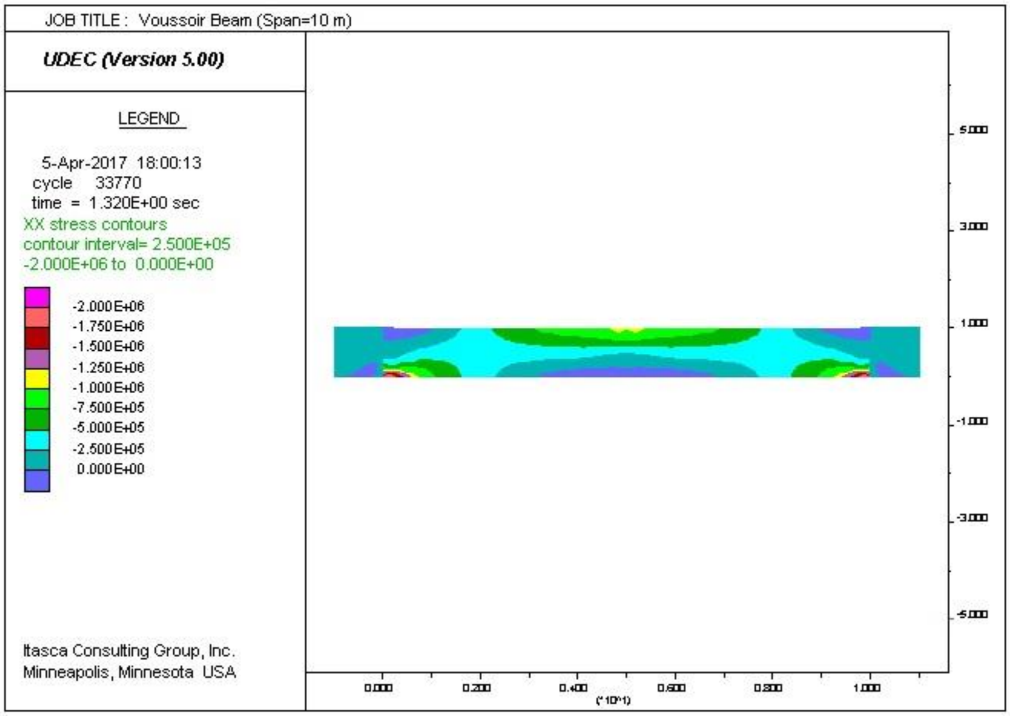

Figure 3.9 Stress contours within a voussoir beam (Unit B rock mass, span=10m, thickness=1m)

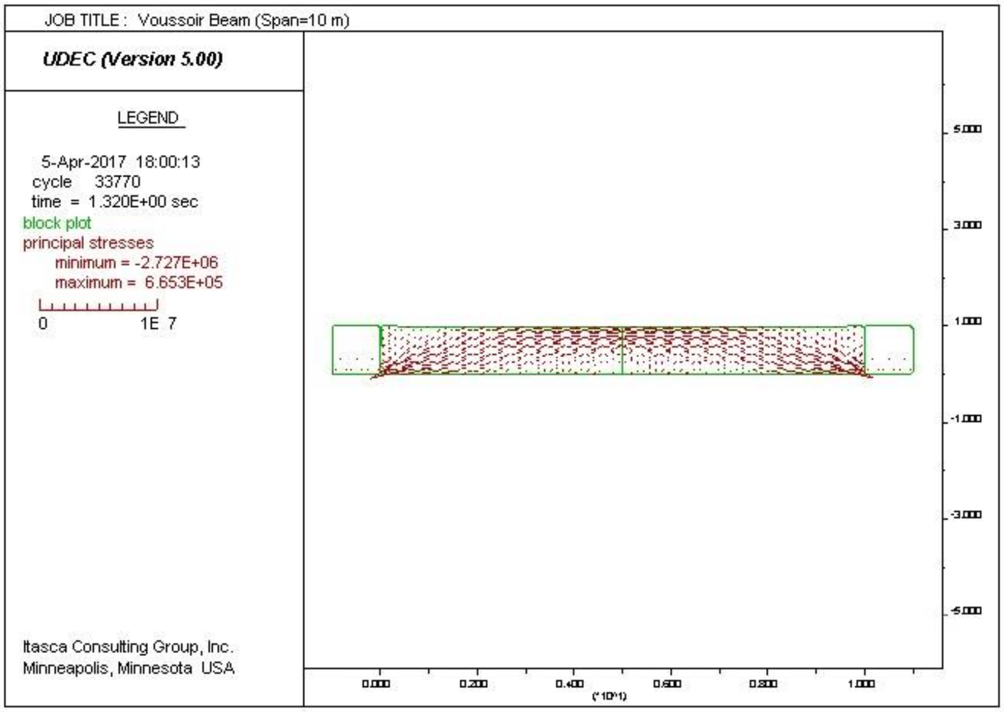

Figure 3.10 Principal stress distribution within a voussoir beam (Unit B rock mass, span=10m, thickness=1m)

The principal stress distribution is illustrated in Figure 3.10. It shows the arch structure generated within the beam, which leads to load transfer to the abutments. One could extract the values of axial stress within different cross-sections to plot the profile of stress through the beam.

To show process of stress distribution and examine accuracy of the assumptions, a wide range of span to thickness ratios are considered. Generally, a roof beam is expected to be stable from span to thickness ratio of 6 m to 18 m. Thus ratios of 6, 7.5, 10, 12.5, 15 and 18 are taken for each type of rock mass. They are taken in a way to cover different span and thickness values. Also three different sets of values are considered for ratios of 7.5 and 18, to clearly show that the results are not dependent on specific beam parameters. Table 3.4 summarizes selected span and thickness values for developed models.

Table 3.4 Geometry of beam models

Span/thickness ratio	Span (m)	Thickness (m)
6	12	2
7.5	15	2
7.5 (second case)	11.25	1.5
7.5 (third case)	7.5	1
10	10	1
12.5	18.75	1.5
15	15	1
18	9	0.5
18 (second case)	13.5	0.75
18 (third case)	18	1

Only compressive stresses are taken into account and half of the beam is examined (due to symmetry). Figure 3.11 to Figure 3.20 show the axial compressive stresses within each cross-section from left abutment to middle of the beam for all models.

The compressive stresses are concentrated at the lower part of the abutment in each model, whereas the top of the abutment is under tension. At the next cross-section, the bigger part of the thickness is under compression with less concentration. This is followed with the bigger part in the third section. At the next cross-section, the entire thickness is under compression and distribution gradually tends to be a rectangle. Towards the mid-span, the stresses tend to accumulate at the higher part of the thickness. Eventually, the stress distribution at the mid-span is exactly opposite of that at the abutment. The voussoir beam method assumed a linear triangular stress distribution at the abutments and mid-span. This assumption is not compatible with the results from numerical simulation, as the distribution is nonlinear.

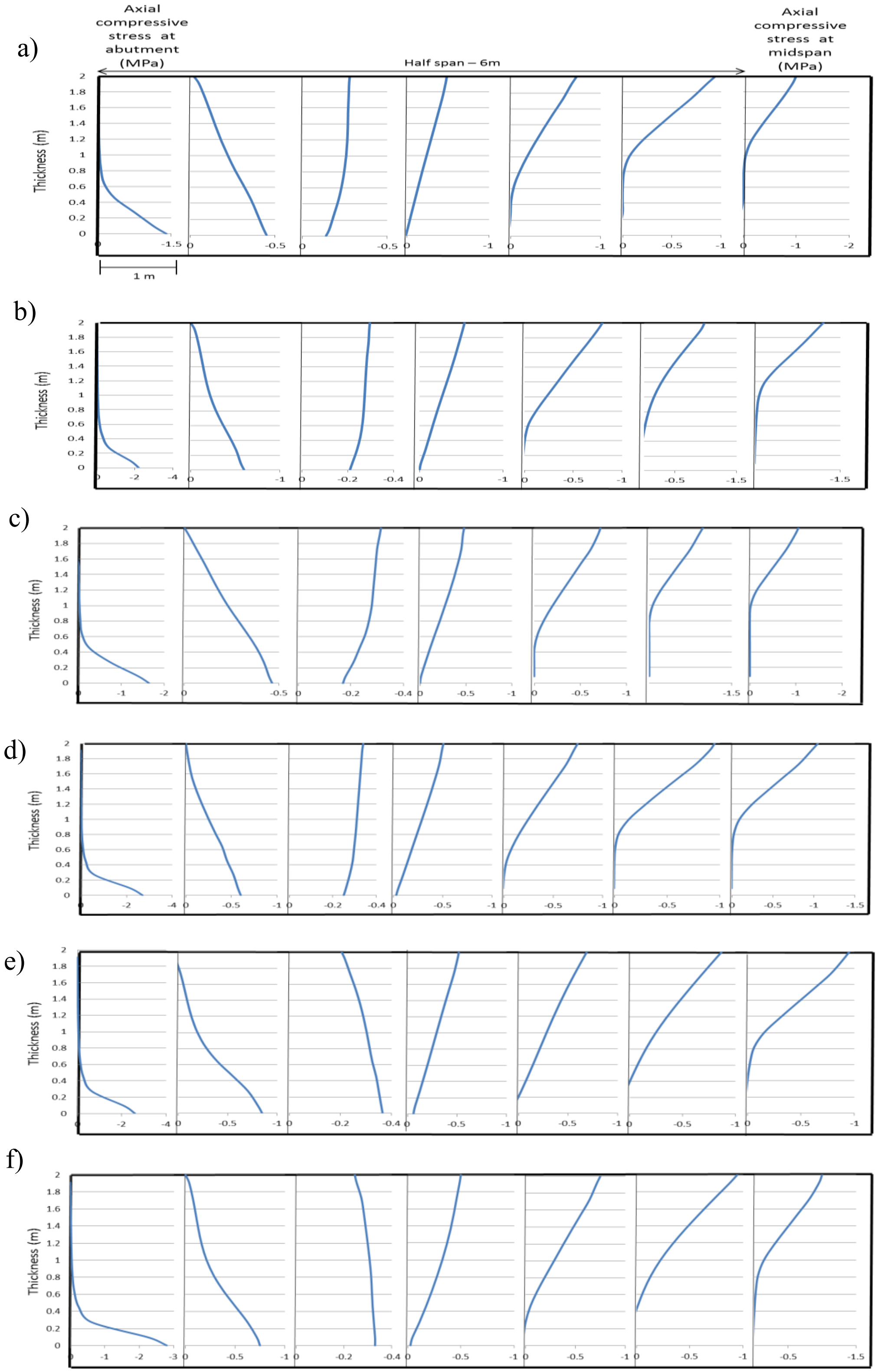

Figure 3.11 Profiles of compressive stresses within a beam with s=12m, t=2m; chalk (a) unit B (b) potash (c) unit A2 (d) limestone (e) dolostone (f)

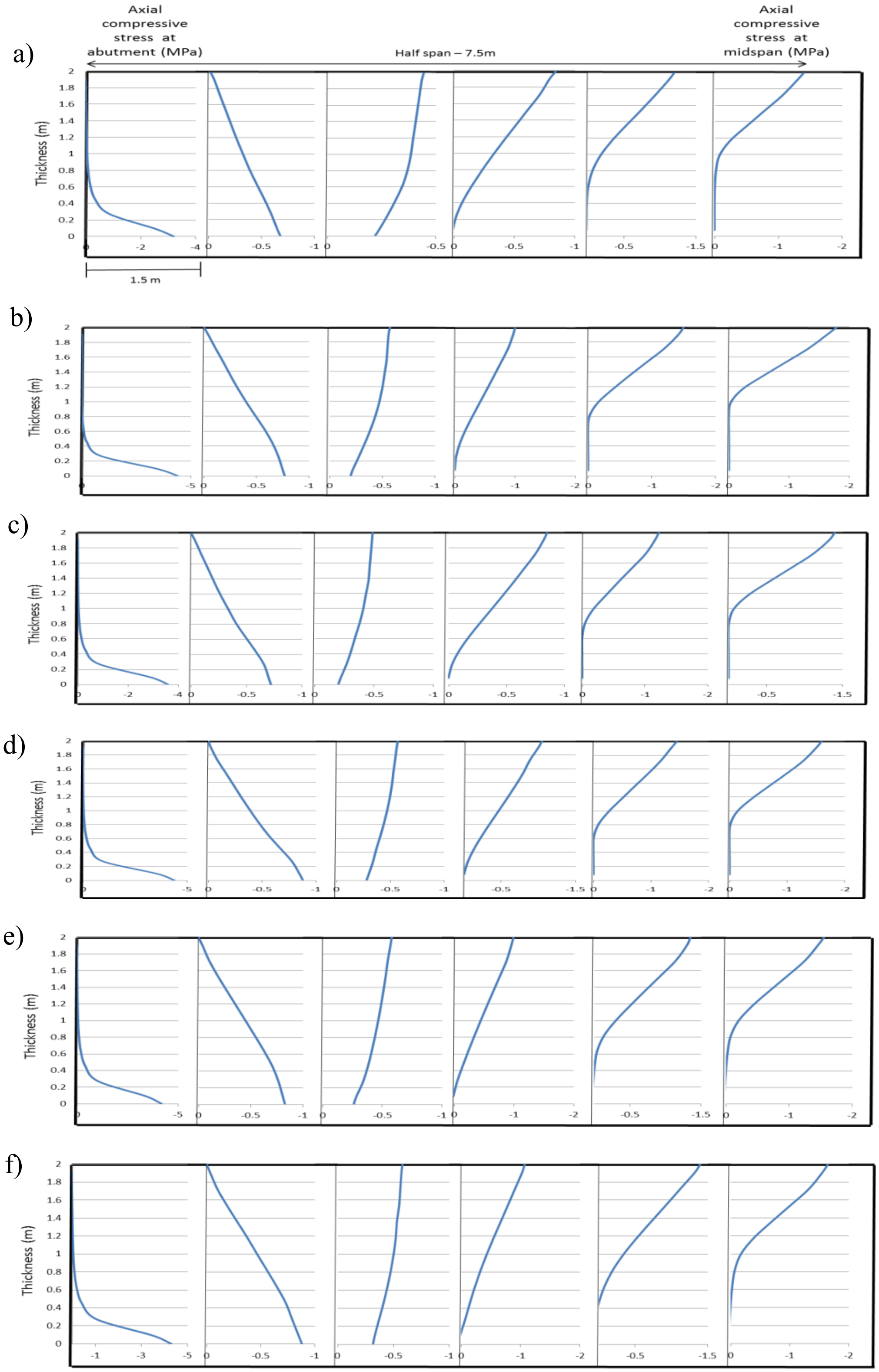

Figure 3.12 Profiles of compressive stresses within a beam with s=15m, t=2m; chalk (a) unit B (b) potash (c) unit A2 (d) limestone (e) dolostone (f)

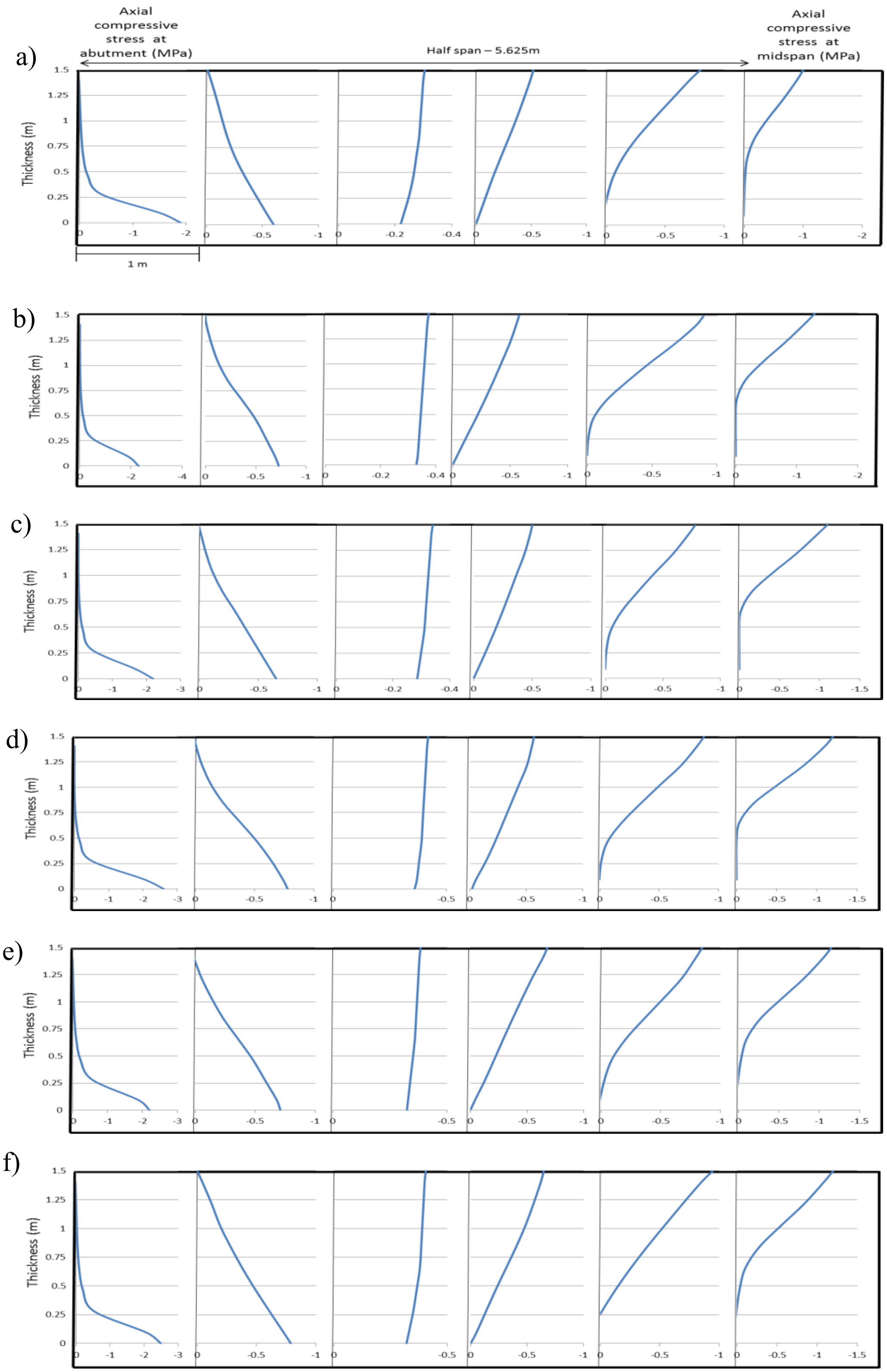

Figure 3.13 Profiles of compressive stresses within a beam with s=11.25m, t=1.5m; chalk (a) unit B (b) potash (c) unit A2 (d) limestone (e) dolostone (f)

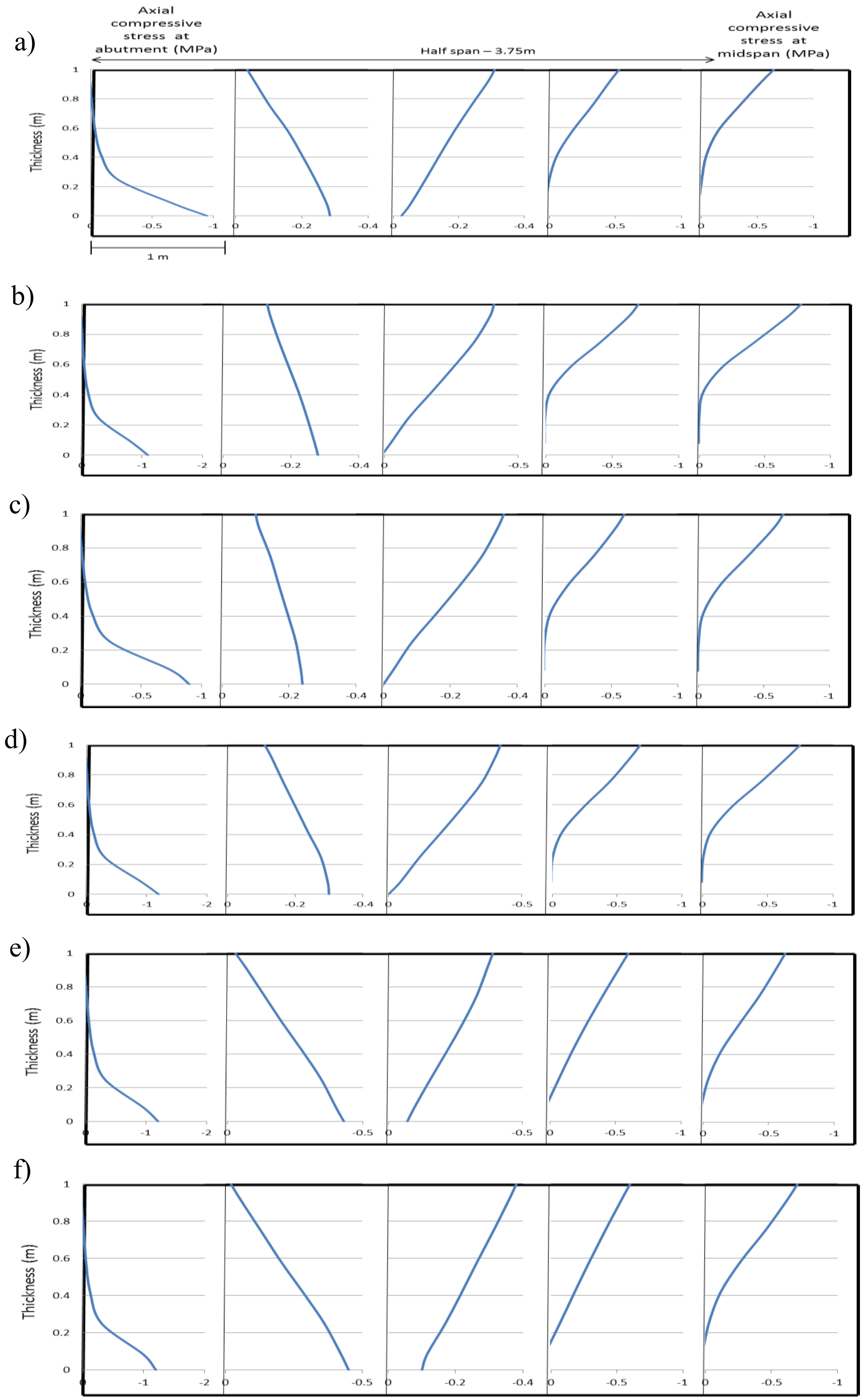

Figure 3.14 Profiles of compressive stresses within a beam with s=7.5m, t=1m; chalk (a) unit B (b) potash (c) unit A2 (d) limestone (e) dolostone (f)

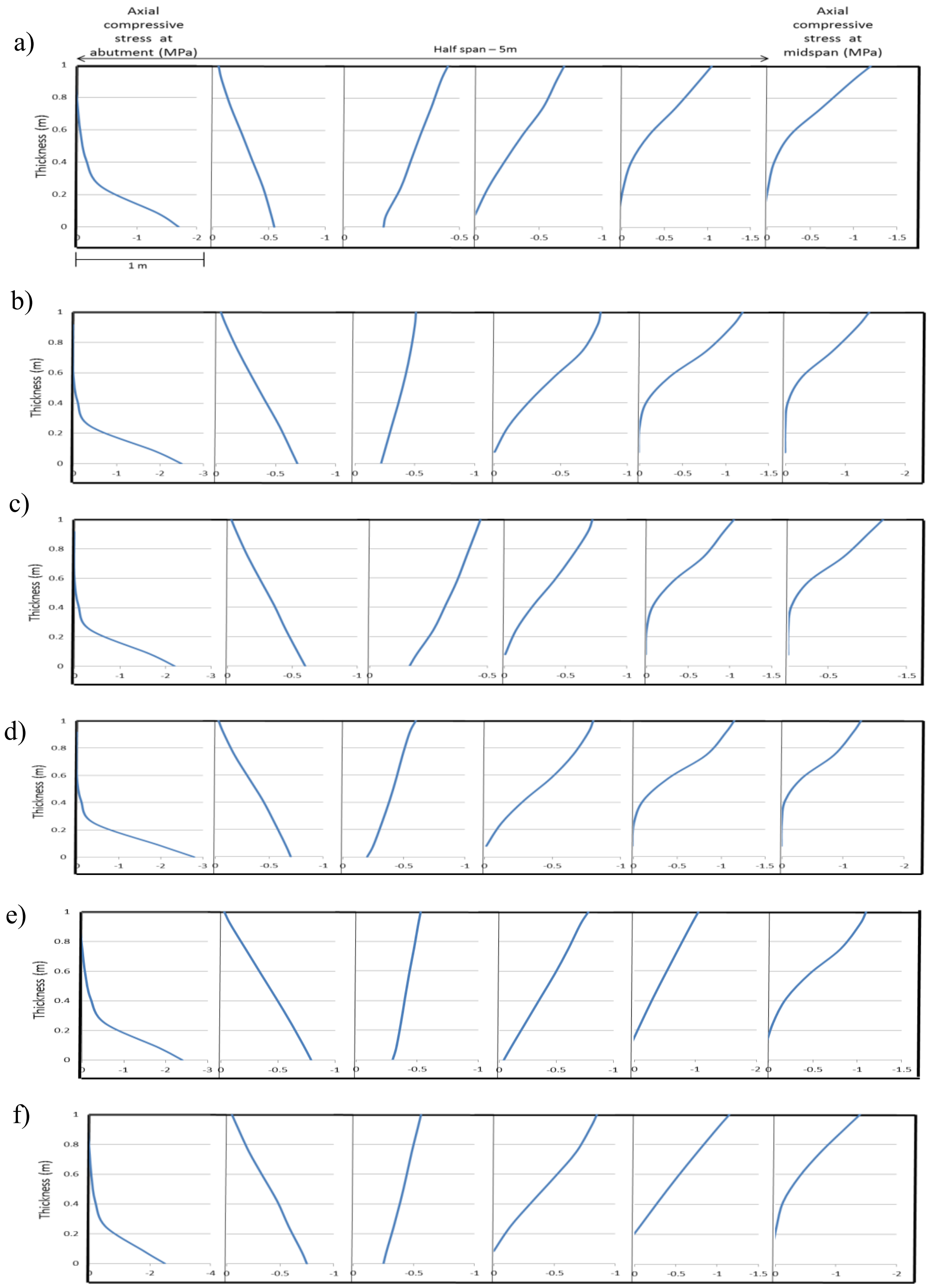

Figure 3.15 Profiles of compressive stresses within a beam with s=10m, t=1m; chalk (a) unit B (b) potash (c) unit A2 (d) limestone (e) dolostone (f)

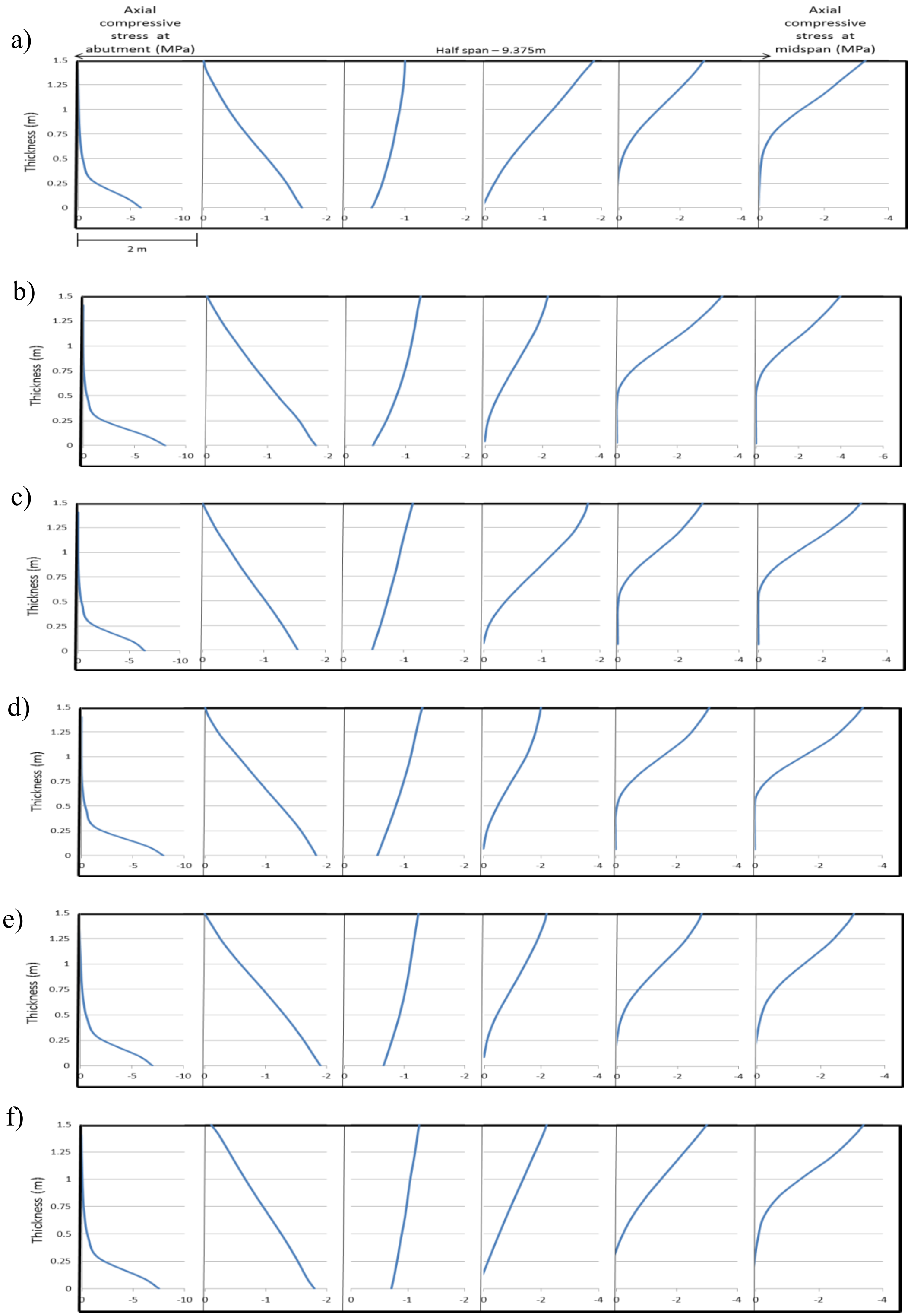

Figure 3.16 Profiles of compressive stresses within a beam with s=18.75m, t=1.5m; chalk (a) unit B (b) potash (c) unit A2 (d) limestone (e) dolostone (f)

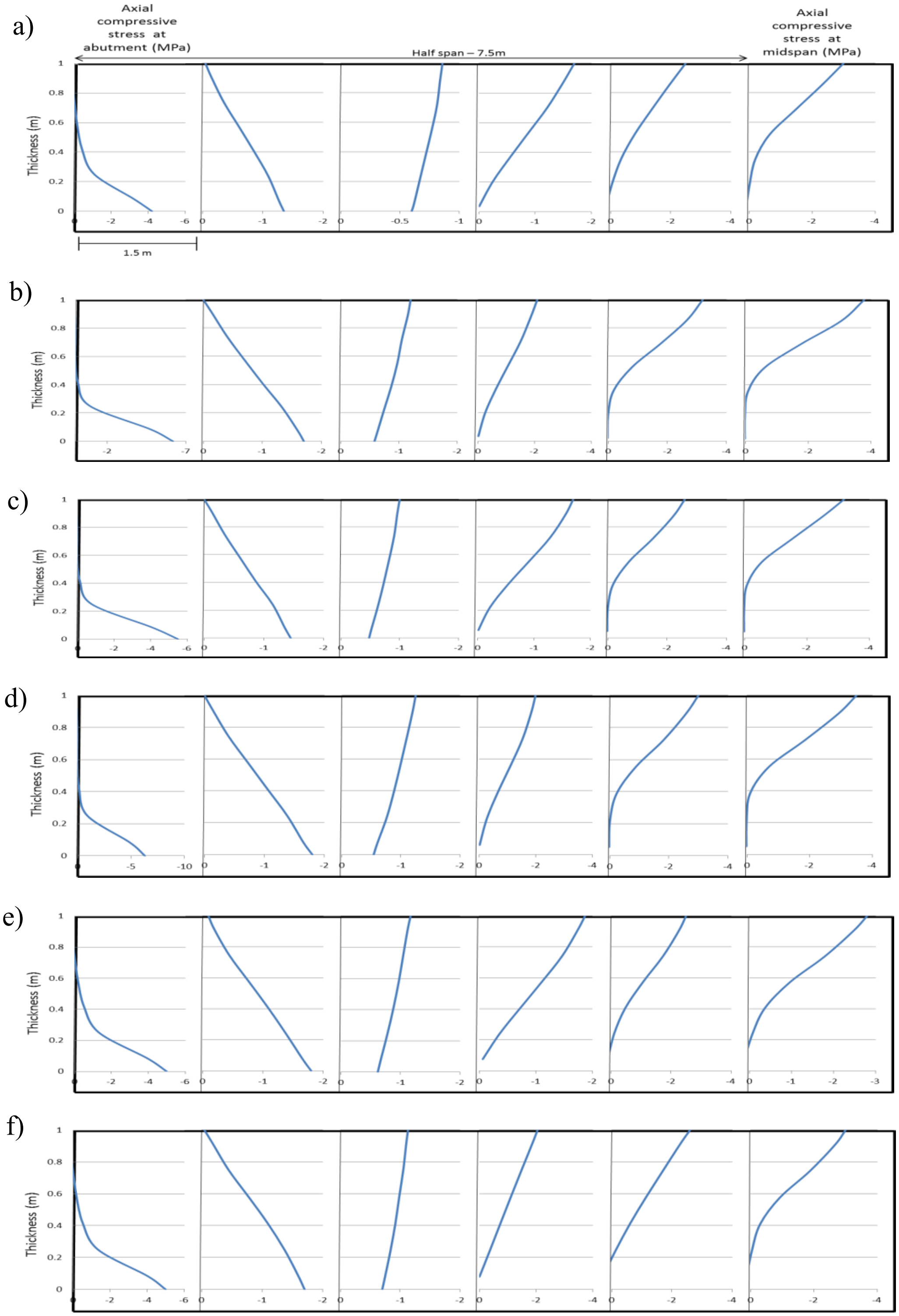

Figure 3.17 Profiles of compressive stresses within a beam with s=15m, t=1m; chalk (a) unit B (b) potash (c) unit A2 (d) limestone (e) dolostone (f)

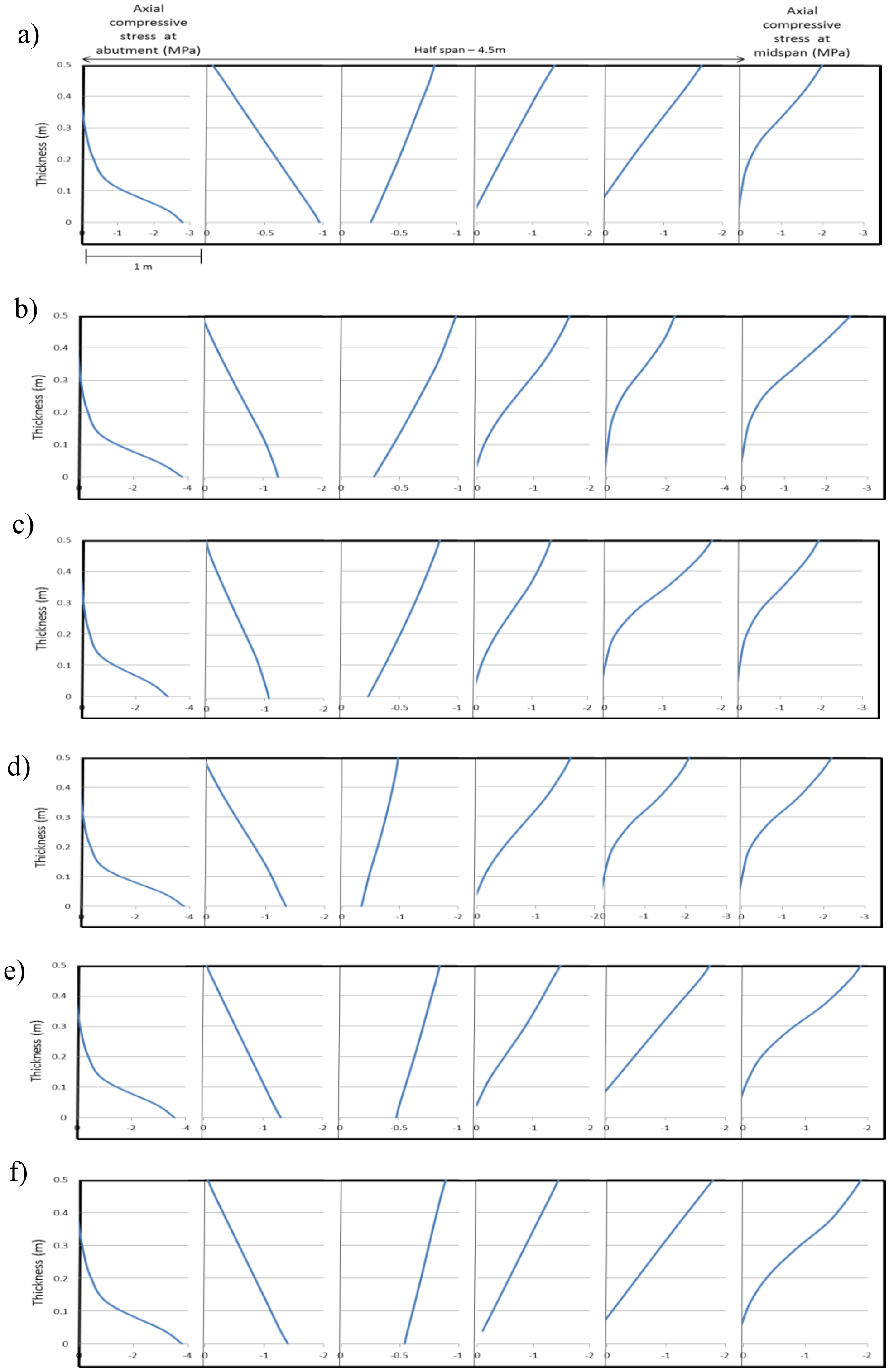

Figure 3.18 Profiles of compressive stresses within a beam with s=9m, t=0.5m; chalk (a) unit B (b) potash (c) unit A2 (d) limestone (e) dolostone (f)

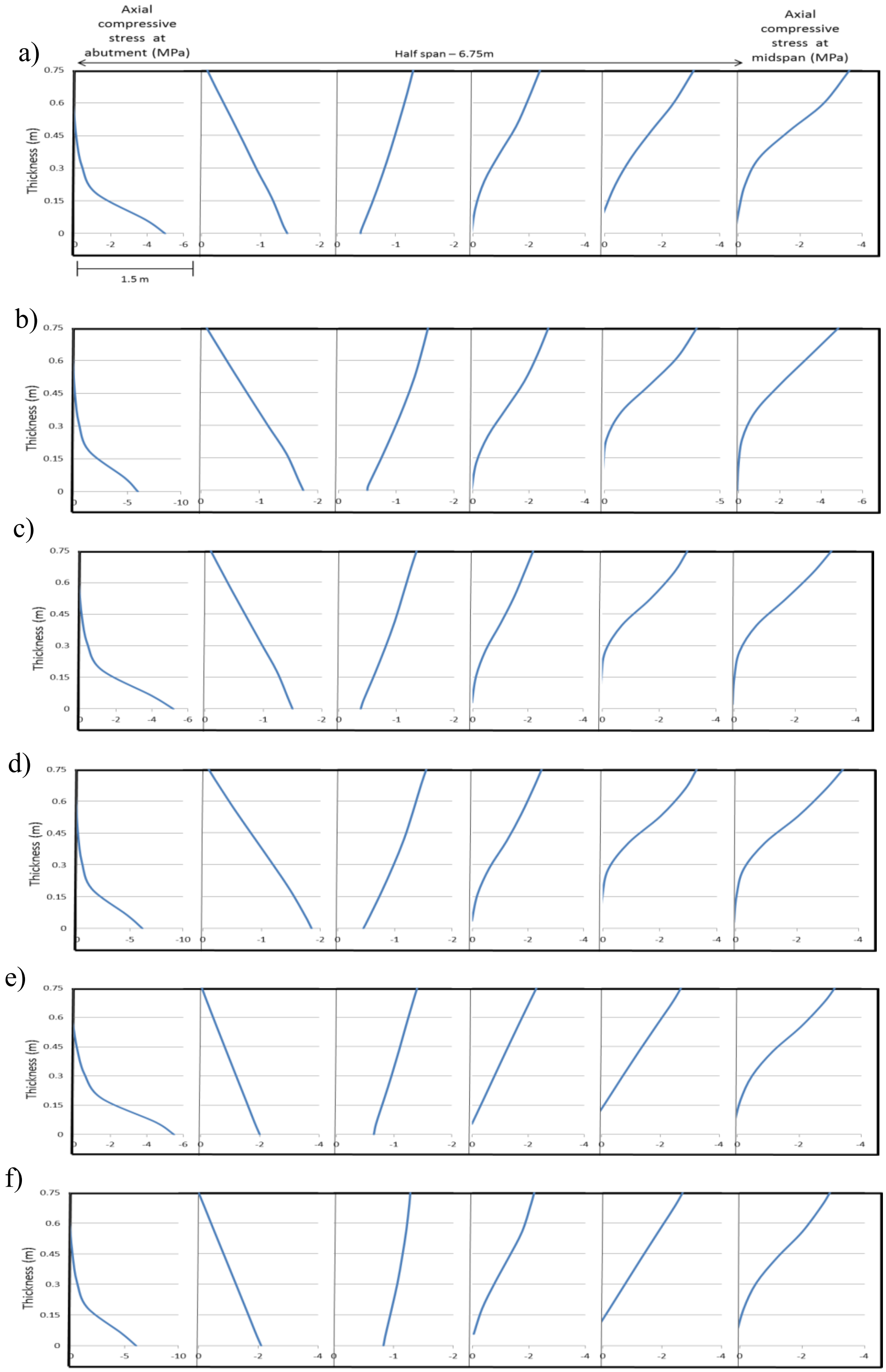

Figure 3.19 Profiles of compressive stresses within a beam with s=13.5m, t=0.75m; chalk (a) unit B (b) potash (c) unit A2 (d) limestone (e) dolostone (f)

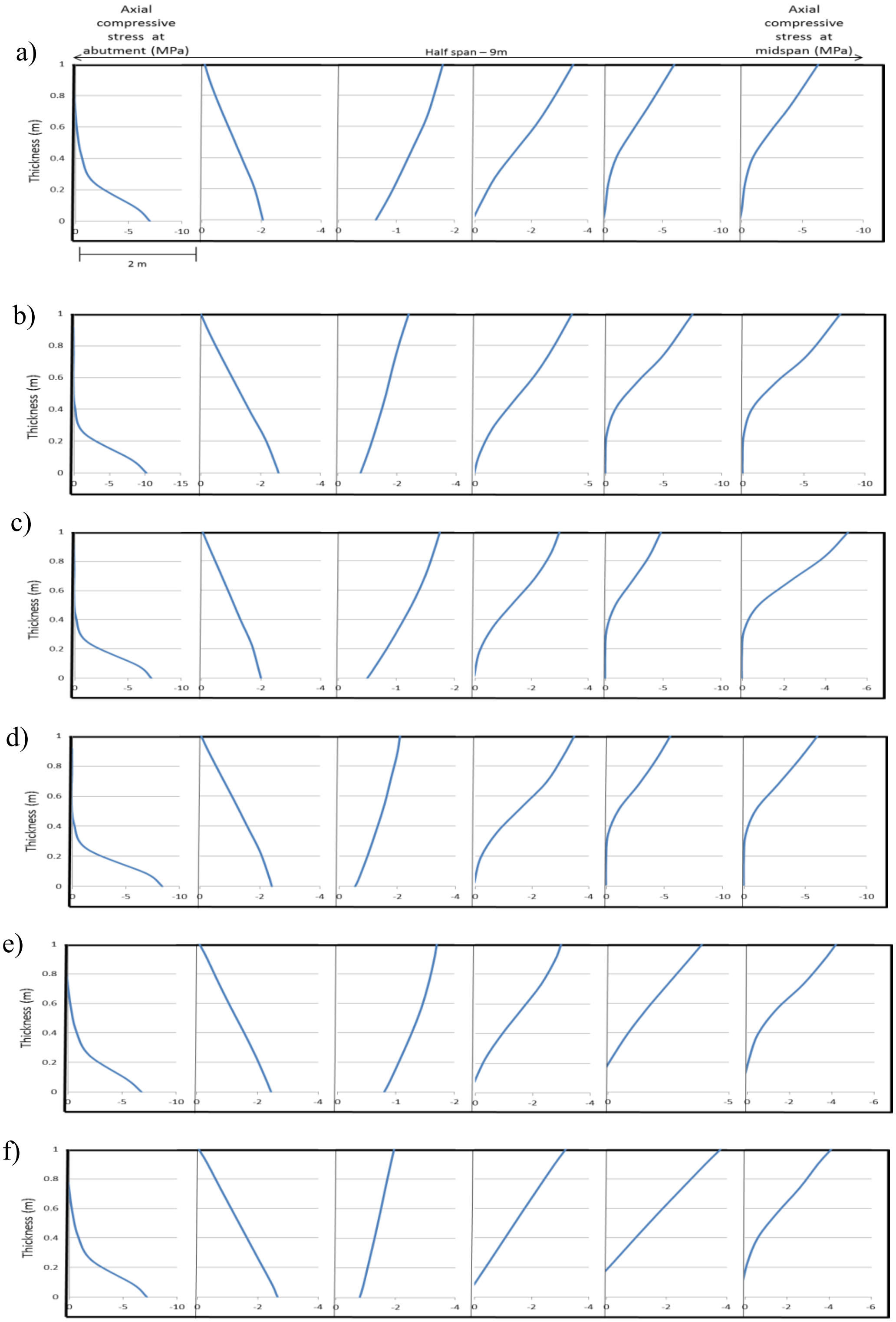

Figure 3.20 Profiles of compressive stresses within a beam with s=18m, t=1m; chalk (a) unit B (b) potash (c) unit A2 (d) limestone (e) dolostone (f)

If the stress distributions at each cross-section are taken as triangles and trapezoids, one could track locus of the centroids of each profile from abutment to middle of the beam. This would show the arch-shaped reaction line through the half beam. The locus of the centroids of triangles and trapezoids are depicted through Figure 3.21 to Figure 3.30. In the following figures data points are the calculated centroids and solid lines represent polynomial trendline. To keep the figures simple and clear, they are each divided into two plots. The first plot of each figure represents behavior of chalk, unit B and potash, while the second plot shows unit A2, limestone and dolostone rock masses.

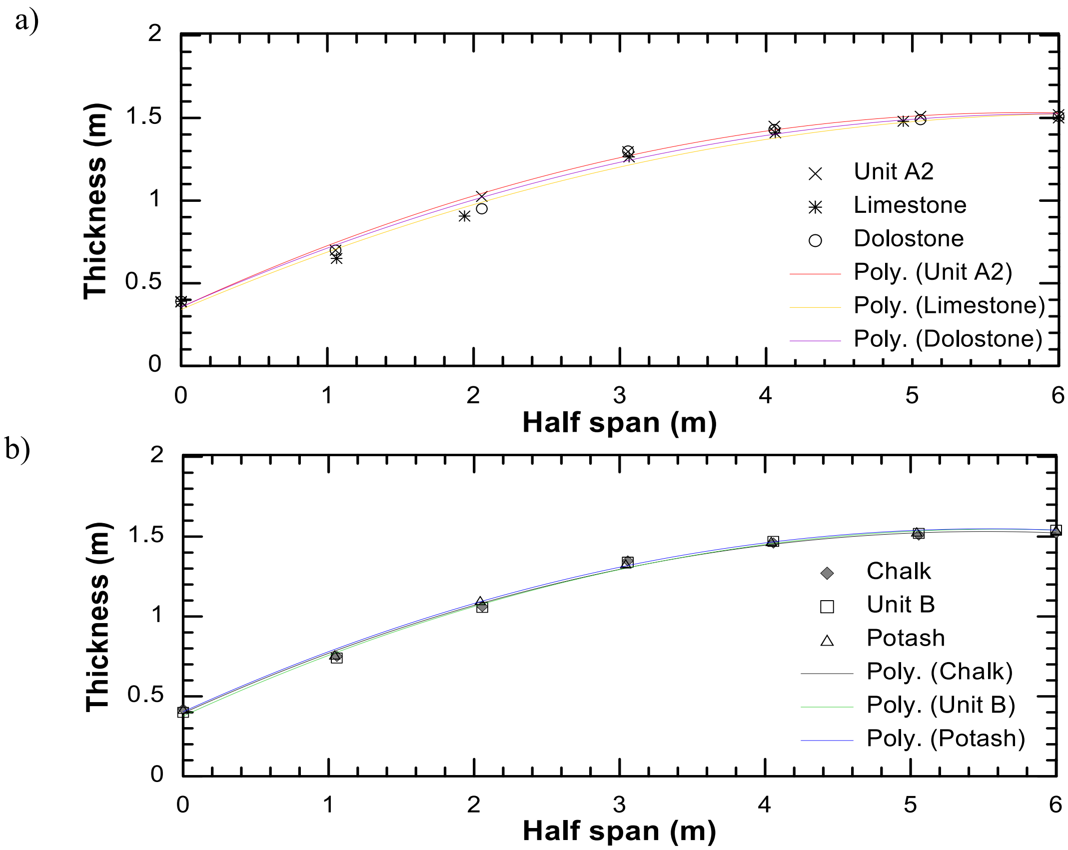

Figure 3.21 Stress reaction line within the half beam with s=12m, t=2m; chalk, unit B and potash (a) unit A2, limestone and dolostone (b)

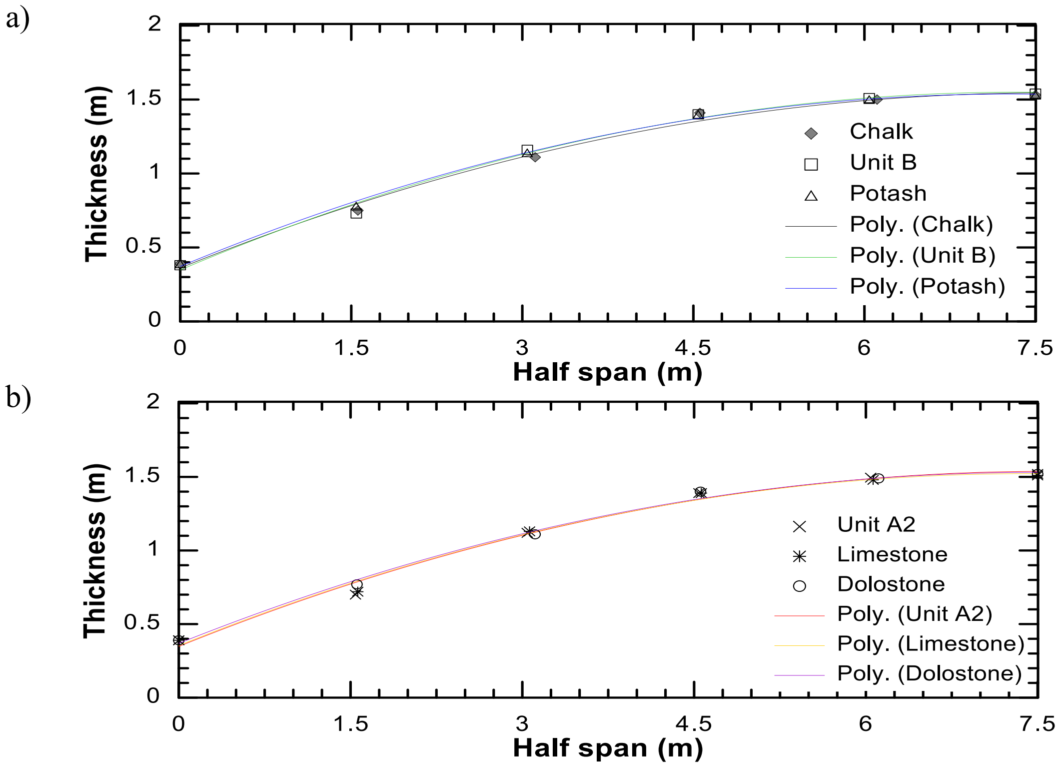

Figure 3.22 Stress reaction line within the half beam with s=15m, t=2m; chalk, unit B and potash (a) unit A2, limestone and dolostone (b)

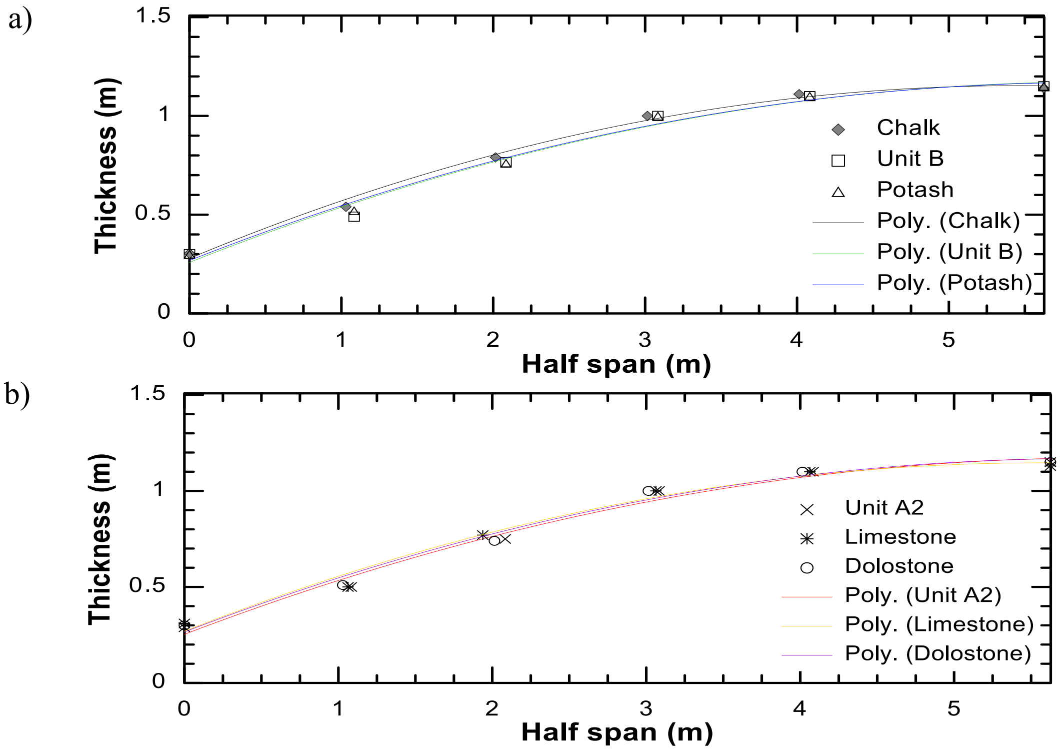

Figure 3.23 Stress reaction line within the half beam with s=11.25m, t=1.5m; chalk, unit B and potash (a) unit A2, limestone and dolostone (b)

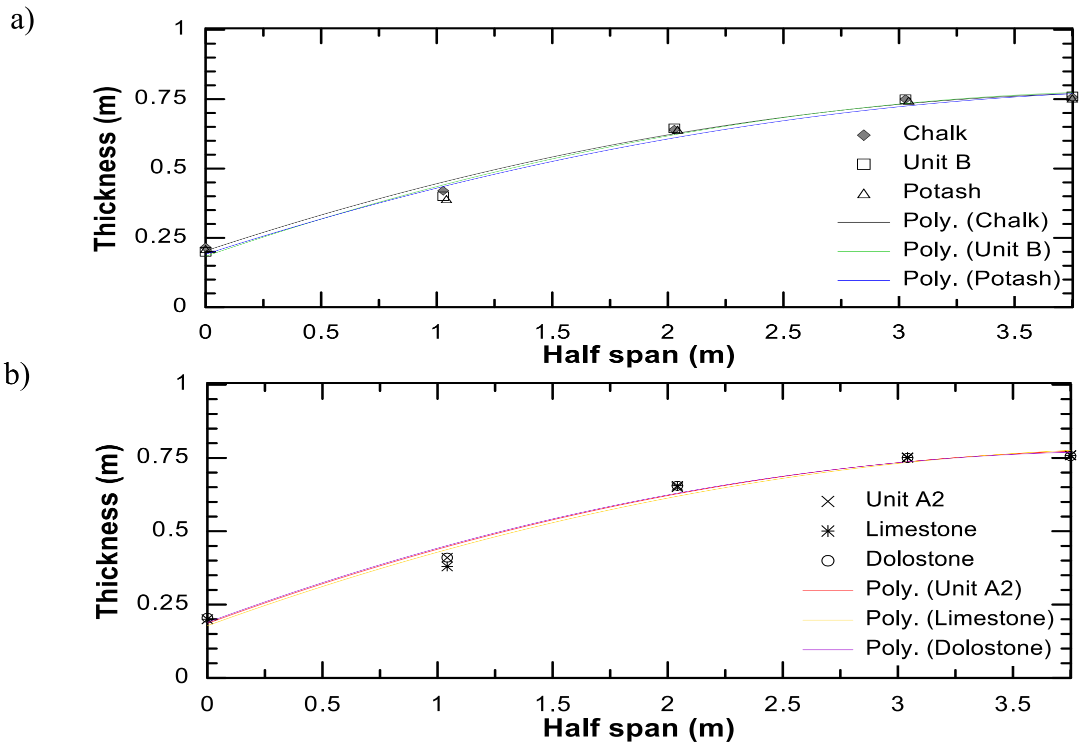

Figure 3.24 Stress reaction line within the half beam with s=7.5m, t=1m; chalk, unit B and potash (a) unit A2, limestone and dolostone (b)

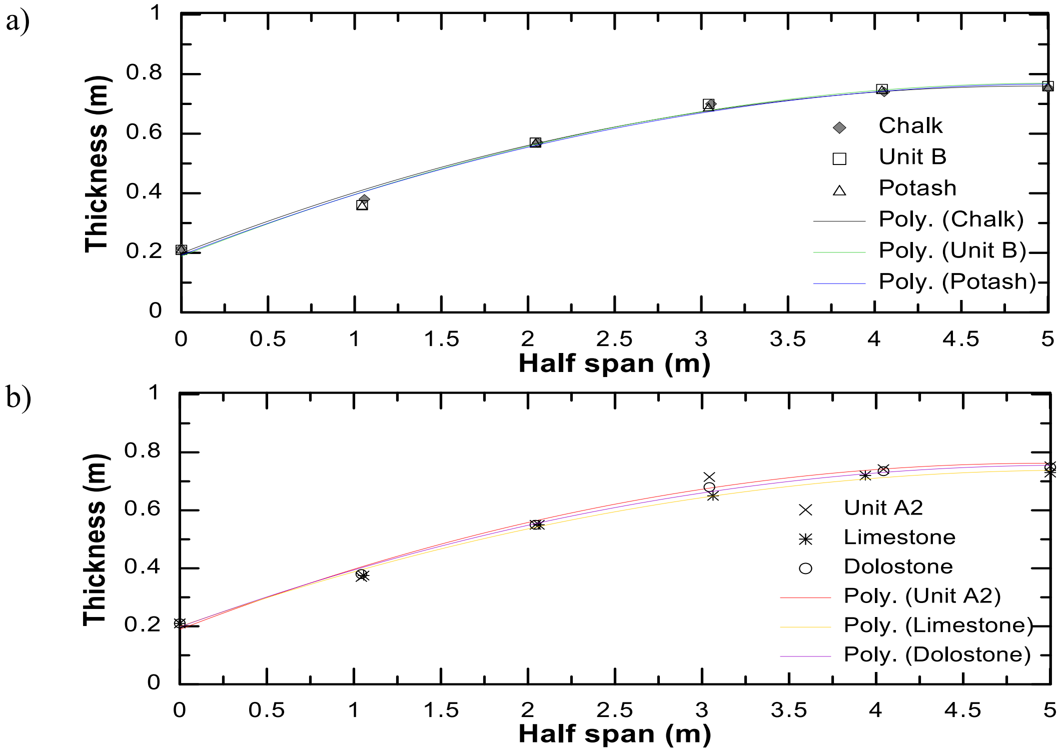

Figure 3.25 Stress reaction line within the half beam with s=10m, t=1m; chalk, unit B and potash (a) unit A2, limestone and dolostone (b)

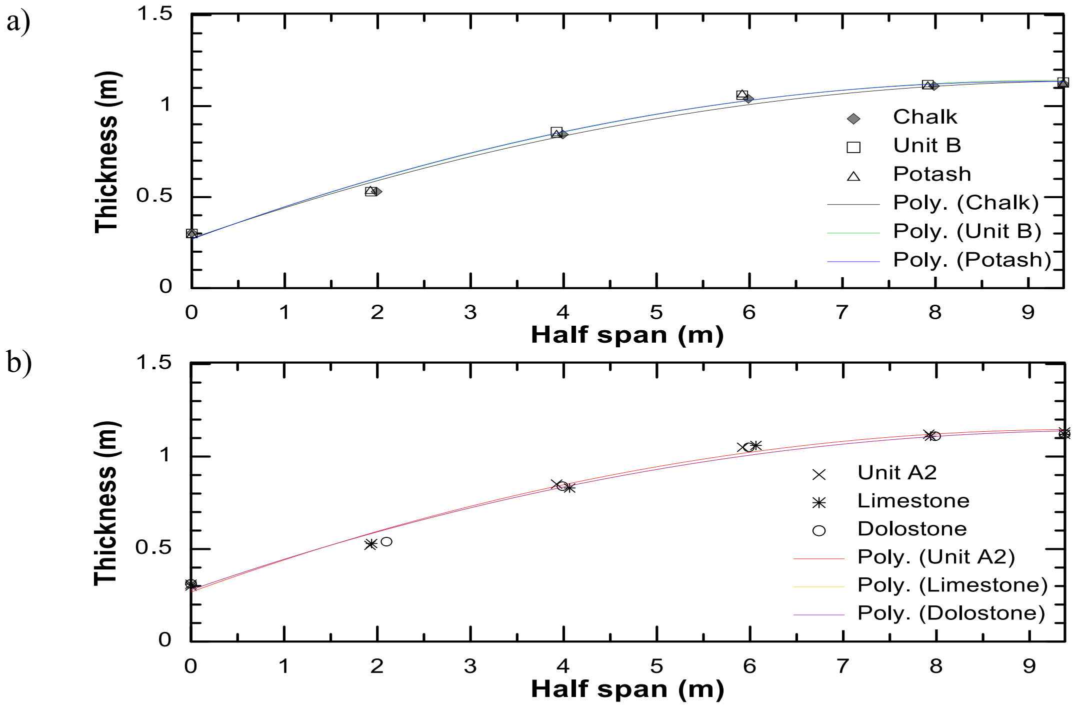

Figure 3.26 Stress reaction line within the half beam with s=18.75m, t=1.5m; chalk, unit B and potash (a) unit A2, limestone and dolostone (b)

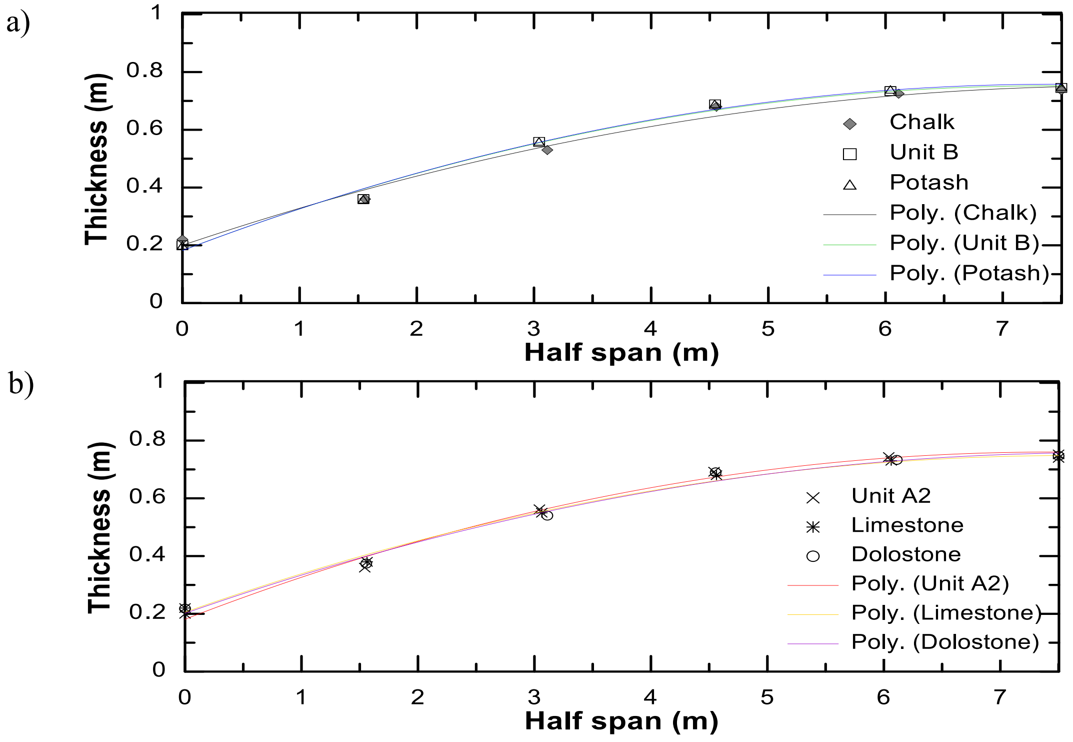

Figure 3.27 Stress reaction line within the half beam with s=15m, t=1m; chalk, unit B and potash (a) unit A2, limestone and dolostone (b)

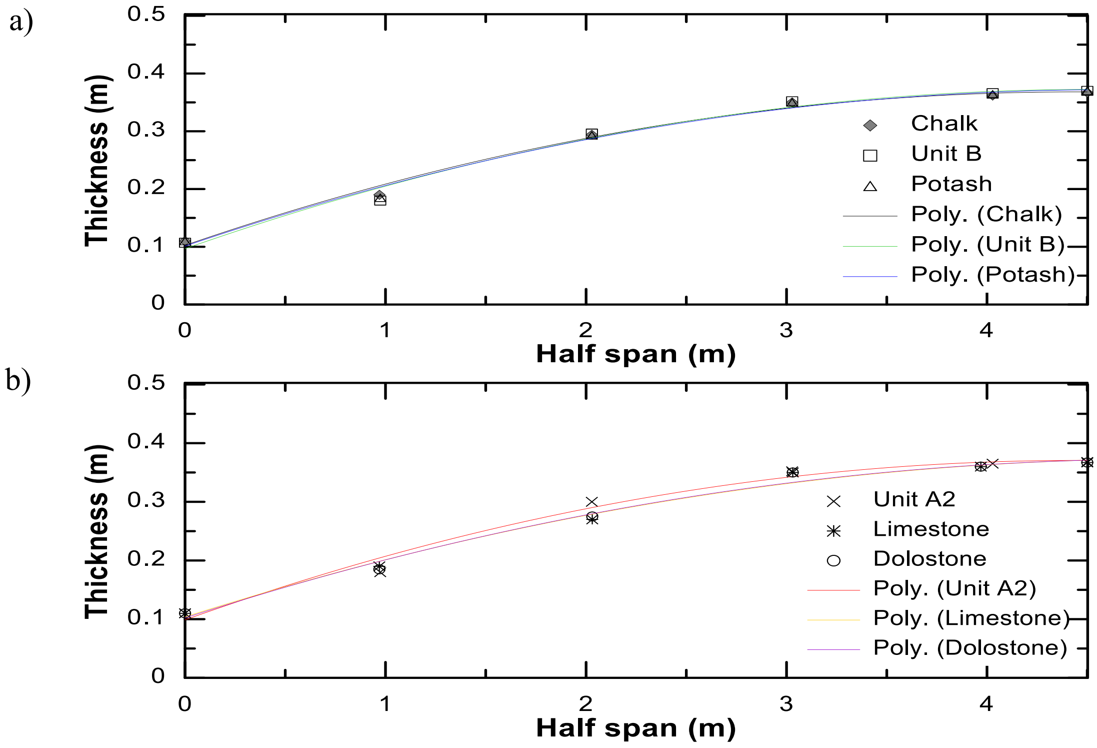

Figure 3.28 Stress reaction line within the half beam with s=9m, t=0.5m; chalk, unit B and potash (a) unit A2, limestone and dolostone (b)

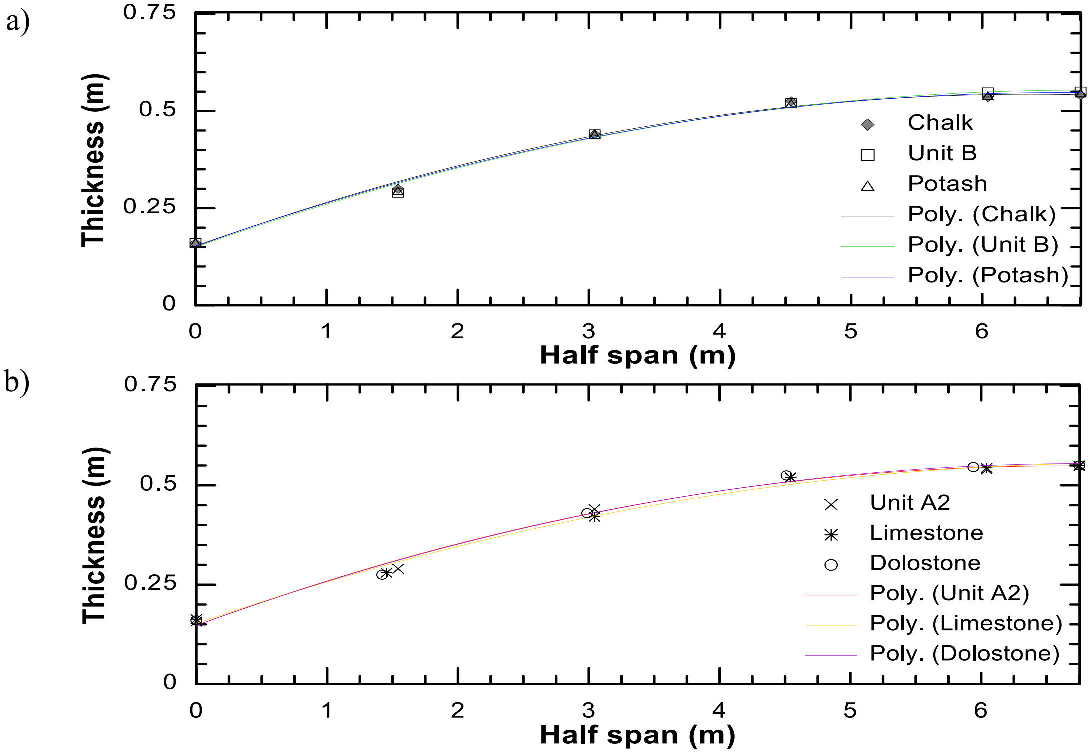

Figure 3.29 Stress reaction line within the half beam with s=13.5m, t=0.75m; chalk, unit B and potash (a) unit A2, limestone and dolostone (b)

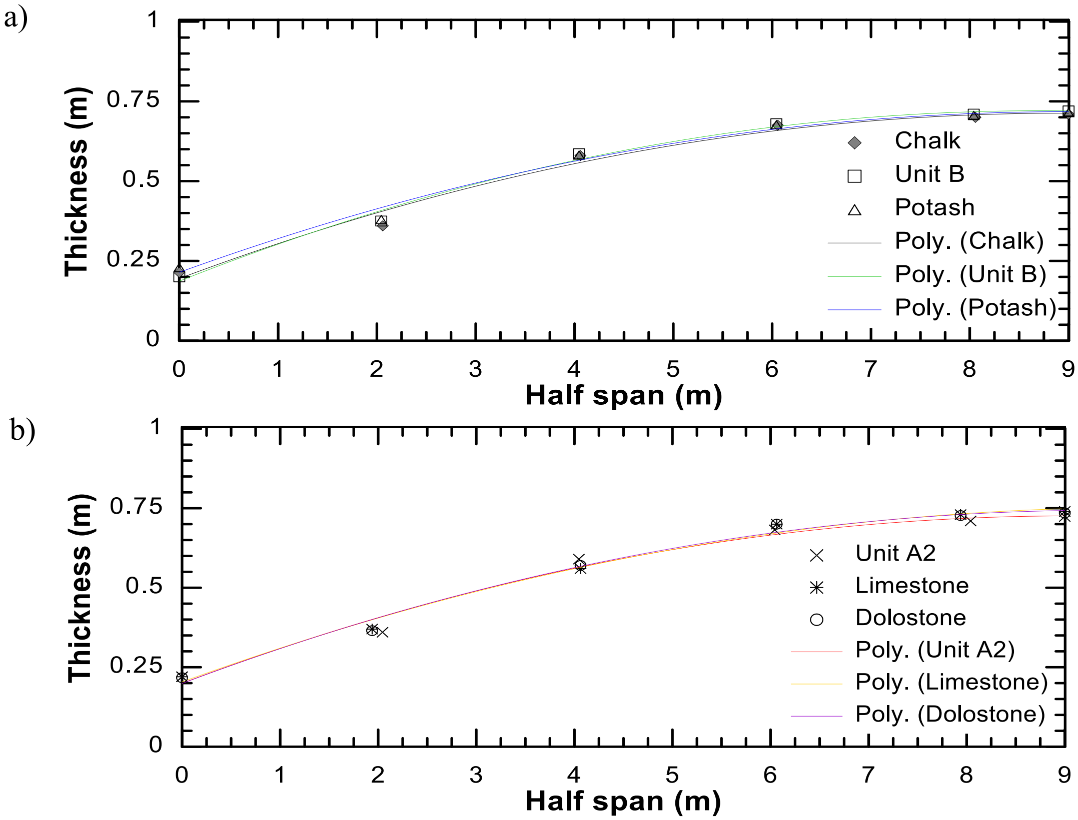

Figure 3.30 Stress reaction line within the half beam with s=18m, t=1m; chalk, unit B and potash (a) unit A2, limestone and dolostone (b)

Length of the arch within each beam can be found using figures of reaction line and compared with values that are obtained from voussoir calculations. Table 3.5 shows arch length values based on UDEC analysis and voussoir beam method. As this table shows, length of the arch within each voussoir beam is almost equal for a constant size of the beam and different types of rock masses. The difference among the values is less than 0.5%, so it only depends on size of the beam. Therefore a constant value is considered for each size, which is the average value of all rock types (Table 3.6). The formula that is used in voussoir beam method to calculate arch length is fairly accurate and gives consistent results with simulations. The error is less than 1% for all cases.

Table 3.5 Length of arch within the beams with different rock types and sizes

Beam model		r=6	r=7.5	r=7.5 (II)	r=7.5 (III)	r=10	r=12.5	r=15	r=18	r=18 (II)	r=18 (III)
UDEC	Chalk	12.3	15.24	11.44	7.6	10.08	18.86	15.04	9	13.5	18.04
	Unit B	12.32	15.28	11.48	7.54	10.2	18.96	15.12	9.02	13.6	18.04
	Potash	12.32	15.24	11.48	7.6	10.14	18.88	15.2	9.02	13.54	18.06
	Unit A2	12.32	15.24	11.6	7.56	10.3	19	15.06	9.16	13.6	18.02
	Limestone	12.3	15.2	11.44	7.62	10.08	18.82	15.12	9.02	13.54	18.06
	Dolostone	12.3	15.24	11.5	7.56	10.2	18.86	15.2	9.02	13.56	18.04
Voussoir beam	Chalk	12.23	15.19	11.39	7.59	10.07	18.86	15.07	9.03	13.55	18.08
	Unit B	12.23	15.19	11.39	7.59	10.07	18.86	15.06	9.03	13.55	18.07
	Potash	12.22	15.18	11.39	7.59	10.07	18.85	15.06	9.02	13.54	18.06
	Unit A2	12.22	15.18	11.39	7.59	10.07	18.84	15.05	9.02	13.54	18.05
	Limestone	12.22	15.18	11.38	7.59	10.07	18.84	15.05	9.02	13.53	18.04
	Dolostone	12.22	15.18	11.38	7.59	10.07	18.83	15.05	9.02	13.53	18.04

Table 3.6 Average of arch length within the beams

Beam model	Arch length (UDEC)	Arch length (voussoir beam)	Error (%)
r=6	12.310	12.224	0.699
r=7.5	15.240	15.183	0.374
r=7.5 (II)	11.490	11.386	0.905
r=7.5 (III)	7.580	7.59	0.132
r=10	10.167	10.07	0.951
r=12.5	18.897	18.845	0.273
r=15	15.123	15.055	0.452
r=18	9.040	9.023	0.188
r=18 (II)	13.557	13.539	0.130
r=18 (III)	18.043	18.058	0.081

Also, compressive stress values can be obtained at the centroids of each section. This leads to the internal stress distribution within the beam (Figure 3.31 to Figure 3.40). As these figures show, the maximum value of stress is at the abutment, while the minimum axial stress is at the left quarter of the beam close to the abutment. It also shows that the stress at the mid-span is not equal to the stress value at the abutment. This distribution of compressive stresses challenges the assumption of equal axial stresses at both abutments and mid-span in the voussoir method.

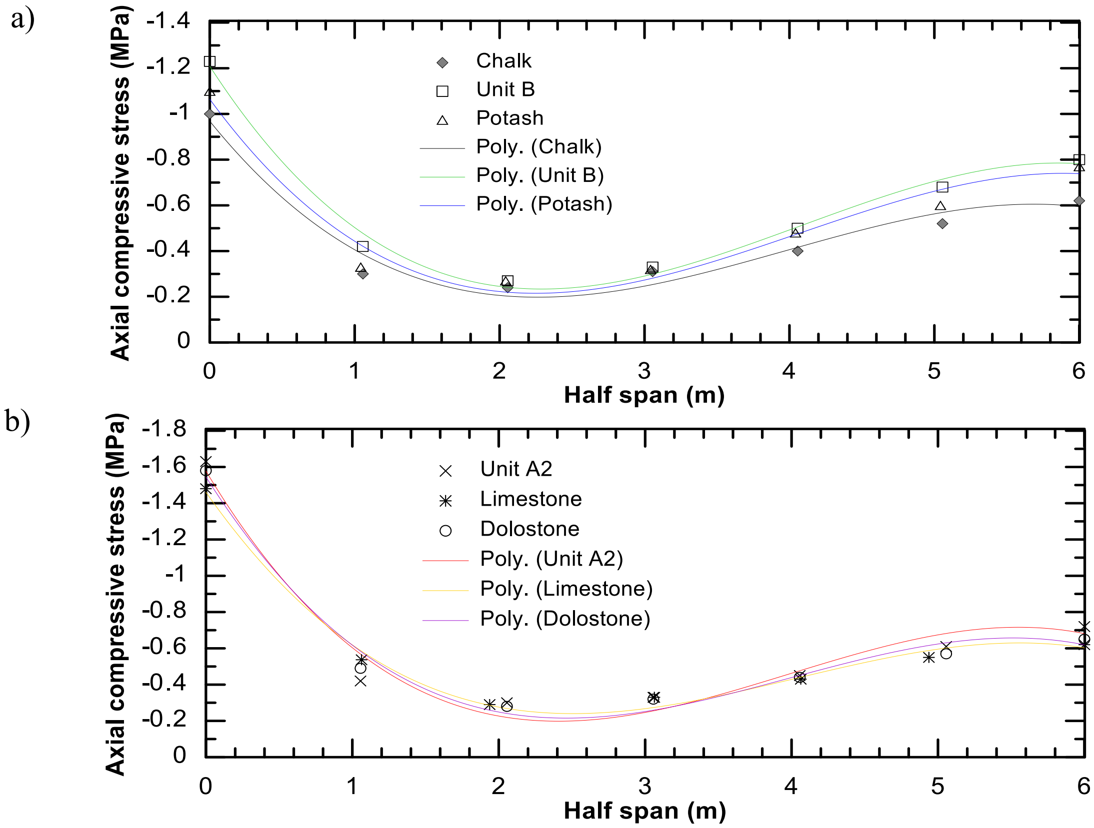

Figure 3.31 Internal axial stress distribution within the half beam with s=12m, t=2m; chalk, unit B and potash (a) unit A2, limestone and dolostone (b)

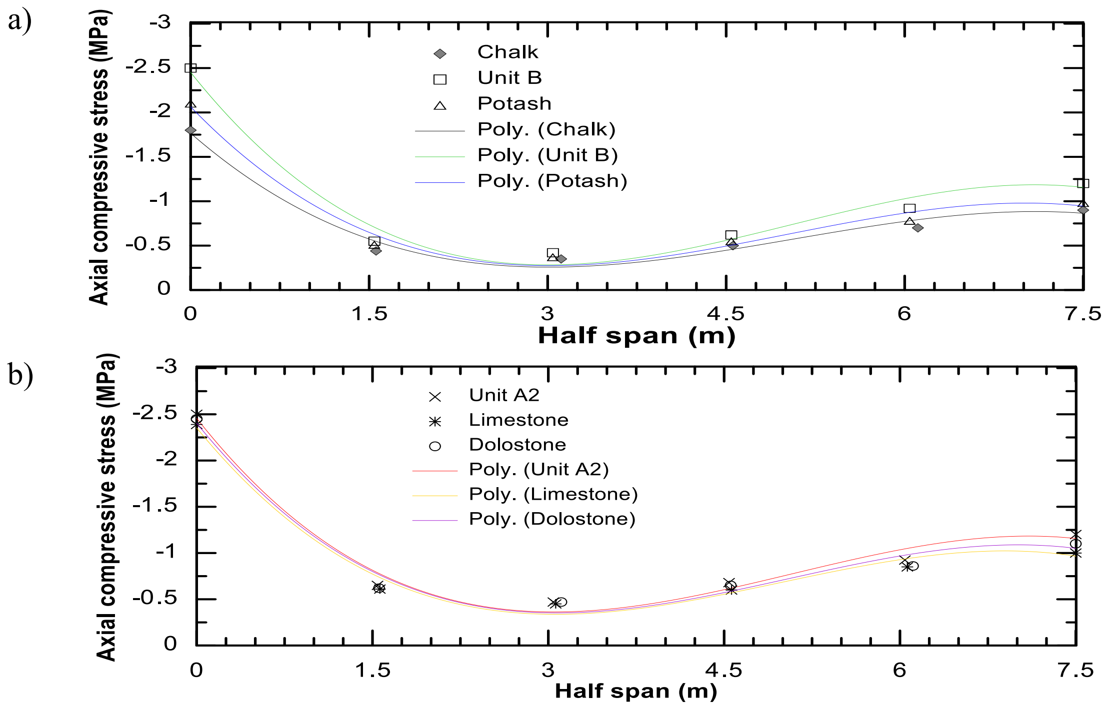

Figure 3.32 Internal axial stress distribution within the half beam with s=15m, t=2m; chalk, unit B and potash (a) unit A2, limestone and dolostone (b)

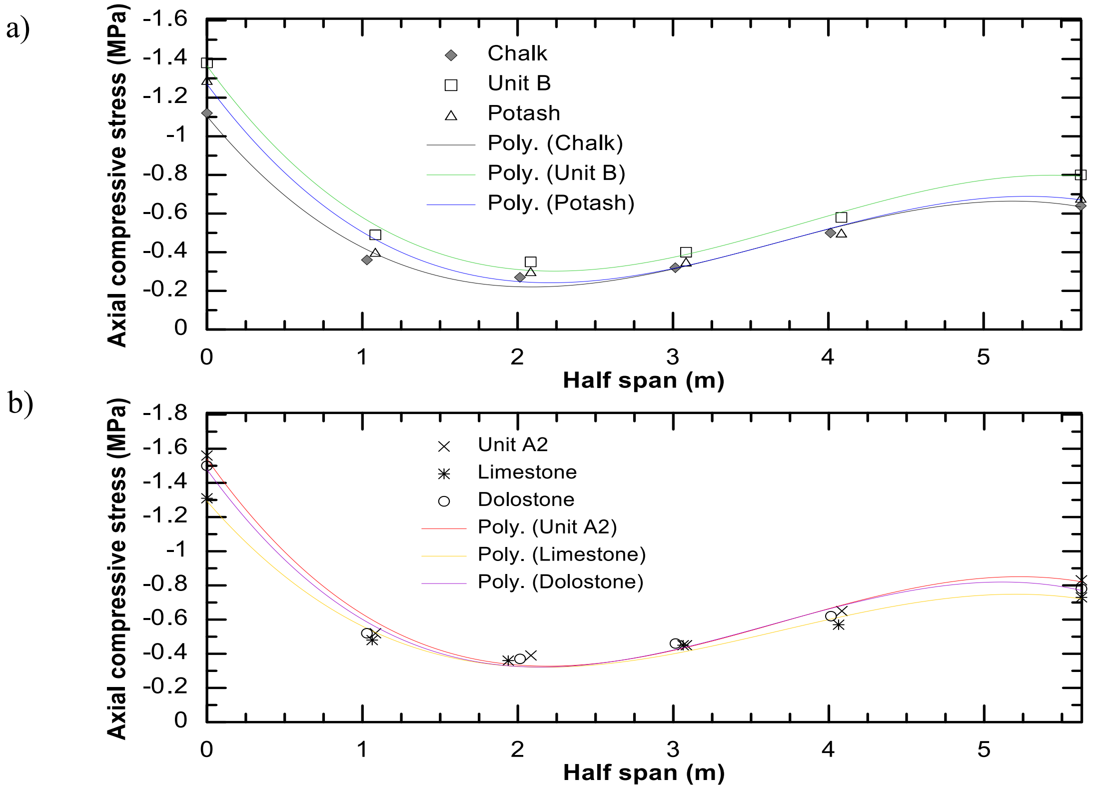

Figure 3.33 Internal axial stress distribution within the half beam with s=11.25m, t=1.5m; chalk, unit B and potash (a) unit A2, limestone and dolostone (b)

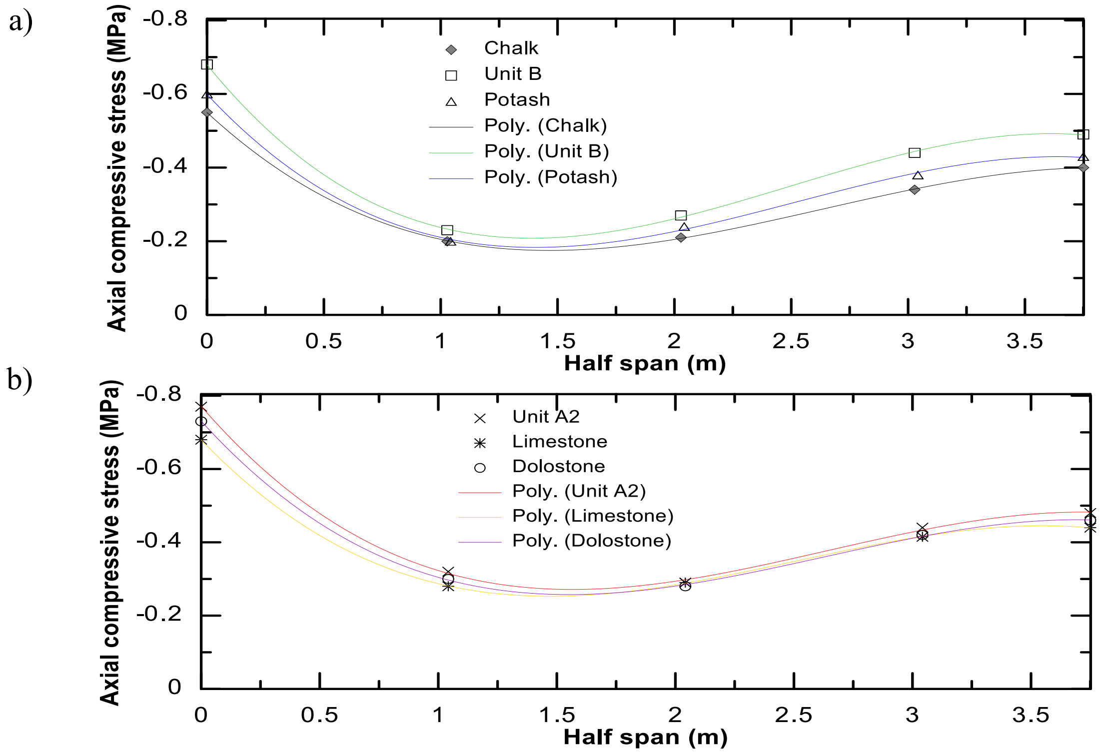

Figure 3.34 Internal axial stress distribution within the half beam with s=7.5m, t=1m; chalk, unit B and potash (a) unit A2, limestone and dolostone (b)

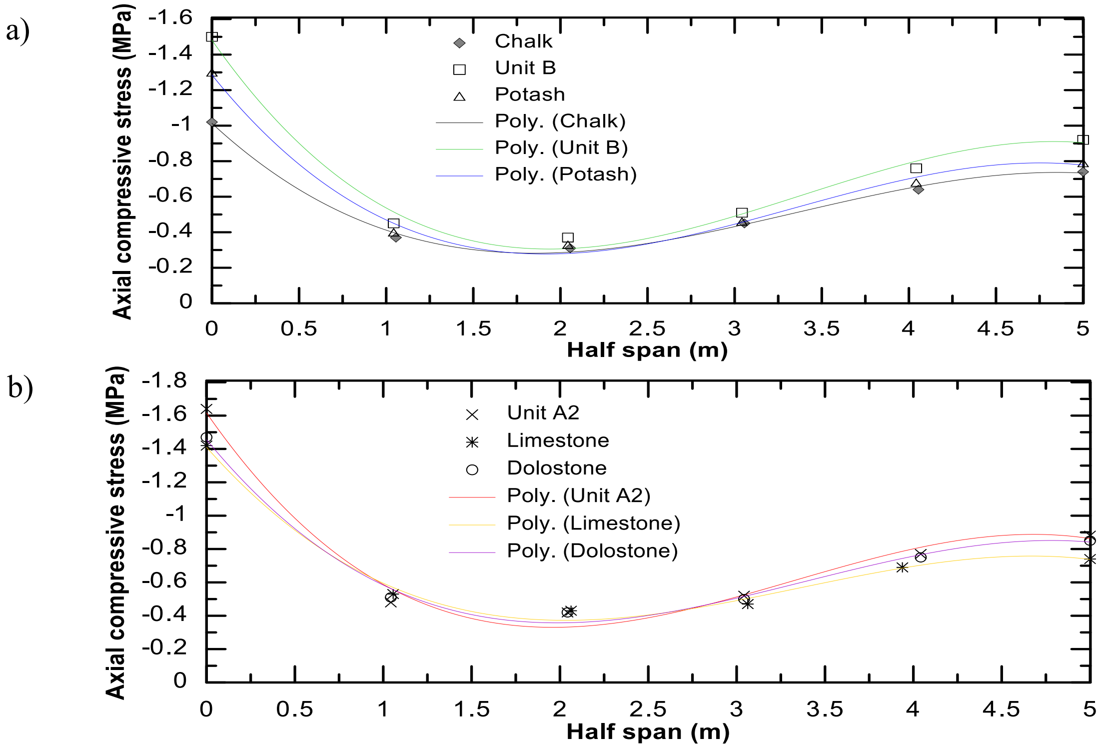

Figure 3.35 Internal axial stress distribution within the half beam with s=10m, t=1m; chalk, unit B and potash (a) unit A2, limestone and dolostone (b)

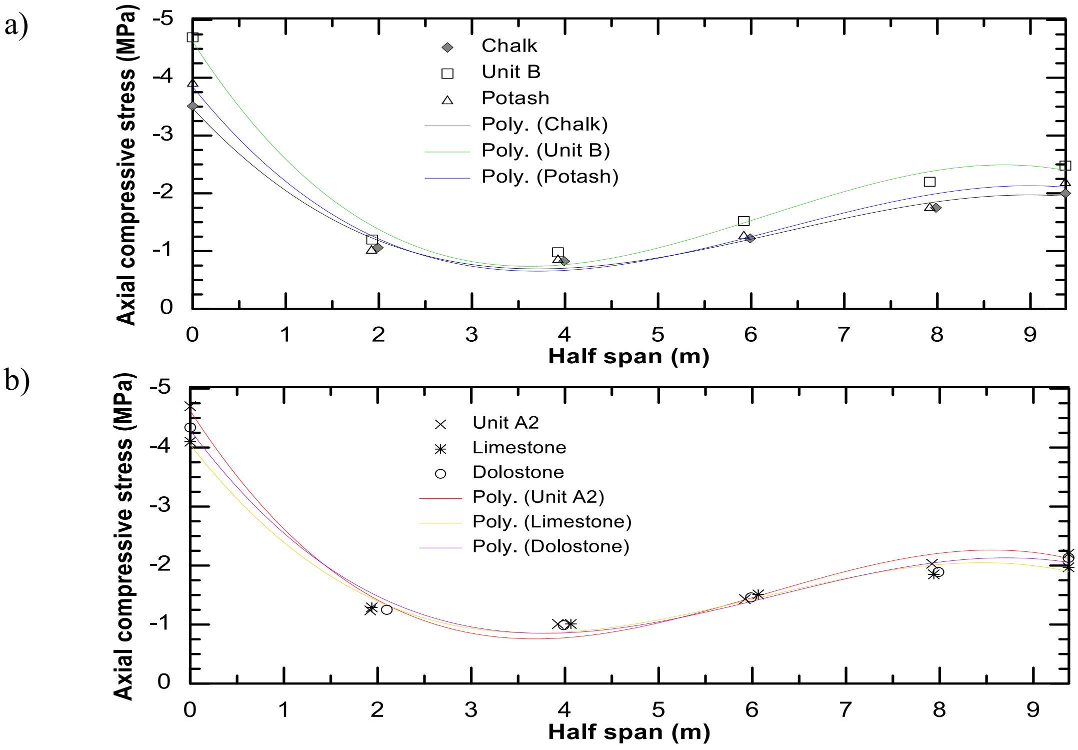

Figure 3.36 Internal axial stress distribution within the half beam with s=18.75m, t=1.5m; chalk, unit B and potash (a) unit A2, limestone and dolostone (b)

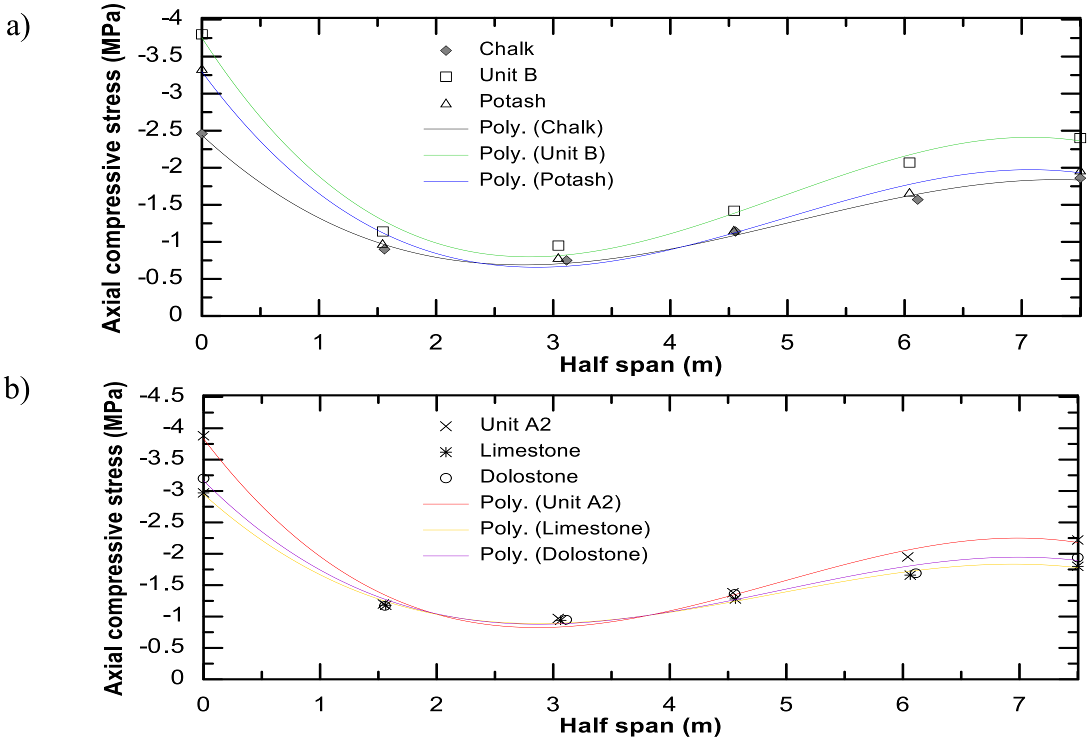

Figure 3.37 Internal axial stress distribution within the half beam with s=15m, t=1m; chalk, unit B and potash (a) unit A2, limestone and dolostone (b)

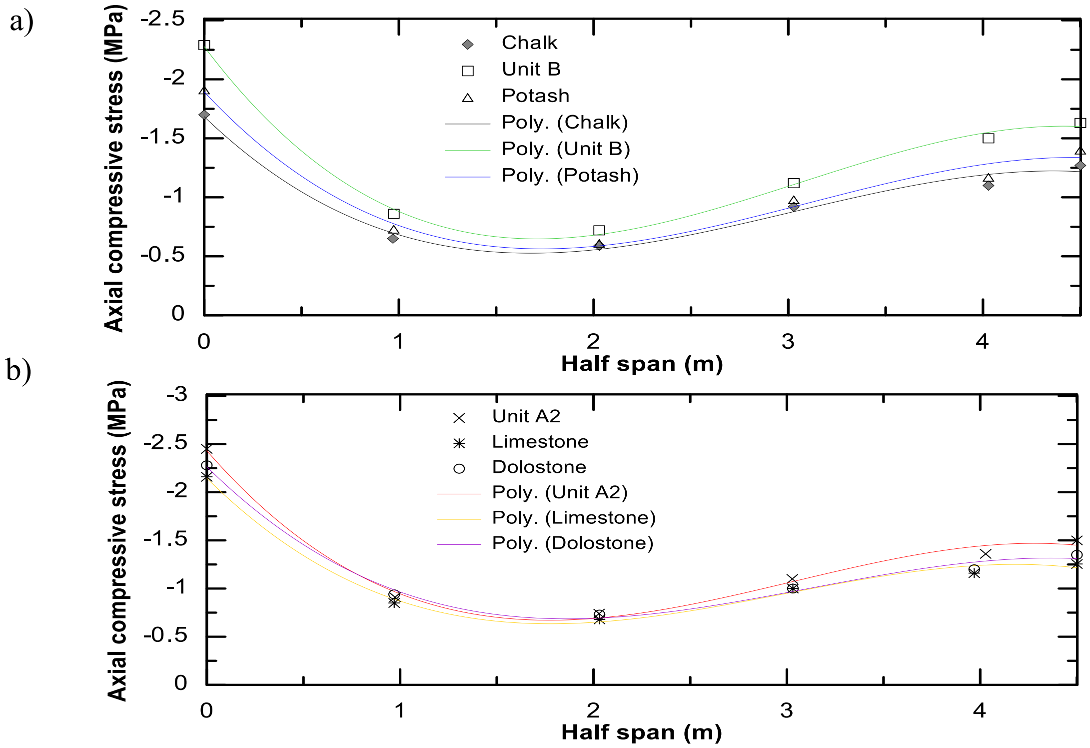

Figure 3.38 Internal axial stress distribution within the half beam with s=9m, t=0.5m; chalk, unit B and potash (a) unit A2, limestone and dolostone (b)

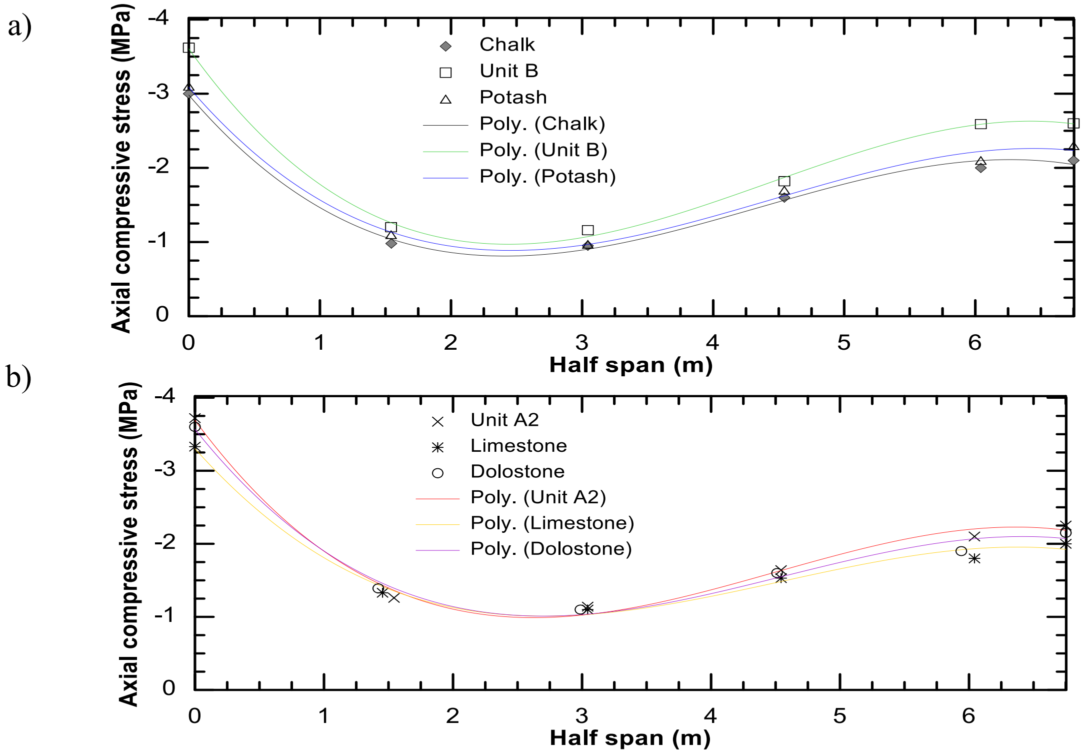

Figure 3.39 Internal axial stress distribution within the half beam with s=13.5m, t=0.75m; chalk, unit B and potash (a) unit A2, limestone and dolostone (b)

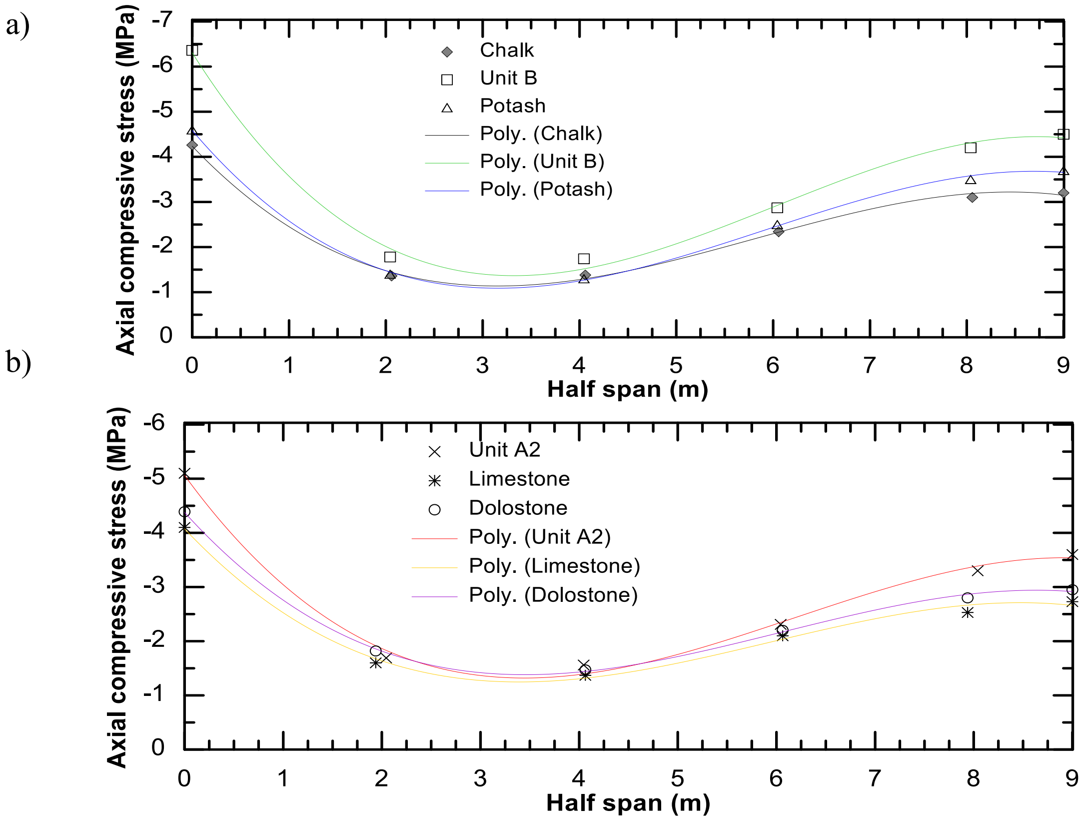

Figure 3.40 Internal axial stress distribution within the half beam with s=18m, t=1m; chalk, unit B and potash (a) unit A2, limestone and dolostone (b)

Table 3.7 and Table 3.8 show the percent difference between stress values at centroids of abutment and mid-span and percent difference between maximum and minimum stress values within half-beam, respectively. There is no discernible correlation among axial stress values for different types of material with a constant size. A beam with bigger size (higher span and thickness) generally gives higher difference between stress values at both sides, regardless of rock type. It means at constant thickness, beam with higher span leads to greater difference; also at constant span, beam with higher thickness gives greater difference. Same behavior can be found in Table 3.8. This behavior is generally valid but it cannot be applied for all the models as there are some exceptions.

Table 3.7 Percent difference between stress values at centroids of abutment and mid-span

Beam model	Chalk	Unit B	Potash	Unit A2	Limestone	Dolostone
r=6	46.91	42.36	35.29	77.45	81.90	83.41
r=7.5	66.67	70.27	72.73	70.27	82.01	76.06
r=7.5 (II)	54.55	53.21	61.93	61.09	56.86	63.16
r=7.5 (III)	31.58	32.48	33.01	46.40	42.86	45.38
r=10	31.82	47.93	48.80	60.32	62.96	53.45
r=12.5	54.81	61.84	56.21	72.46	70.18	68.32
r=15	27.78	45.16	51.60	54.43	49.06	49.03
r=18	28.96	33.67	30.82	48.10	53.00	51.24
r=18 (II)	35.29	32.80	29.63	49.25	49.91	50.43
r=18 (III)	28.42	34.25	21.69	34.48	40.12	39.24

Table 3.8 Percent difference between max and min stress values within half-beam

Beam model	Chalk	Unit B	Potash	Unit A2	Limestone	Dolostone
r=6	122.58	128.00	121.17	137.82	134.46	139.78
r=7.5	134.88	142.47	140.08	136.70	125.35	125.34
r=7.5 (II)	122.30	119.08	124.53	120.00	113.77	120.86
r=7.5 (III)	93.33	98.90	100.00	90.57	83.33	89.11
r=10	106.77	120.86	119.02	118.45	107.03	111.11
r=12.5	123.80	130.99	127.35	129.25	120.94	125.70
r=15	106.54	120.00	123.49	120.00	103.84	108.43
r=18	96.94	104.32	103.17	107.21	104.23	102.99
r=18 (II)	103.80	102.93	104.67	106.17	100.68	106.38
r=18 (III)	103.20	114.07	111.86	106.31	99.82	99.66

In voussoir beam method, distance of the cross-section with minimum stress value from mid-span is assumed to be $s/_{2\sqrt{2}}$; this value is shown in the last row of Table 3.9 for each beam size. As Table 3.9 shows, this parameter does not depend on type of the rock mass. At a constant size, the maximum difference among values of different rock types is 2.2%. Therefore one value can be considered for all rock masses as a constant size. Table 3.10 summarizes average distance of the minimum stress point from mid-span for each beam size based on UDEC and voussoir beam method. The results of voussoir beam are not consistent with simulations as the average error of results is 15.5%. This value must be modified in the equations. The last column of Table 3.10 shows the ratio of the UDEC to voussoir beam results. The average ratio is 0.866, which is equal to $\sqrt{0.75}$. The calculated values from voussoir beam must be multiplied by $\sqrt{0.75}$ to get accurate results. Thus, the distance would be changed to $\frac{s\sqrt{0.75}}{2\sqrt{2}}$.

Table 3.9 Distance of the minimum stress point from mid-span for all rock types and beam sizes

Beam model		r=6	r=7.5	r=7.5 II	r=7.5 III	r=10	r=12.5	r=15	r=18	r=18 II	r=18 III
UDEC	Chalk	3.70	4.50	3.52	2.36	3.06	5.66	4.68	2.74	4.22	5.72
	Unit B	3.68	4.40	3.47	2.35	3.05	5.70	4.67	2.71	4.21	5.71
	Potash	3.66	4.50	3.45	2.30	3.04	5.68	4.64	2.72	4.24	5.73
	Unit A2	3.64	4.48	3.46	2.27	3.03	5.66	4.65	2.69	4.17	5.70
	Lime-stone	3.62	4.44	3.50	2.28	3.00	5.63	4.60	2.71	4.14	5.68
	Dolo-stone	3.61	4.45	3.48	2.26	3.02	5.62	4.65	2.70	4.15	5.67
V-beam		4.24	5.3	3.98	2.65	3.53	6.63	5.3	3.18	4.77	6.36

Table 3.10 Average distance of the minimum stress point from mid-span

Beam model	Distance from mid-span (UDEC)	Distance from mid-span (voussoir beam)	Ratio
r=6	3.652	4.24	0.86
r=7.5	4.462	5.3	0.84
r=7.5 II	3.476	3.98	0.87
r=7.5 III	2.303	2.65	0.87
r=10	3.033	3.53	0.86
r=12.5	5.656	6.63	0.85
r=15	4.648	5.3	0.88
r=18	2.712	3.18	0.85
r=18 II	4.188	4.77	0.88
r=18 III	5.702	6.36	0.90
Average	-	-	0.866

Figure 3.31 to Figure 3.40 showed that the compressive stresses at centroid of the abutment are higher than stress values at centroid of mid-span for all cases; however, the obtained values in these figures are not maximum stresses within the beam. In order to determine maximum axial stresses, values of compressive stress at lowest part of the abutment and highest part of the mid-span must be obtained.

Figure 3.41 to Figure 3.43 illustrate the maximum axial compressive stresses within beams with different rock types and span values. The thickness of the beams in these figures is to a unit value, as other thicknesses show similar results. They are depicted through three separate plots to avoid making complicated figures. Data points show the compressive stresses at mid-span and abutments that are obtained from UDEC simulations; while solid lines represent results of voussoir beam method.

As these figures show, a larger span leads to higher stress concentration. Numerical models give different stress values at mid-span and abutments, while voussoir method assumes they are equal. One could compare the average of the maximum axial stress at abutment and mid-span with voussoir prediction; however, it still shows a noticeable difference. This reflects the effect of an invalid assumption of equal and linear stress distributions within the beam in the voussoir analogue. It can be seen that data points that represent stresses at mid-span are close to solid lines, but stresses at abutments are significantly greater than stresses obtained from voussoir method as well as stresses at mid-span.

The voussoir method does not accurately predict the maximum stresses within the beam. Maximum and minimum error of axial stresses at mid-span are 42.4% and 8.7%, respectively; while the average error is 18.37%. Also, maximum and minimum error of stresses at abutments are calculated as 77.7% and 37.3%, respectively, and the average error is 46.7%. Clearly errors of stresses obtained from voussoir beam are high with respect to both mid-span and abutment, but since maximum stress concentration occurs at the abutments, equations of voussoir beam method must be modified in way to accurately predict compressive stresses at the abutments. In other words, error of 46.7% must be reduced to a reasonable value so that the results of factors of safety would be reliable.

The assumption of a linear and equal stresses at both ends needs to be modified. Clearly, the maximum axial stress is concentrated at the abutments. It implies that failure due to crushing most likely happens at both ends for high span/thickness values rather than the middle of the beam.

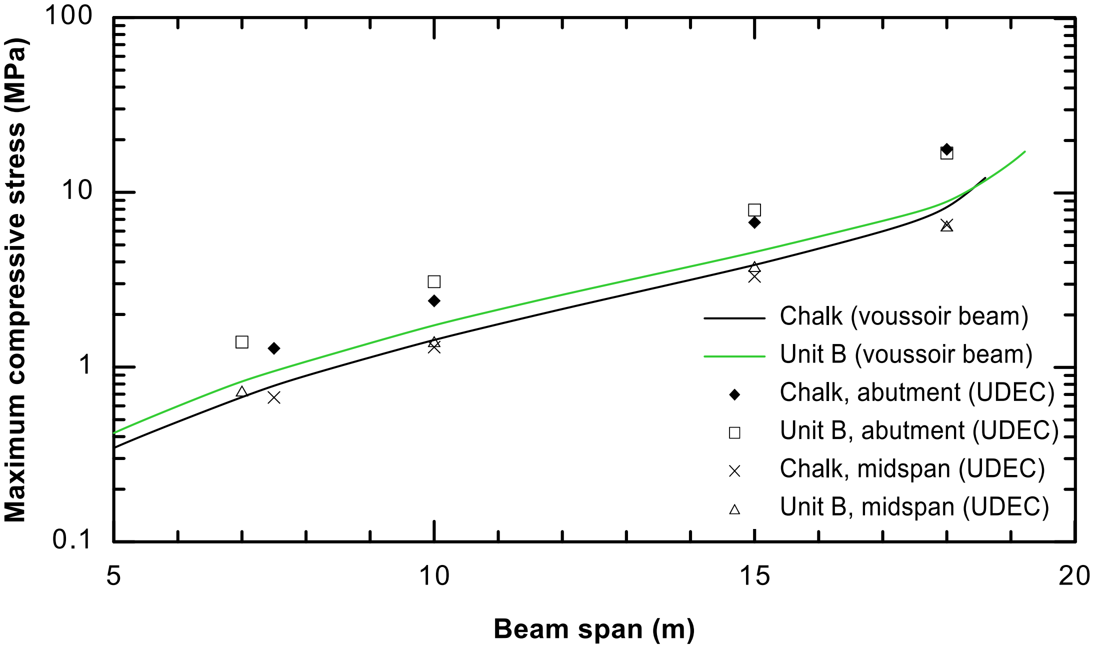

Figure 3.41 Maximum axial compressive stress for chalk and unit B rock masses

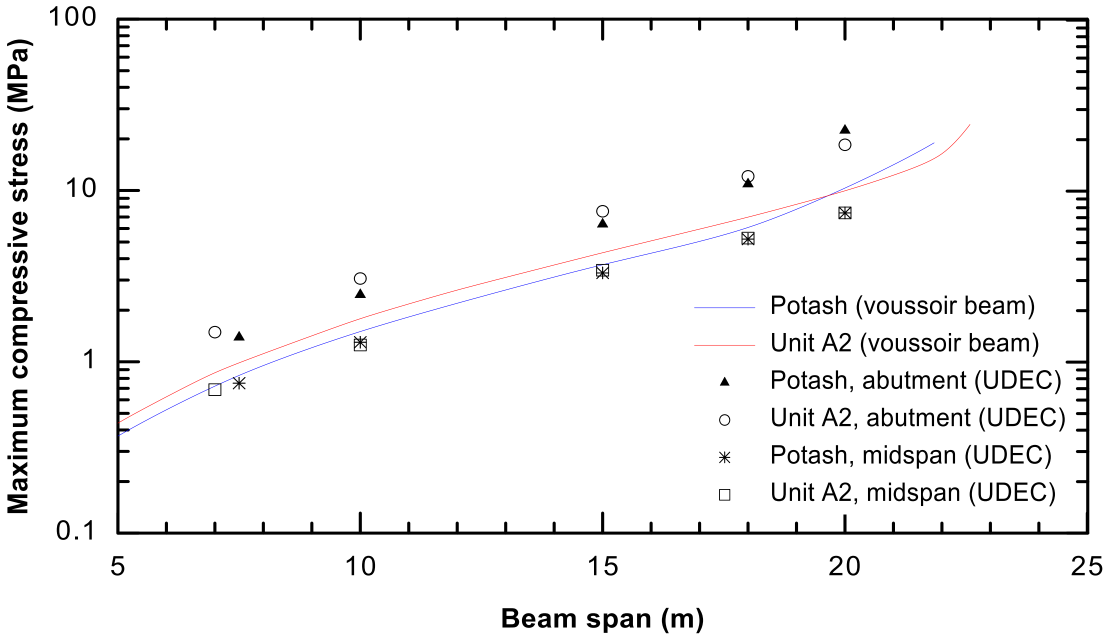

Figure 3.42 Maximum axial compressive stress for potash and unit A2 rock masses

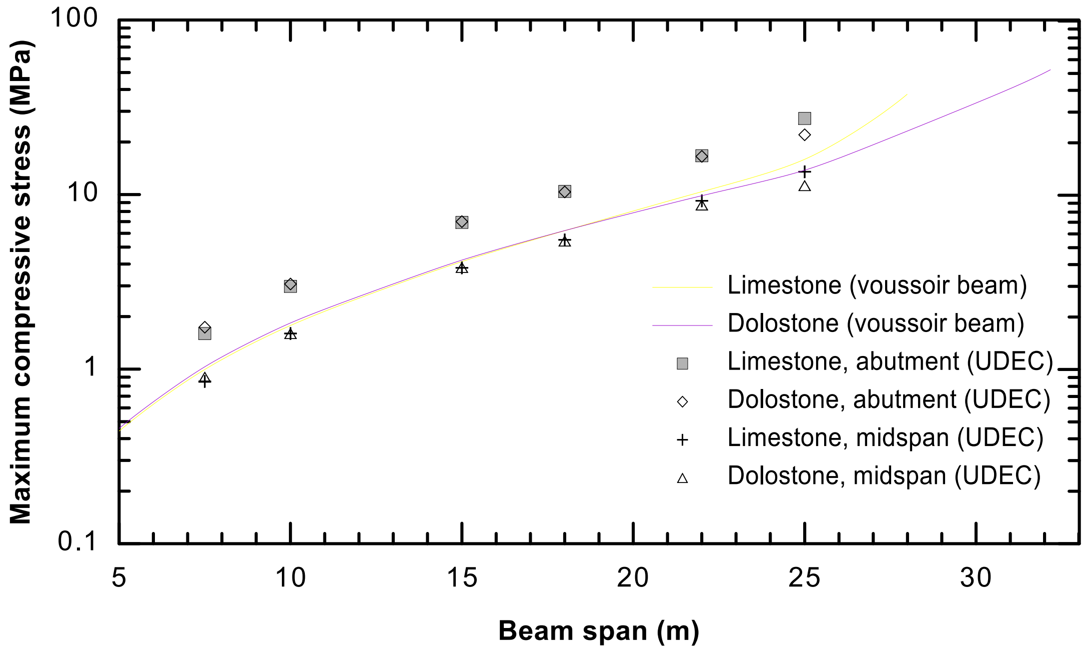

Figure 3.43 Maximum axial compressive stress for limestone and dolostone rock masses

In order to compare the stress distributions at abutment and mid-span in more details. Two of the rock types (unit B and unit A2) are selected and examined with different span values. Numerical simulations show that the normal compressive thickness (n) at mid-span is greater than that at the abutments. Figure 3.44 and Figure 3.45 display axial compressive stress distribution within the thickness of the beams at the abutments and mid-span. Different spans have been examined for each model with unit B and unit A2 rock mass properties. The minimum span in the following figures is 7 m because of the scale. The axial stress for a 5 m span is very low and it cannot be seen on the graph. It can be observed that the compressive thickness at mid-span (n_m) is approximately $\frac{3}{2}$ of that at the abutments (n_a). High stress concentration at relatively smaller compressive thickness leads to a non-linear distribution at the abutments, while it can be assumed that the stress distributions at mid-span are linear and form a triangle.

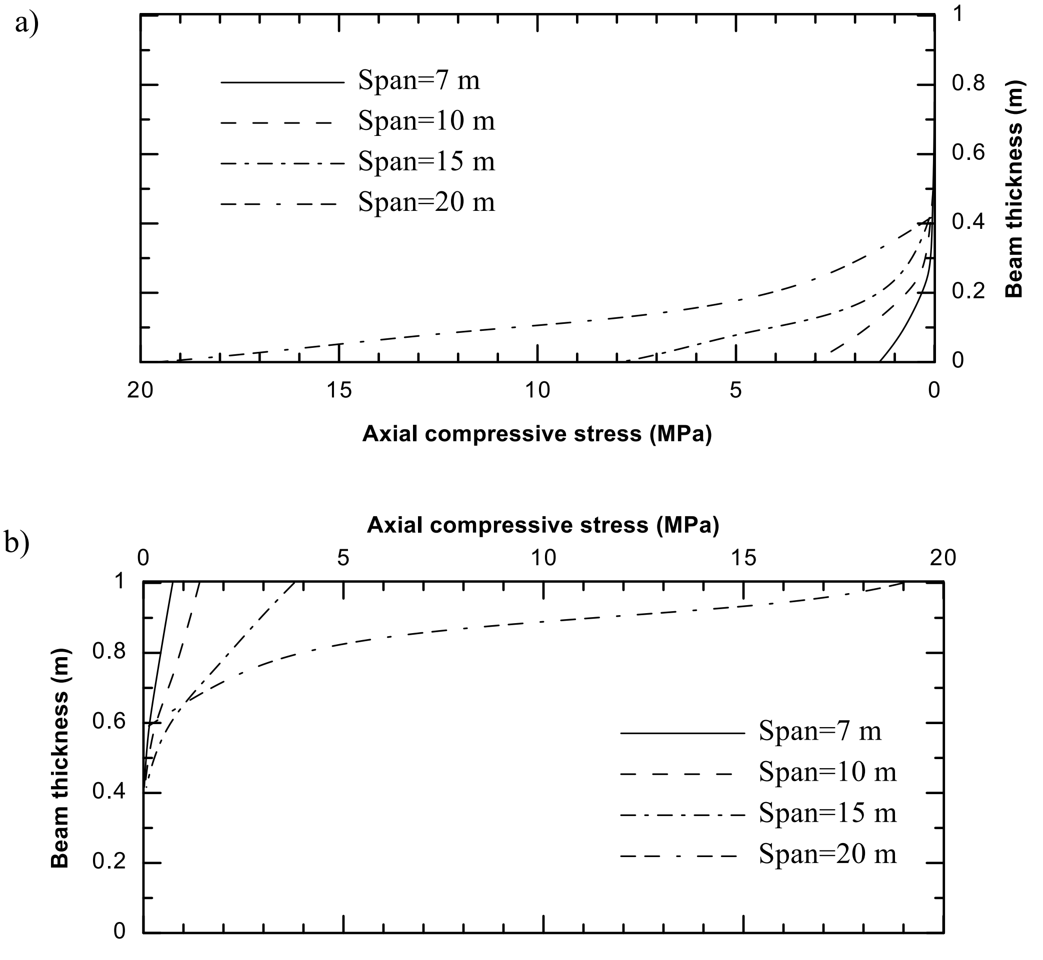

Figure 3.44 Stress distribution at abutment (a) and mid-span (b) for unit B rock mass

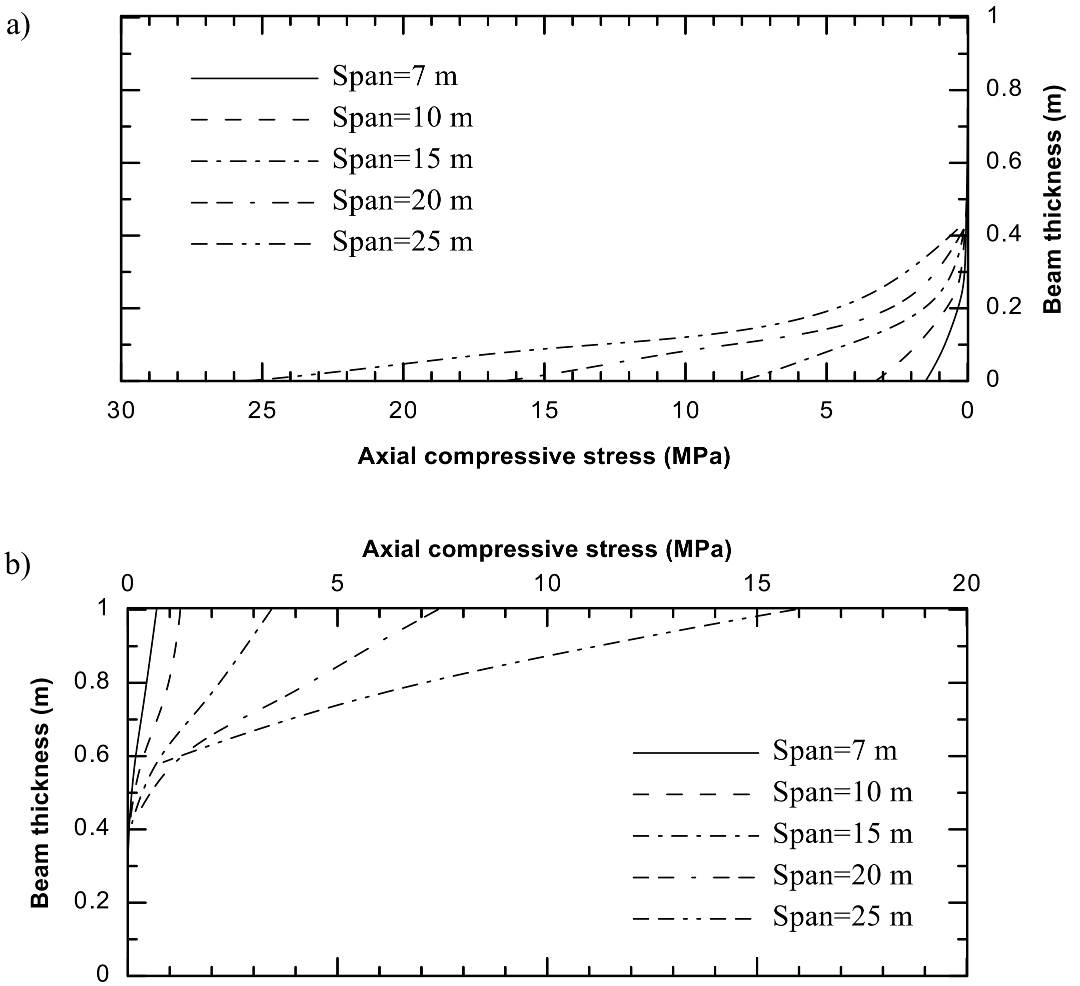

Figure 3.45 Stress distribution at abutment (a) and mid-span (b) for unit A2 rock mass

Numerical models in UDEC suggest that voussoir assumptions regarding the equal value for axial stress and normal compressive thickness at the abutments and mid-span are not accurate. This is the reason for high errors of maximum stress values. Therefore, more consistent assumptions are required to predict stress distributions within the beam. The next section of this chapter would describe the modifications to cope with this issue.

3.4 Modified voussoir beam theory

In voussoir beam method, axial stresses are assumed to be linear and form a triangular distribution at the abutment and mid-span. Figure 3.44 and Figure 3.45

demonstrate that the assumption of the linear stress distribution might be valid at mid-span, but it is not accurate at the abutments. The values of axial stress obtained from numerical modeling at the abutment are noticeably higher than voussoir solution (Figure 3.41 to Figure 3.43). Therefore, a better approximation for stress distribution at the abutment is required.

Let us assume the stress distribution at both abutments and mid-span can be replaced with a second order polynomial (Figure 3.46).

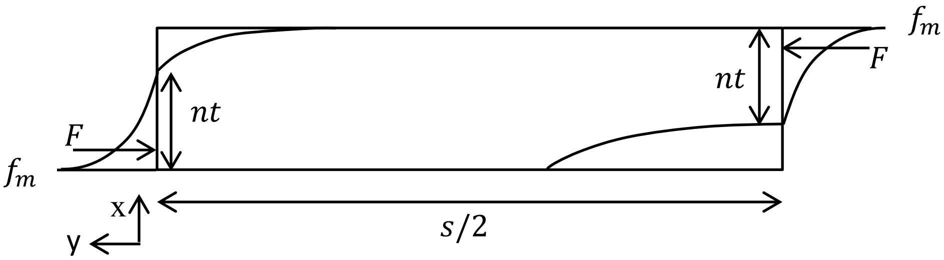

Figure 3.46 Non-linear stress distribution at both abutment and mid-span

Therefore, the parabolic stress can be expressed as

$$y = ax^2 + bx + c \tag{3.1}$$

when $x = 0$, then $y = f_m$

$$c = f_m \tag{3.2}$$

when $x = nt$, then $y = 0$

$$a(nt)^2 + b(nt) + c = 0 \tag{3.3}$$

when $x = 2nt$, then $y = f_m$

$$a(2nt)^2 + b(2nt) + c = f_m \tag{3.4}$$

Combining equations (3.3) and (3.4)

$$b = \frac{-2f_m}{nt} \tag{3.5}$$

$$a = \frac{f_m}{n^2t^2} \tag{3.6}$$

Hence the equation of stress distribution is

$$y = \frac{f_m}{n^2t^2}x^2 - \frac{2f_m}{nt}x + f_m \tag{3.7}$$

The centroid of any function can be calculated by

$$x = \frac{\int_a^b xf(x)\,dx}{\int_a^b f(x)\,dx}\ , a \leq x \leq b \tag{3.8}$$

Thus, the centroid of the stress distribution is

$$x = \frac{\int_0^{nt} x(ax^2 + bx + c)\,dx}{\int_0^{nt}(ax^2 + bx + c)\,dx} \tag{3.9}$$

Replacing constant parameters by equations (3.2), (3.5) and (3.6)

$$x = \frac{nt}{4} \tag{3.10}$$

Putting this value into equation (3.7), the axial compressive stress at the centroid, σ_c, would be calculated as

$$\sigma_c = \frac{9}{16}f_m \tag{3.11}$$

The average of a function over a domain can be calculated using

$$y_{av} = \frac{\int_a^b f(x)\,dx}{b-a} \tag{3.12}$$

Thus the average axial stress at the abutment and mid-span can be obtained by

$$F = \frac{\int_0^{nt} f(x)\,dx}{nt} \tag{3.13}$$

where $f(x)$ can be replaced by equation (3.7)

$$F = \frac{f_m}{3} \tag{3.14}$$

These calculations are based on nonlinear stress distribution at both mid-span and abutments; however, my numerical simulations showed that the linear distribution at mid-span is consistent with voussoir results. Thus, a triangular distribution at mid-span and a second order polynomial distribution at the abutment have been assumed (Figure 3.47).

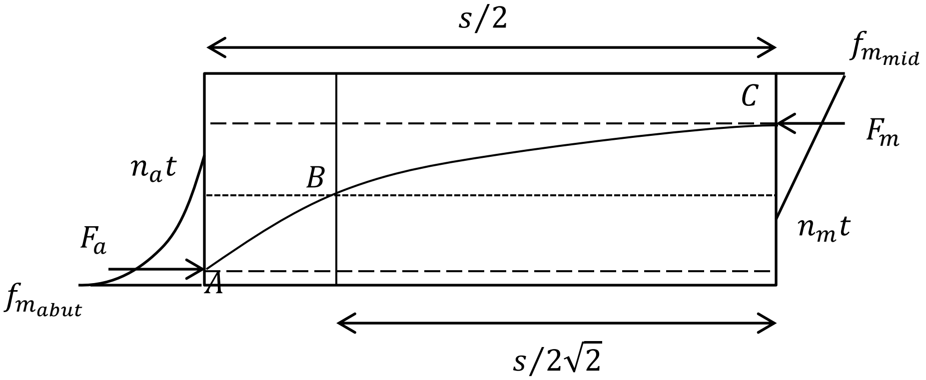

Figure 3.47 Linear and non-linear stress distribution in voussoir beam

Moreover, Figure 3.44 and Figure 3.45 show that the normal compressive thickness at midspan (n_m) is higher than that at the abutment (n_a) and the ratio is approximately $3:2$.

$$\frac{n_m}{n_a} = \frac{3}{2} \tag{3.15}$$

So the initial arm of arch would be

$$Z_0 = t - \frac{n_a t}{4} - \frac{n_m t}{3} \tag{3.16}$$

Replacing n_m with equation (3.15)

$$Z_0 = t(1 - \frac{3n_a}{4}) \tag{3.17}$$

Writing force balance in horizontal direction for half of beam gives

$$\sum F = 0 \tag{3.18}$$

$$\frac{f_{m_{abut}}}{3} n_a t = f_{min} t = \frac{f_{m_{mid}}}{2} n_m t \tag{3.19}$$

where $f_{m_{abut}}$ and $f_{m_{mid}}$ are maximum axial stress at abutment and mid-span, respectively, and f_{min} is axial stress at $\frac{s}{2\sqrt{2}}$ away from mid-span where the entire thickness of the beam is under compression.

Using equation (3.19)

$$f_{m_{abut}} = \frac{9}{4} f_{m_{mid}} \tag{3.20}$$

$$f_{min} = \frac{f_{m_{abut}}}{3} n_a \tag{3.21}$$

The moment generated by deflection, M_R, must compensate the moment due to gravitational load, M_W. Writing the moment balance at the abutment gives

$$\sum M = 0 \tag{3.22}$$

$$\frac{f_{m_{abut}}}{3} n_a t Z = \frac{\gamma t s^2}{8} \tag{3.23}$$

Thus

$$f_{m_{abut}} = \frac{3\gamma s^2}{8 n_a Z} \tag{3.24}$$

Also, the average axial stress within the arch can be calculated using a weighted average method based on the distribution of stress within the beam. Hu (2016) measured the straight distance between points A, B and C using the Pythagorean Theorem; however, the length of the arc created between these points can be considered for more accuracy. Thus, the average stress would be

$$f_{av} = \left(\frac{\overset{\frown}{AB}}{\overset{\frown}{AC}}\right) f_{AB} + \left(\frac{\overset{\frown}{BC}}{\overset{\frown}{AC}}\right) f_{BC} \tag{3.25}$$

where $\overset{\frown}{AB}$, $\overset{\frown}{AC}$ and $\overset{\frown}{BC}$ are the length of the reaction arch from point A to B, A to C and B to C, respectively. The axial stresses acting on the arch from point A to B and point B to C are punctuated as f_{AB} and f_{BC}. These values can be calculated as following

$$f_{AB} = \frac{\sigma_{c_{abut}} + f_{min}}{2} \tag{3.26}$$

$$f_{BC} = \frac{f_{min} + \sigma_{c_{mid}}}{2} \tag{3.27}$$

where $\sigma_{c_{abut}}$ and $\sigma_{c_{mid}}$ are the axial stresses at the centroid of the abutment and mid-span, respectively. Using the same procedure presented in 0, values of $\overset{\frown}{AB}$, $\overset{\frown}{BC}$ and $\overset{\frown}{AC}$ can be determined using the following equations.

$$\overset{\frown}{AB} = \frac{2Z^2(2\sqrt{2}-0.75\sqrt{0.75})}{3s\sqrt{2}} + \frac{s(\sqrt{2}-\sqrt{0.75})}{2\sqrt{2}} \tag{3.28}$$

$$\overset{\frown}{BC} = \frac{1.5Z^2\sqrt{0.75}}{3s\sqrt{2}} + \frac{s\sqrt{0.75}}{2\sqrt{2}} \tag{3.29}$$

$$\overset{\frown}{AC} = \frac{4Z^2}{3s} + \frac{s}{2} \tag{3.30}$$

Replacing equations (3.26) through (3.30) into equation (3.25) gives the value of average axial stress. By using these equations, the iterative voussoir solution would be updated with new assumptions. The maximum axial stress values at the abutment for various spans are depicted in Figure 3.48 to Figure 3.50. As these figures show, stress values obtained from numerical models are consistent with the results of the modified voussoir solution. The maximum and minimum errors are 10.7% and 0.23%, respectively, and the average error is 2.6%. The assumption of linear and identical stress distribution and equal normal compressive thickness at both abutments and mid-span caused an average error of 46.7% for axial stress at abutment by voussoir method; while new results give an average error of 2.6%. Therefore, other results of voussoir method must be obtained using the modified equations to be trustable.

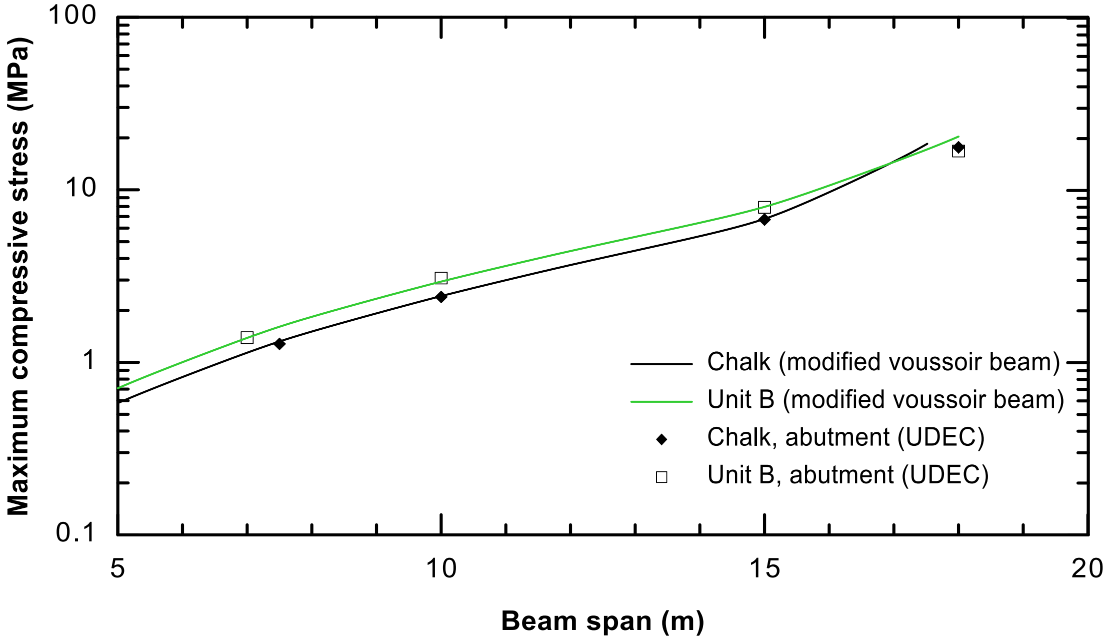

Figure 3.48 Modified maximum axial compressive stress for chalk and unit B rock masses

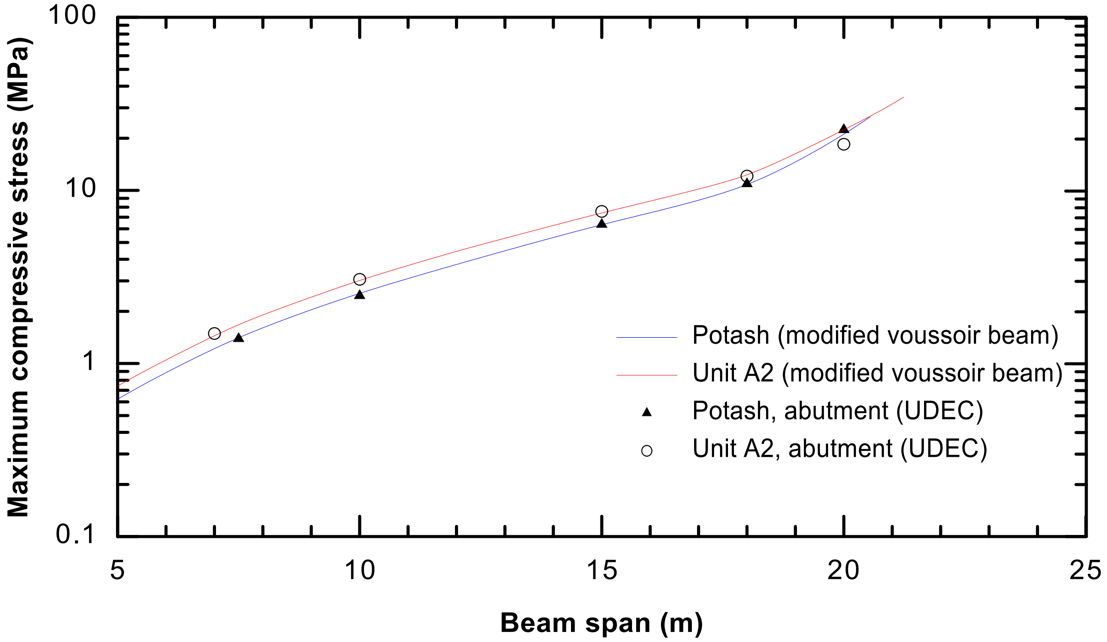

Figure 3.49 Modified maximum axial compressive stress for potash and unit A2 rock masses

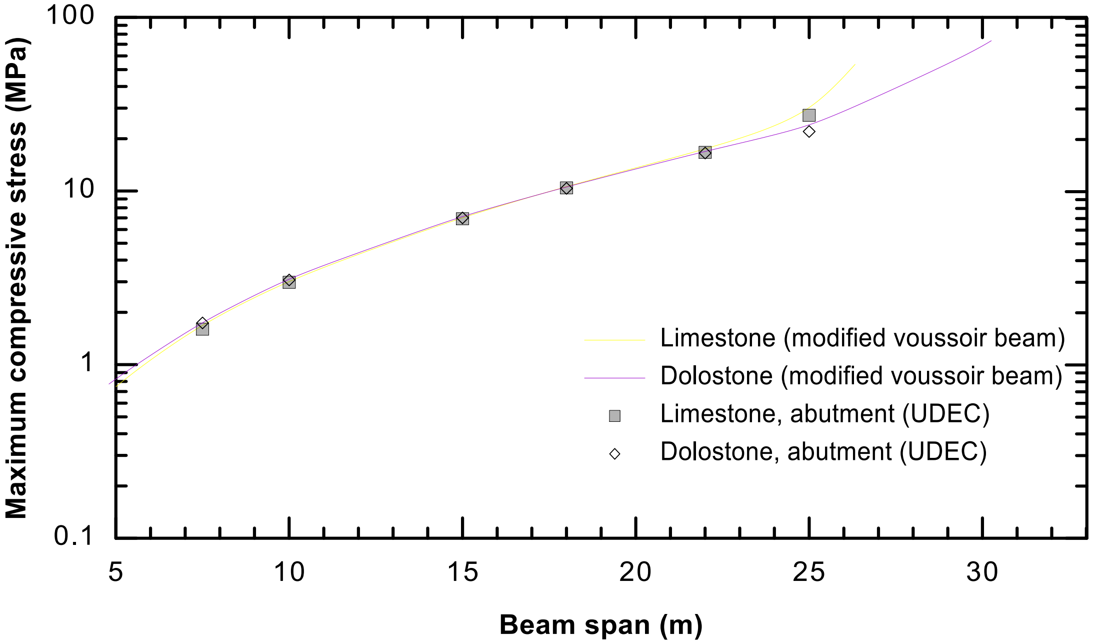

Figure 3.50 Modified maximum axial compressive stress for limestone and dolostone rock masses

3.4.1 Mechanical response of the roof rock

In order to investigate mechanical response of the roof rocks, different types of rock with various span values and unit thicknesses have been considered. This assessment leads to the maximum allowable span for a cavern roof. Using the information presented in section 1.4.2.2, rock and joint properties of the beam models were determined and summarized in Table 3.3.

Figure 3.51 and Figure 3.52 show the maximum vertical displacement for different span values. They are depicted in two separate plots to keep them clear and understandable. The solid lines are the results of voussoir analysis, data points are UDEC simulations and dashed lines are results of modified voussoir beam. A roof layer with greater span/thickness ratio undergoes higher displacement. A weak rock mass (such as chalk) shows highest displacement at a constant size, while a strong rock mass (such as dolostone) shows least displacement.

Stability of the beam is controlled by the maximum mid-span displacement. Diederichs and Kaiser (1998) considered a displacement equivalent to approximately $0.25 \times t$ would lead to a buckling limit of 100% in which failure occurs; however, present analysis shows a displacement of $0.33 \times t$ corresponds to 100% of buckling factor. This can be clearly seen in Figure 3.51 and Figure 3.52. For all types of rock masses, roof beams deform until magnitude of displacement reaches one third of the beam thickness and then no data can be found as beam fails (Table 3.12). This is valid for both UDEC and voussoir results. If displacement is less than this limit but greater than 10% of the thickness ($0.1 \times t$), beam is in yield zone. This would lead to a buckling limit of 40%. Yield zone starts from the point that displacement would rapidly increases until beams would collapse. It must be noted that when the voussoir solution does not give any result, it means the beam has failed under snap-through failure. Also, roof beam models in UDEC immediately collapse beyond the failure limit ($\text{Buckling Limit} = 100\%$) predicted by analytical solution. It means that no data point could be added over the failure line in Figure 3.51 and Figure 3.52.

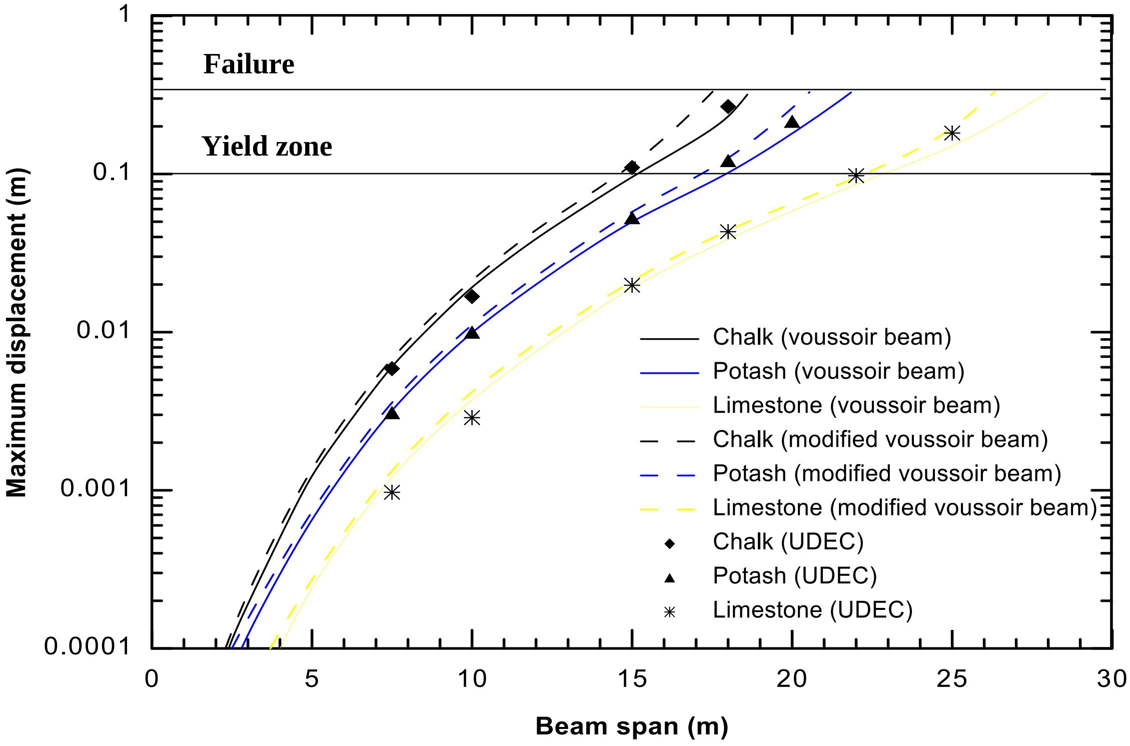

Figure 3.51 Maximum vertical displacement for chalk, potash and limestone

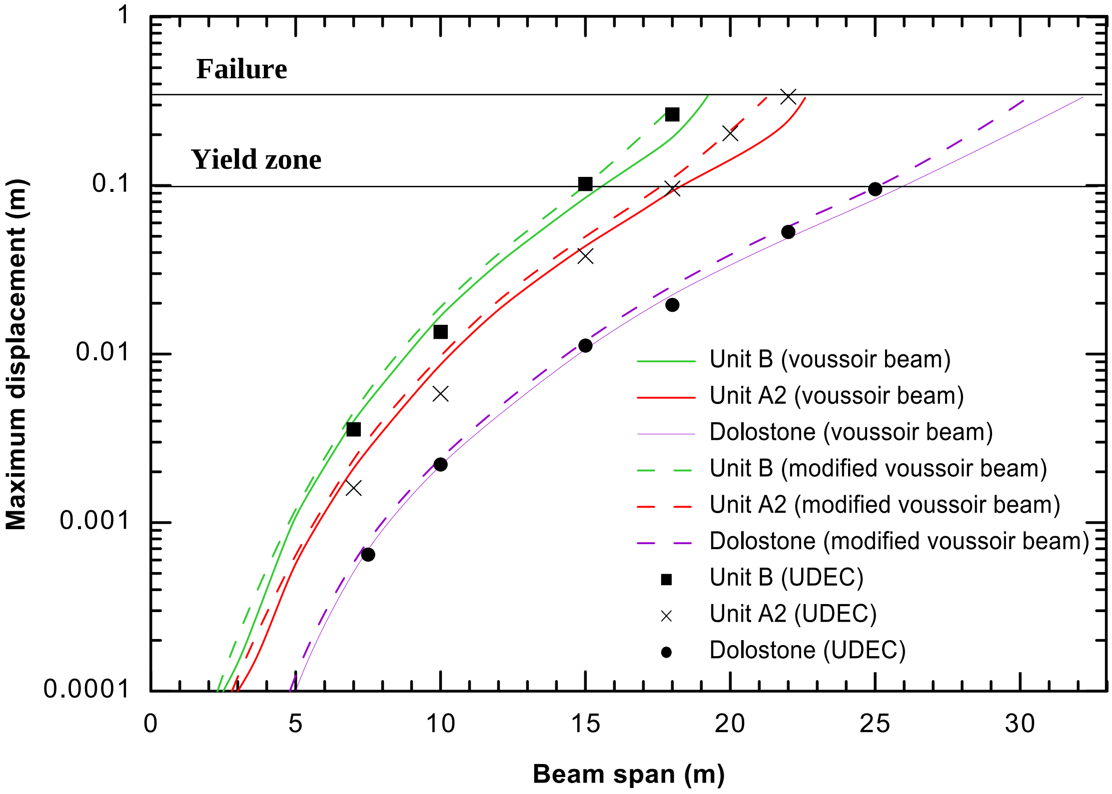

Figure 3.52 Maximum vertical displacement for unit B and unit A2 and dolostone

As Figure 3.52 depicts, maximum allowable span for unit B cap rock is $18.07\ m$ and for unit A2 cap rock is $21.24\ m$. These values limit the maximum size of the roof layer for caverns in salt beds of western Ontario. As Figure 3.51 and Figure 3.52 show, both initial (solid lines) and modified (dashed lines) voussoir beam methods give fairly accurate results. In fact, voussoir beam predicts the displacement of the beam accurately for high spans, but it slightly overestimates the deformation for small spans. Table 3.11 summarizes the minimum, maximum and average error of the results obtained from initial and modified voussoir beam method with respect to UDEC simulations. Maximum error usually happens for relatively low span/thickness ratios for both versions of voussoir beam. In contrast, modified voussoir beam gives the minimum error for high span/thickness ratios. In fact, values of minimum error for modified voussoir beam in Table 3.11 represent models with highest span values for all types of material. Displacement is very limited (in order of millimeters) for smaller spans. Therefore, a high value of error does not concern engineers in the design process of the cavern. Since high roof span is usually desired, error of predicted results must be reasonable for high span models, which Figure 3.51 and Figure 3.52 and Table 3.11 demonstrate accuracy of the method.

Table 3.11 Errors of initial and modified voussoir beam for different types of rock mass

Rock mass	Error of voussoir beam (%)			Error of modified voussoir beam (%)		
	Minimum	Maximum	Average	Minimum	Maximum	Average
Chalk	2.8	14.3	10.8	4.4	26.3	15.3
Unit B	5.6	19.4	11.1	2.5	24.2	15.6
Potash	2.9	16.3	6.5	3.8	11	9.7
Unit A2	4	32.8	14.7	2.8	32.1	17.3
Limestone	3.8	38.1	16.2	1.5	45.1	19.4
Dolostone	1.3	14.7	8.1	2.4	29.4	12.4

The factor of safety for crushing is depicted in Figure 3.53 and Figure 3.54. Crushing at the abutments is critical for beams with high span/thickness values as compressive stress concentration increases. As these figures show, results of modified voussoir beam are consistent with simulations. The minimum, maximum and average error of the initial voussoir beam are 59.6%, 114.3% and 69.7%, respectively; whereas modified results lead to minimum, maximum and average error of 0.23%, 8.5% and 2%, respectively.

Failure occurs when axial stress exceeds the strength of the material. Hence, a value less than one for the factor of safety presents crushing failure; however, damage starts even when stress is less than uniaxial compressive strength (UCS) depending on the rock mass properties. Crack initiation threshold for unit B and unit A2 layers are 32% and 45% of UCS, where values of UCS are $8\ MPa$ and $60\ MPa$, respectively (Table 1.5). Thus, the yield limit for factor of safety against crushing failure is 3.12 for unit B layer and 2.22 for unit A2 layer. Since the rock mass of unit A2 is very much stronger than unit B, there is no risk of crushing failure for this layer while unit B is strongly under compression when span is greater than $15\ m$.

For low span/thickness values sliding failure is most likely to happen (Figure 3.55 to Figure 3.57). Shear failure at the abutments occurs when the shear force is high enough to mobilize the frictional resistance. Therefore, a value less than one for factor of safety leads to slip at the abutments. It has been noted that shear sliding happens for models with $s = 5\ m$ in UDEC for materials with low friction angle (unit B, unit A2 and limestone).

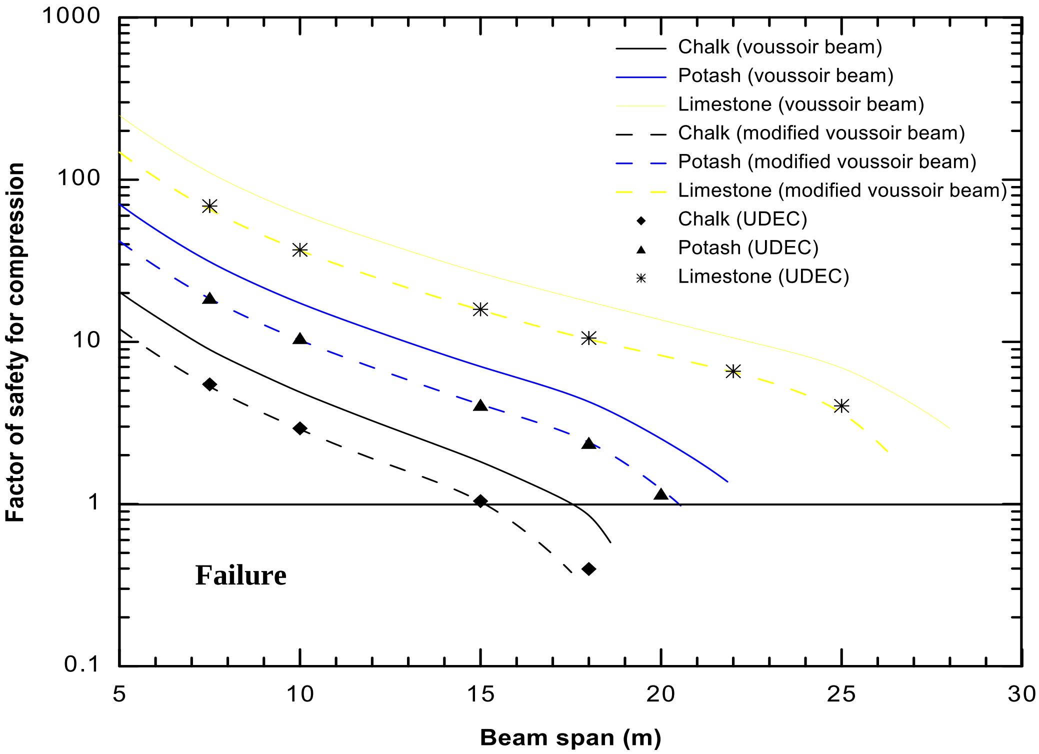

Figure 3.53 Factor of safety against compression failure for chalk, potash and limestone

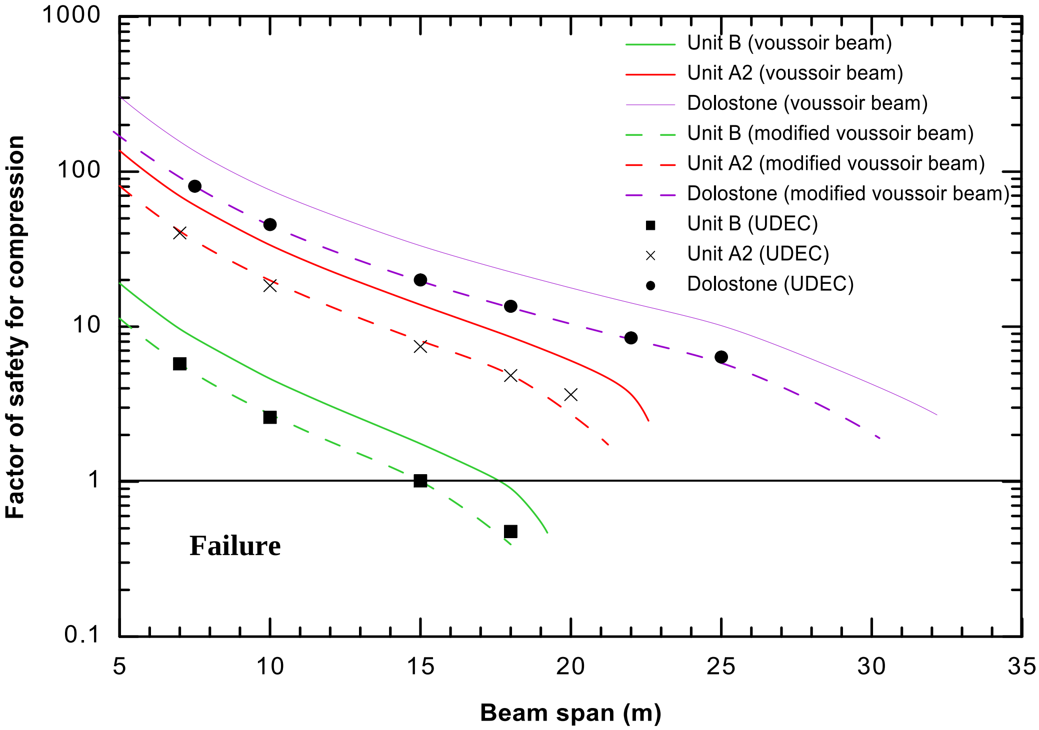

Figure 3.54 Factor of safety against compression failure for unit B, unit A2 and dolostone

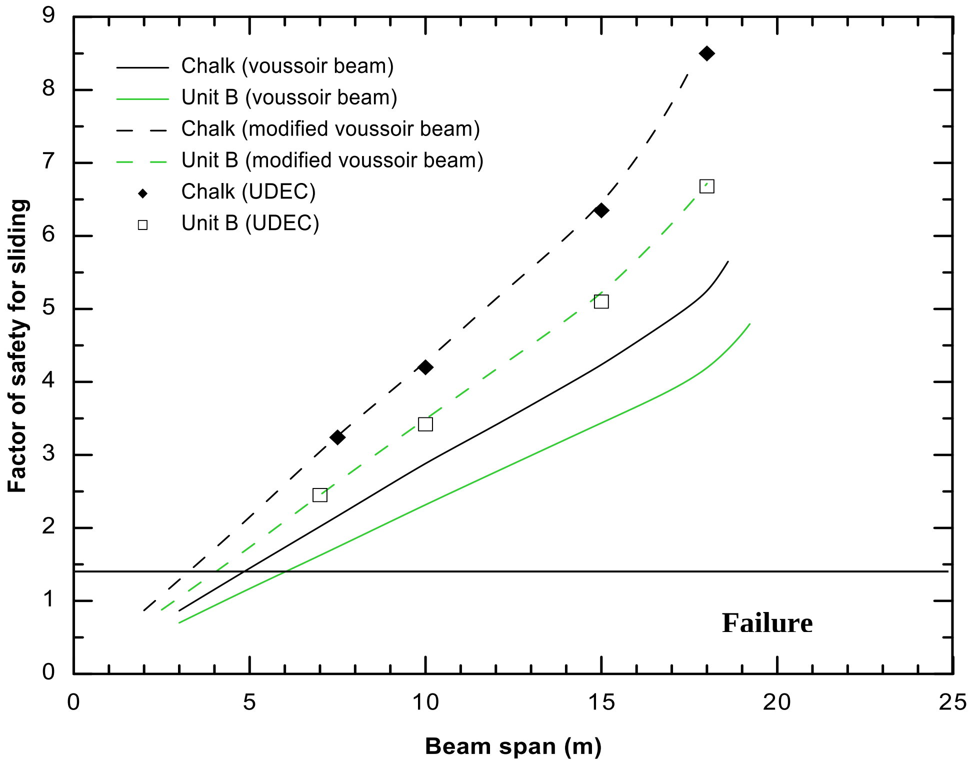

Figure 3.55 Factor of safety against sliding failure for chalk and unit B

The analyzed beams give a value of 1.9 for sliding factor based on results of modified method and 1.16 based on initial voussoir method. Shear failure causes serious stability issues and casing impairment, so the limit for this factor of safety must be chosen in a way to ensure stability of the cavern roof. Since results of modified method are consistent with UDEC simulations, a limit of 1.9 is considered for sliding factor stability limit. The minimum, maximum and average error of the results are 31.4%, 38.2% and 33.6% for voussoir beam method and 0.5%, 2.1% and 1.3% for modified version, respectively. Results of the modified voussoir beam analysis are summarized in Table 3.12.

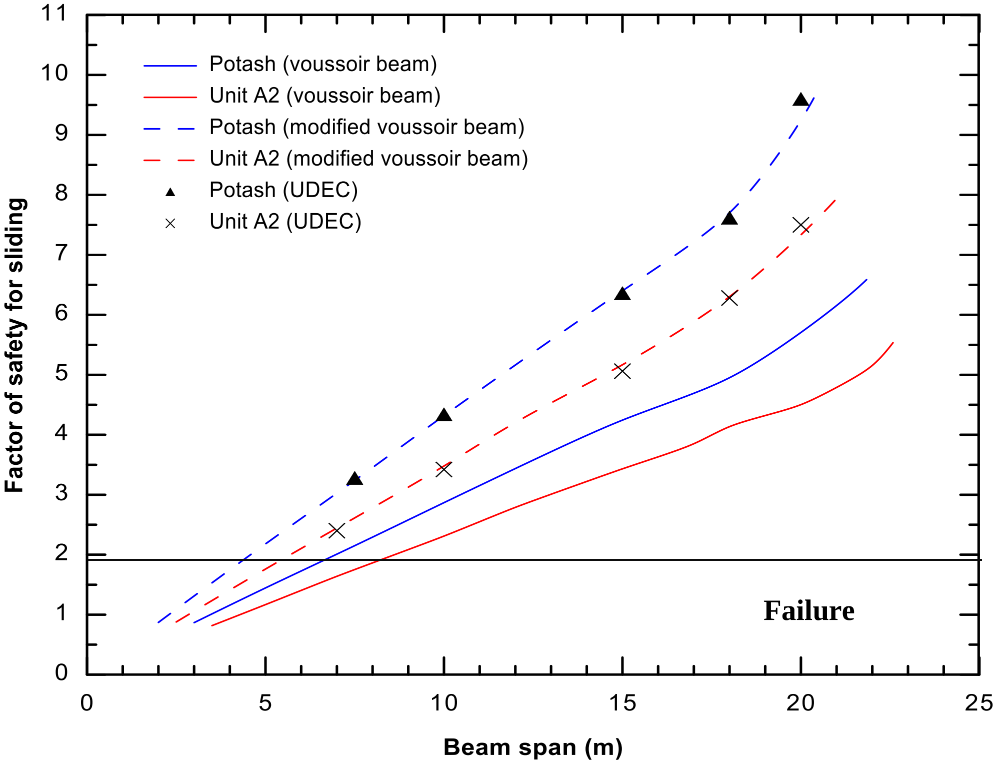

Figure 3.56 Factor of safety against sliding failure for potash and unit A2

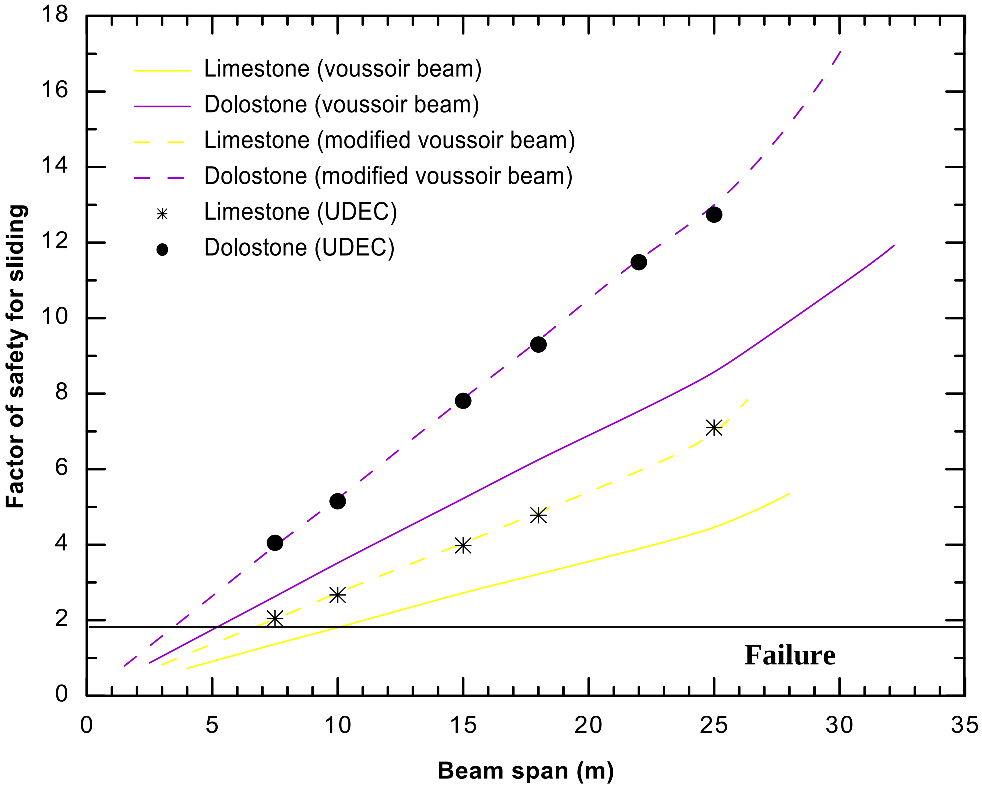

Figure 3.57 Factor of safety against sliding failure for limestone and dolostone

Table 3.12 Summary of the modified voussoir beam analysis (the first, second and third number for each beam show the displacement, factor of safety for crushing and sliding failure, respectively)

Span	Chalk	Unit B	Potash	Unit A2	Limestone	Dolostone	Note
5	0.0014	0.0012	0.0007	0.0006	0.0003	0.0001	Sliding failure at the abutments for unit B, unit A2 and limestone rock masses
	12.05	11.30	41.82	81.04	147.58	181.22	
	2.15	<1.9	2.18	<1.9	<1.9	2.64	
7.5	0.0068	0.0059	0.0036	0.0031	0.0013	0.0008	-
	5.30	4.97	18.48	35.84	65.45	80.42	
	3.26	2.63	3.24	2.61	2.03	3.96	
10	0.0212	0.0189	0.0111	0.0097	0.0042	0.0024	-
	2.89	2.72	10.24	19.89	36.61	45.09	
	4.28	3.49	4.32	3.48	2.73	5.22	
12	0.0442	0.0392	0.0234	0.0207	0.0085	0.005	-
	1.91	1.81	6.93	13.50	25.2	31.15	
	5.14	4.17	5.15	4.20	3.25	6.3	
15	0.1148	0.1002	0.0576	0.0498	0.021	0.012	-
	1.03	1.01	4.11	8.10	15.71	19.65	
	6.46	5.22	6.40	5.17	4.04	7.87	
18	>0.33	0.2914	0.1265	0.1106	0.0439	0.0253	Crushing and snap-through failure for chalk; crushing failure for unit B rock mass
	<1	<1	2.40	4.88	10.38	13.27	
	-	6.72	7.70	6.30	4.85	9.41	
20	-	>0.33	0.2307	0.1863	0.0684	0.0385	Snap-through failure for unit B rock mass
		<1	1.45	3.21	7.95	10.45	
		-	8.94	7.12	5.41	10.4	
22	-	-	>0.33	>0.33	0.1013	0.057	Crushing and snap-through failure for potash; snap-through failure for unit A2
			<1	-	6.05	8.29	
			-	-	5.9	11.54	
25	-	-	-	-	0.196	0.0973	-
					3.64	5.82	
					6.98	12.99	
27	-	-	-	-	>0.33	0.1393	Snap-through failure for limestone
					-	4.48	
					-	14.16	
30	-	-	-	-	-	0.2761	-
						2.41	
						16.8	
32	-	-	-	-	-	>0.33	Snap-through failure for dolostone
						-	
						-	

3.5 Application of voussoir beam to creep

Classical voussoir beam theory assumes an elastic behavior for beam in which the stress/strain relationship follows Hook's law. There are two ways to investigate inelastic behavior of the beam using the voussoir method. Generally, one could discretize the stress/strain curve into small intervals when it passes the yield point. Each interval in this condition is assumed to be linear. Thus, a specific Young's modulus can be assumed for each interval. In fact, the inelastic behavior affects Young's modulus and it would be updated during the solution for all steps using the same Hook's law.

The second way is to use a non-elastic equation to take the effect of inelastic stress/strain relationship into account. For this purpose a typical creep model for rock salt has been considered. Since the only goal of this section is to examine the capability of voussoir method to incorporate the effect of creep, a simple model with typical values is sufficient. In an engineering time and stress, a steady-state creep law properly models the creep behavior of rock salt.

$$\dot{\varepsilon} = A \exp(\frac{-Q}{RT}).(\frac{\sigma_1 - \sigma_3}{\sigma_0})^m \qquad \textbf{(3.31)}$$

where m is the stress component, Q is the apparent activation energy of the rate-limiting flow mechanism, R is the universal gas constant and T is the absolute temperature. Constant parameters of A , σ_0 and m depend on salt properties. Value of m and σ_0 represent the effect of stress and a constant scaling parameter, respectively, while A is the effect of fabric damage and depends on grain size, defect density, porosity (brine content), crystal anisotropy, etc. (Dusseault and Fordham, 1994)

Temperature is assumed to be constant and the effect of stress is only taken into account. Therefore, a simplified version of the steady-state creep law has been used here

$$\dot{\varepsilon} = A\,\overline{\sigma}^{m} \tag{3.32}$$

where $\overline{\sigma}$ is deviatoric stress. The values of m and A are 3 and $1.67 \times 10^{-31}\ \ Pa^{-3}Sec^{-1}$, respectively.

The above equation determines the strain caused by creep of salt with respect to time. Summation of the displacement due to elastic and creep response is considered as the total displacement of the beam. The response of a $10\,m$ roof beam has been examined within a 10 year period. Creep response of three beams with properties of unit B, potash and unit A2 are investigated.

Since there is no creep at time equal to zero, results of the new solution must be exactly same as the elastic voussoir method. Displacement obtained from (2.20 can be added to displacement due to (3.32 to take the effect of creep into account. As time increases, higher vertical displacement and axial stress are expected.

The results demonstrate that the vertical displacement and axial stresses increase with time (Table 3.13 and Table 3.14). This is valid for both modified voussoir beam and numerical simulations. It must be noted that displacement difference after 10 years is in order of millimeters. After 10 years, the maximum difference in deformation and axial stress are $0.844\,mm$ and $2.91\,KPa$ for unit B, $0.85\,mm$ and $2.99\,KPa$ for potash and $0.864\,mm$ and $3.06\,KPa$ for unit A2, respectively. Hence, creep process does not affect stability of roof beams in a noticeable way and can be ignored. It also must be noted that error of the obtained results in each time are almost equal for each type of material, as the slope of change in displacement and stress are constant (steady-state creep).

Table 3.13 Displacement of roof beams under creep

Time	Unit B		Potash		Unit A2	
	Modified voussoir beam	UDEC	Modified voussoir beam	UDEC	Modified voussoir beam	UDEC
0.0	0.01898	0.01354	0.011106	0.01	0.009715	0.005816
1.3	0.01909	0.01364	0.011213	0.010107	0.009823	0.005924
2.5	0.01919	0.01375	0.01132	0.010214	0.009931	0.006032
3.8	0.01930	0.01385	0.011427	0.010320	0.010039	0.00614
5.1	0.01940	0.01396	0.011533	0.010427	0.010147	0.006248
6.3	0.01951	0.01406	0.01164	0.010534	0.010255	0.006356
7.6	0.01962	0.01417	0.011747	0.010641	0.010363	0.006464
8.9	0.01972	0.01427	0.011854	0.010748	0.010471	0.006572
10.1	0.01983	0.01438	0.011961	0.010854	0.010579	0.00668

Table 3.14 Maximum axial stress within roof beams under creep

Time	Unit B		Potash		Unit A2	
	Modified voussoir beam	UDEC	Modified voussoir beam	UDEC	Modified voussoir beam	UDEC
0.0	2.93702	3.08	2.539748	2.4632	3.016752	3.26127
1.3	2.93739	3.080364	2.540121	2.463573	3.017133	3.261652
2.5	2.93775	3.080728	2.540494	2.463946	3.017515	3.262035
3.8	2.93811	3.081092	2.540867	2.46432	3.017897	3.262417
5.1	2.93848	3.081456	2.541241	2.464693	3.018279	3.2628
6.3	2.93884	3.081821	2.541614	2.465066	3.018662	3.263182
7.6	2.93921	3.082185	2.541987	2.465439	3.019044	3.263564
8.9	2.93957	3.082549	2.54236	2.465813	3.019427	3.263947
10.1	2.93994	3.082913	2.542734	2.466186	3.019811	3.264329

In addition, there seems to be a conflict between creep mechanism and factors of safety. By definition, creep is the tendency of the material to deform under a constant load. If stresses are constant, then creep deformation would not affect factors of safety. For example, the factor of safety against crushing depends on uniaxial compressive strength, UCS, and the maximum axial stress, f_m, which both remain constant. In other words, factors of crushing and sliding do not depend on vertical displacement and they must be constant with time; however, since displacement increases at each time step, axial stress would be updated in each iteration and change the factors of safety. This does not conform to the concept of creep behavior. Although factors of safety cannot be defined in this condition, the results of vertical displacement can still be used.

3.6 Application of modified voussoir beam to caverns

The immediate roof layer on top of an underground excavation tends to separate from the upper layers and deform under its own weight; however, the effect of the formation pressure (P_f) exerted by a column of water must be taken into account. The cavern is not completely empty. Hence, there is always a back pressure (P_i) applied on the roof layer depending on the cavern internal pressure. A typical voussoir roof layer on top of the cavern is depicted in Figure 3.58. It shows a beam deformed under gravitational load and surcharge and internal pressures. The scale of the roof and cavern are not necessarily consistent. It is only used to show the physics of the problem.

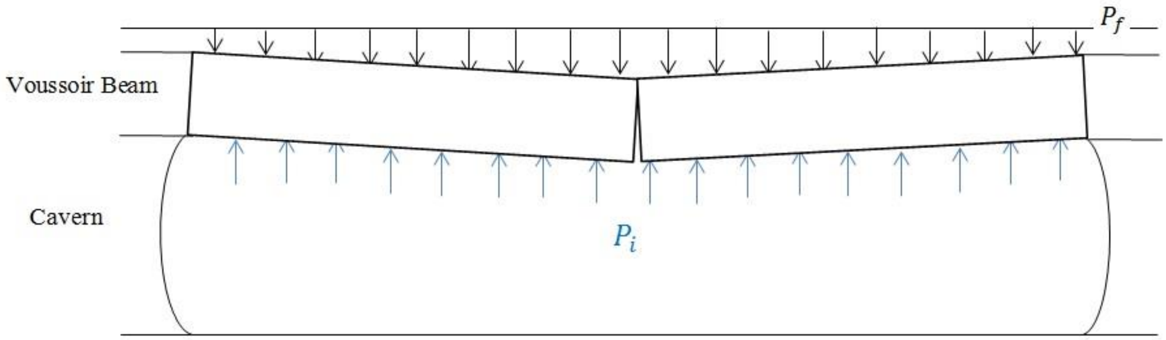

Figure 3.58 Surcharge and back pressure on a typical voussoir beam

The effect of surcharge load depends on the nature of the air and formation fluid interaction (Figure 3.58). If the pressure applied on top of the cavern does not drop as quickly as cavern internal pressure, it can negatively affect the cavern's stability. In other words, the difference between formation pressure and back pressure ($P_f - P_i = \Delta P$) strongly affects the displacement of the roof layer. Figure 3.59 presents a typical pressure drop over an ascribed time period due to air withdrawal. When rate of depletion is high enough and pressure difference exceeds the limit, the roof beam would go under compression or tension depending if ΔP is positive or negative. Load bearing capacity in this condition is controlled by rock mass properties.

The effect of pressure can be added to the solution by defining an effective unit weight.

$$\gamma_{eff} = \gamma + \frac{P_f - P_i}{T} \tag{3.33}$$

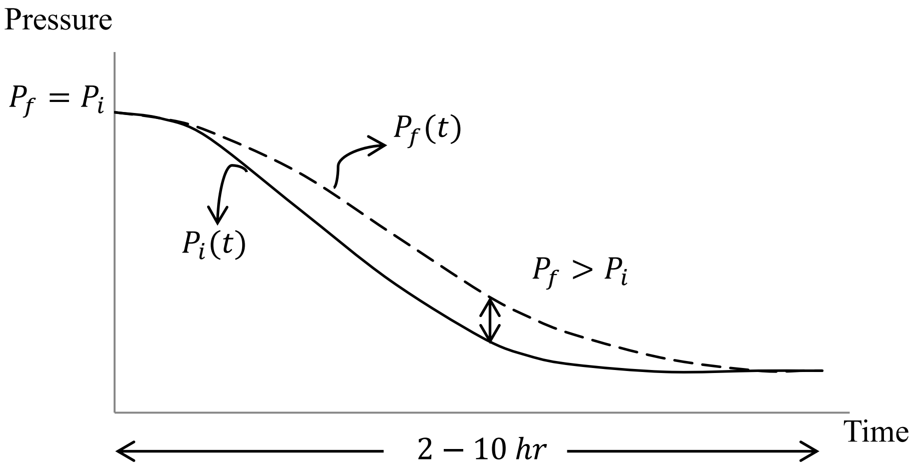

Figure 3.59 Pressure difference during air withdrawal

To understand the response of the beam to each type of pressure, they have been examined separately. A back pressure exerted upwards tends to generate a negative axial stress within the beam, unless it is less than the value of gravitational load multiplied by thickness. Behavior of the beam is similar to a lighter beam with the same properties.

$$\frac{P_i}{T} < \gamma \tag{3.34}$$

In this condition, the presence of support pressure would decrease the maximum axial stress (σ_m), decrease the displacement (δ) and factor of safety for buckling (FS_b). It increases the factor of safety for compression (FS_c) and decreases the factor of safety for sliding (FS_s), while the normal compressive thickness (n) is constant and equal to 0.75. It clearly reduces the risk of failure due to compression or buckling and allows us to have a higher span/thickness ratio. Although it decreases the factor of safety for sliding (FS_s), its value is always greater than one. Thus it would noticeably boost the stability of the roof layer.

When the upward load is greater than the value of gravitational load multiplied by thickness, the compression zone at the abutments and mid-span decreases (to $n = 0.01$) such that the entire beam becomes a large tensile zone.

$$\frac{P_i}{T} > \gamma \tag{3.35}$$

The maximum axial stress is no longer compressive. A negative value for maximum axial stress (σ_m) and factor of safety for compression (FS_c) would be obtained, while there would be no displacement ($\delta = 0$). Higher internal pressure increases the tensile stress. The span of the beam does not affect its response. Only a higher thickness mitigates the impact of back pressure. The beam is safe against snap-through and sliding. Crushing failure is not defined in this condition as tensile stresses are dominant. The tensile strength of the rock mass is negligible due to different joint sets cutting through the rock laminations. Therefore, tensile joints and cracks are expected to be extended.

When surcharge pressure (P_f) is applied on top of the roof layer, it behaves similar to a same beam with higher unit weight. As the overload increases, higher axial stress (σ_m), lower compressive zone (n) and more displacement (δ) are expected. Also, it would increase the factor of safety for buckling (FS_b) and sliding (FS_s) and decrease the factor of safety for compression (FS_c).

Load bearing capacity of the voussoir beam, in this condition, is highly dependent on the span to thickness ratio ($^S/_t$) and Young's modulus (E). When P_f is very high, the average stress within the beam increases, which leads to a higher ΔL in equation (2.20). Consequently, value of Z_{chk} in equation 5 of Figure 2.10 becomes negative. Thus, no stable value for n can be found in the iterative solution, which means failure due to snap-through has occurred. A stronger beam with higher Young's modulus (E) reduces the risk of failure by giving a lower ΔL.

If the value of overload would be fixed and span/thickness ratio increase, a similar response as mentioned above is expected. A beam with a higher span can withstand a higher overload. In most cases, failure due to compression is most likely to occur unless span/thickness ratio is relatively low, which in that case sliding failure can be an issue.

3.6.1 Maximum and minimum internal pressure

The suitable salt beds for CAES in south-western Ontario are located in Sarnia and Goderich. Only two units from the Salina Group of salt beds have enough thickness for creating a cavern. They are unit B and unit A2. These two units in Sarnia and Goderich provide four potential salt beds for CAES caverns. Depending on the depth of these units in each site, the maximum and minimum allowable pressure inside the cavern is different. As a rule of thumb, the maximum allowable pressure is 75% of the in-situ stress on top of the cavern. The vertical stress (σ_v) on the cavern roof is lower than the cavern floor. Hence, the upper limit of pressure is selected based on the vertical stress on top of the cavern to avoid fracturing. The minimum internal pressure must be greater than 25% of the in-situ stress around the cavern floor. Since pressure difference on cavern floor is greater than the roof, the creep of rock salt is stronger on the floor. Thus, the minimum internal pressure depends on the stress around the bottom of the cavern.

Table 3.15 is the summary of the allowable internal pressure for caverns. The vertical stresses depend on the depth of the salt beds and bulk density of the upper layers.

Also, the gradient of the hydrostatic pressure is assumed to be $10\ \frac{MPa}{Km}$. Therefore, the difference between formation and cavern pressures ($\Delta P = P_f - P_i$) around the roof layer can be calculated.

Table 3.15 Vertical stress and inside pressures of the caverns in Sarnia and Goderich

Site	Salt unit	Depth (top-bottom) h/m	Vertical stress (top-bottom) σ_v/MPa	Cavern pressure (Min.-Max.) P_i/MPa	Hydrostatic pressure P_f/MPa	Pressure difference $P_f - P_i/MPa$
Sarnia	B	$610 - 700$	$15.56 - 18.03$	$4.5 - 11.67$	6.1	$(-5.57) - 1.6$
	A2	$750 - 790$	$19.3 - 20.4$	$5.1 - 14.47$	7.5	$(-6.97) - 2.4$
Goderich	B	$390 - 460$	$9.95 - 11.87$	$2.97 - 7.46$	3.9	$(-3.56) - 0.93$
	A2	$510 - 535$	$13.18 - 13.85$	$3.46 - 9.89$	5.1	$(-4.79) - 1.64$

This table shows the maximum and minimum pressure difference around the cavern roof. The possibility of fluid and air transmission, which depends on the rock properties such as relative permeability and capillary pressure, is not taken into consideration. In practice, the capacity of the available surface facilities, such as compressors and turbines, also limit the cavern pressure.

In order to investigate the ability of the roof layer to tolerate overload, different voussoir beams with spans of $7, 9, 11$ and $13\ m$ have been examined. Only a positive pressure difference ($P_f > P_i$) is considered, as the risk of failure due to snap-through and compression is examined. Figure 3.60 illustrates the maximum vertical displacement for unit

B and A2 rock masses. A cavern in unit B salt bed can have a roof span of 7 m, approximately. Any wider roof cannot tolerate high pressure difference. Since unit A2 cap rock is relatively strong, a wider span, approximately 8 m, is stable under high pressure difference.

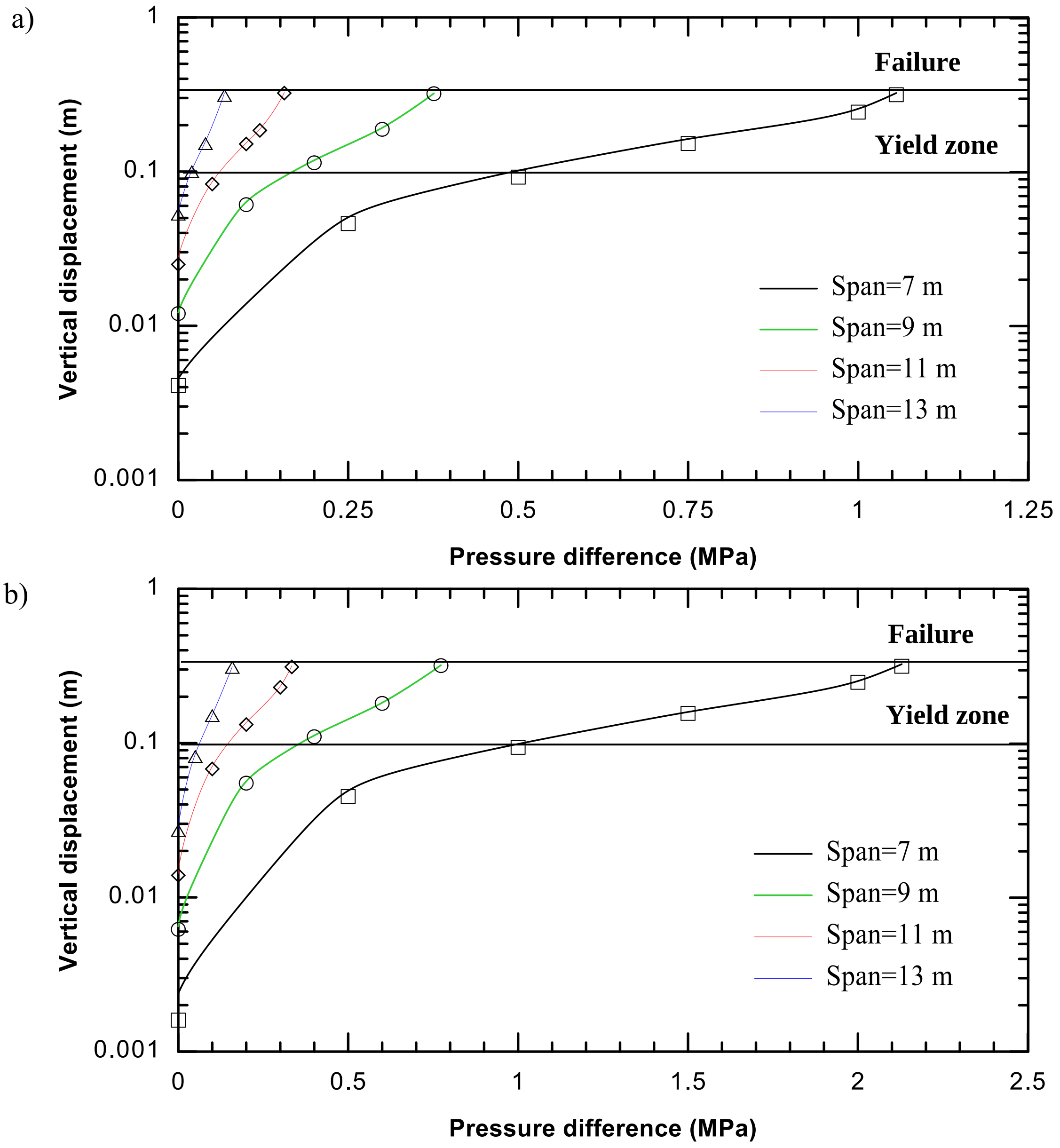

Figure 3.60 Vertical displacement under pressure for unit B (a) and unit A2 (b); modified voussoir beam (solid lines) and UDEC simulations (data points)

Factors of safety against crushing failure are depicted in Figure 3.61. It suggests that the applied pressure can readily create zones of high stress concentration and force crushing at the abutments and mid-span of the beam. As it can be seen, the maximum allowable span for roof beam is noticeably lower than the results of Figure 3.53 and Figure 3.54.

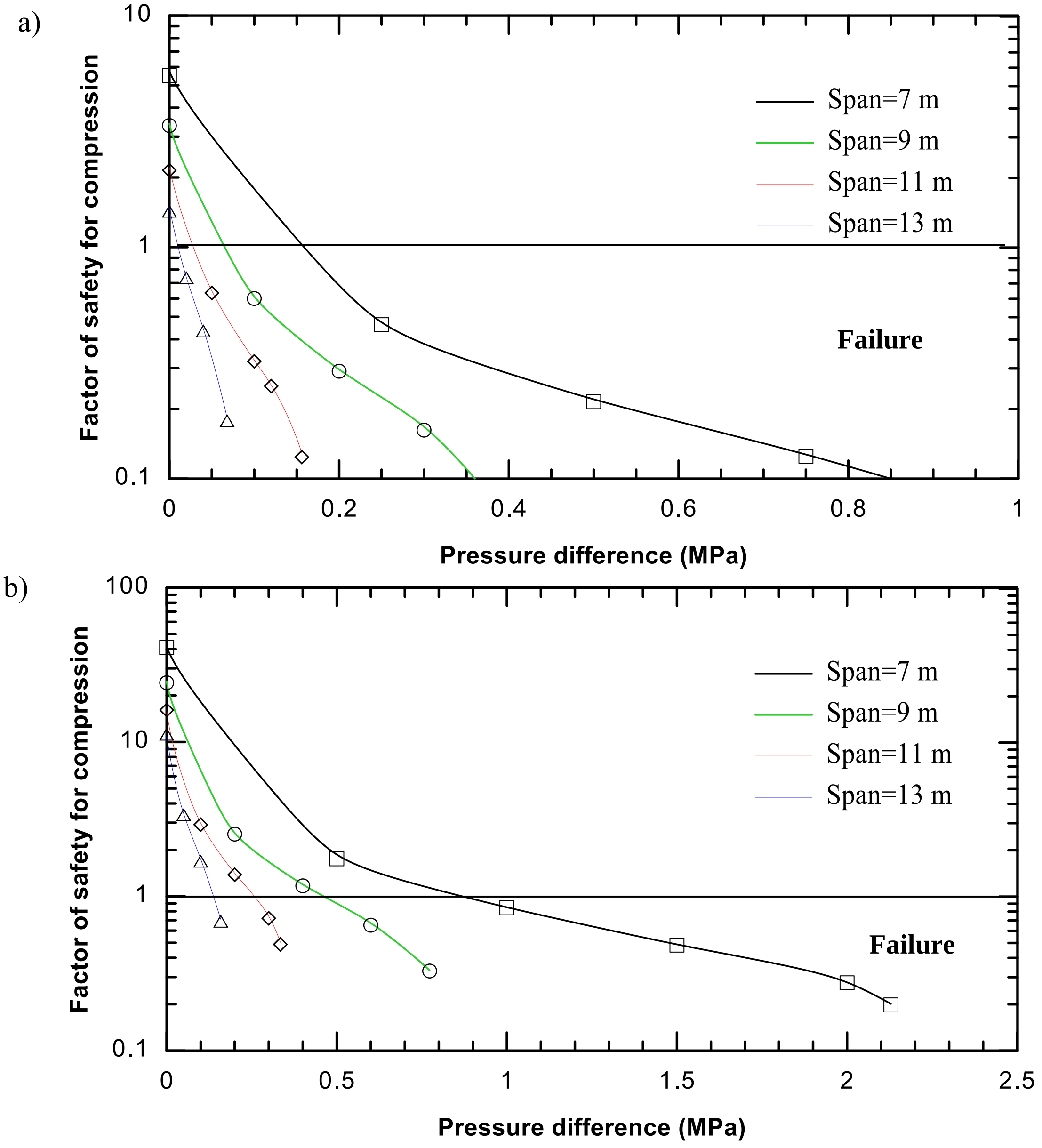

Figure 3.61 Factor of safety against compression under pressure for unit B (a) and unit A2 (b); modified voussoir beam (solid lines) and UDEC simulations (data points)

CHAPTER 4 – Summary and Conclusions

Using an underground cavern for storage of compressed air requires geomechanical analysis to ensure stability and serviceability of the cavern. Gravity driven failures can cause serious stability issues such as roof raveling and casing impairment. Thus, among all geomechanical design parameters, design of the immediate roof beam is of importance. The goal of the research is to model the behavior of the roof layer regarding geometrical and mechanical properties and to predict stability/instability of the beam against different failure modes.

Chapter 1 discussed the concept of CAES systems and focused on the geomechanical aspect of the technology. Site selection criteria and suitable geological formations in south-western Ontario were introduced. Unit A2 and unit B salt beds of the Salina Formation in Sarnia and Goderich were selected as potential sites for CAES plant in south-western Ontario. The Q-index is used to calculate rock mass modulus of the selected beams. Chapter 2 summarized the analytical methods for modeling of rock mass behavior. Voussoir beam theory was presented and the experimental, analytical and numerical analyses published by other researchers were highlighted. Concepts and assumptions of the voussoir method were discussed and the main conclusions of previous investigations were taken into account. Also, a detailed statics and formulation of the selected approach was presented in this chapter.

Chapter 3 introduced the characteristics of the developed model. The developed computer program was verified against results of other researchers. A Universal Distinct Element Code (UDEC) was generated to investigate the accuracy of the inherent assumptions in this method. The existing voussoir beam method is modified based on the numerical simulations. Mechanical response of the roof rock was assessed and the values of factors of safety were calculated for different span to thickness ratios and rock mass properties. Also, surcharge and cavern inside pressure on the response of the roof beam was analyzed. Since the presented method was simplified by assuming linear stress distribution, a nonlinear approach was implemented to improve the results. Finally, feasibility of adding inelastic deformation of the beam to the voussoir beam solution was examined.

Despite the accuracy of the analytical results in predicting the deformation, values of compressive stress at the abutments are not consistent with numerical models. Voussoir method considers a linear and identical stress distribution at both abutments and mid-span. In addition, the values of normal thickness of compressive zone at the abutments are set to be equal. The oversimplification of the method led to average error of 46.7%. Numerical analysis illustrated that lateral stresses at abutments form a nonlinear distribution, while a linear assumption is accurate at the middle of beam. It was also found that the compressive zone at mid-span is 1.5 times thicker than that at the abutments. Therefore, stress distribution at the abutment has been modeled using a second order polynomial with less normal thickness value. These modifications drop the average error of axial stress to below 3%.

The voussoir beam method has been widely used for design of underground openings; however, some guidelines must be noted when voussoir results are used for decision making. Numerical models showed that the deformation predicted by the voussoir method is fairly accurate and the error decreases as span/thickness values increase. Investigation of the mechanical response of the unit thickness roof beam under gravitational load demonstrated that maximum allowable span for unit B and unit A2 cap rock layers is $18.07\ m$ and $21.24\ m$, respectively. It must be noted that the values that have been selected for some of the input parameters with no field data are chosen in a way to ensure reliability of the stable zone. Moreover, inherent assumptions in the solution lead to conservative results. Therefore, a roof beam with span of less than $18.07\ m$ for unit B and $21.24\ m$ for unit A2 cap rock layers is certainly stable against snap-through failure; however, instability of beams with spans of greater than the upper limits is not certain.

The lower limit for span/thickness ratio is determined by factor of safety against sliding failure because less axial thrust would be applied at the abutments of low span beams, which leads to slip at the abutments. The limit for factor of safety is theoretically set to one; however, numerical models in this study show that the voussoir method underestimates the lower limit for this factor of safety. Therefore, the value of 1.9 is considered as failure limit of factor of safety against sliding. This leads to a minimum allowable span of $5\ m$ for both unit B and A2 rock masses.

Failure due to compression at zones of high stress concentration is not an issue for roof beams in unit A2 rock mass. Due to high strength of the material, this criterion does not affect the allowable range of span/thickness ratio determined by other failure mechanisms. Unit B rock mass is not as strong as unit A2. Thus crushing failure occurs at spans greater than $15\ m$ for roof beams in this medium.

When formation pressure is greater than the cavern inside pressure, the behavior of the roof beam is strongly dependent on the rock mass modulus, E, and span/thickness ratio of roof beam. This condition occurs when air has been withdrawn and cavern is in the mode of minimum internal pressure. Depending on the depth of cavern in each site, the maximum pressure difference can take a value from $0.93\ MPa$ for unit B in Goderich to $2.4\ MPa$ for unit A2 in Sarnia. Considering the extreme condition, the stable span cannot exceed $7\ m$ in unit B and $8\ m$ in unit A2 cap rock layers. It can be concluded that if air and formation water transmission is not possible through cap rock, then snap-through and crushing failures most likely will occur while no sliding is expected.

On the other hand, when air has been injected into the cavern, it acts as a support pressure which boosts stability by decreasing the deformation; however, there is a limit for this effect. When pressure difference is greater than the product of the unit weight of material and beam thickness, then the compressive zone within the beam shrinks and gradually the entire beam goes under tensile stresses. This is likely to occur when the cavern is in the mode of maximum internal pressure. In this condition, the obtained axial stress is negative. Since rock mass has zero tensile strength, any applied stress leads to initiation of new joints and cracks or extension of previous joint sets.

Since the immediate roof beam of salt caverns may contain evaporites, creep deformation of the roof rock has been added to elastic deformation analysis. Investigation of the creep response of the roof beam under gravitational load displayed vertical displacement of less than $0.9\ mm$ over ten years. This is a small value in comparison with instantaneous deformation of the beam (which is about $19\ mm$ for unit B and $10\ mm$ for unit A2). Thus, it is concluded that the creep behavior does not affect stability of the roof beam.

The major outcomes and contributions of the study are summarized in the following

- The unit B and unit A2 salt beds in Salina Formation are suitable for compressed air storage as long as the guidelines regarding stability analysis are considered in the design process. The maximum and minimum allowable span of cavern roof layer is limited by snap-though and sliding failures, respectively.
- A roof with low rock material strength and relatively high span/thickness ratio is likely to fail by crushing and spalling at abutments and mid-span.
- The lower limit of roof span obtained from voussoir method is not accurate. Based on the findings from numerical analyses, a threshold of 1.9 for factor of safety against sliding ensures the stability/instability of all roof beams.
- The cavern inside pressure improves the roof stability as long as pressure difference around the roof is lower than the multiplication of the material unit weight and beam thickness; otherwise, it would impose tensile stresses and leads to fracturing of the rock mass.
- Load bearing capacity of the roof beam depends on the generation of a compressive arch within the beam. It has been found that the thickness of the arch is not constant, as the compressive zone at mid-span is thicker than the abutment while the maximum axial stress at the abutment is higher than the mid-span.
- Axial stress distributions at the abutments follow a nonlinear pattern. Since linear stress assumptions oversimplify the model, a nonlinear solution is developed to model the stress distribution, which significantly enhanced the accuracy of results.
- The cavern cannot be completely empty, as the presence of formation pressure on top of the roof layer causes significant pressure difference which leads to roof

collapse. This response of the beam strongly depends on the rock mass modulus; however, no discernible correlation has been found.

- Creep deformation of the roof rock is very small. Thus it can be ignored in design process of the cavern.

REFERENCES

Al-Ajmi, A.M., Zimmerman, R.W., 2006. Stability analysis of vertical boreholes using the Mogi–Coulomb failure criterion. International Journal of Rock Mechanics & Mining Sciences, 43, 1200 –1211.

Bakun-Mazor, D., Hatzor, Y.H., Dershowitz, W.S., 2009. Modeling mechanical layering effects on stability of underground openings in jointed sedimentary rocks. International Journal of Rock Mechanics and Mining Sciences, 46(2), 262-271.

Barker, R.M., Hatt, F., 1972. Joint effects in bedded formation roof control. New Horizons in Rock Mechanics, Proc. 14th U. S. Symp. Rock Mech., University Park (eds H. R. Hardy and R. Stefanko), 247–61.

Barton, N., 1995. The influence of joint properties in modeling jointed rock masses. In: Proceedings of the 8th international congress on rock mechanics, Tokyo, Japan, p. 1023–1032.

Barton, N.R., Lien, R., Lunde, J., 1974. Engineering classification of rock masses for the design of tunnel support. Rock Mech. 6(4), 189-239.

Beer, G., Meek, J.L., 1982. Design curves for roofs and hanging walls in bedded rock based on voussoir beam and plate solutions. Trans. Inst. Min. Metall., 91, A18-22.

Brady, B.H.G., Brown, E.T., 1985. Rock Mechanics for Underground Mining. 1st edn. Allen & Unwin: London.

Brady, B.H.G., Brown, E.T., 2004. Rock mechanics: For underground mining. Kluwer Academic Publishers.

Bucky, P.B., Taborelli, R.V., 1938. Effects of immediate roof thickness in longwall mining as determined by barodynamic experiments. Trans Am. Inst. Min. Metall., 130: 314–32.

Capes, G.W., 2009. Open stope hangingwall design based on general and detailed data collection in rock masses with unfavorable hangingwall conditions. PhD thesis, University of Saskatchewan, Saskatoon.

Diederichs, M.S., Kaiser, P.K., 1999a., Stability of large excavations in laminated hard rock masses: The voussoir analogue revisited. International Journal of Rock Mechanics and Mining Sciences, 36(1), 97-117.

Diederichs, M.S., Kaiser, P.K., 1999b. Authors' reply to discussion by A. I. Sofianos on "Stability of large excavations in laminated hard rock masses: the voussoir analogue revisited". Int. J. Rock. Mech. Min. Sci., 36(7), 995–7.

Diederichs, M.S., Kaiser, P.K., 1999c. Tensile strength and abutment relaxation as failure control mechanisms in underground excavations. International Journal of Rock Mechanics and Mining Sciences, 36, 69-96.

Dusseault, M.B., Fordham, C.J., 1994. Time-dependent behavior of rocks. In J. A. Hudson (Ed). Comprehensive rock engineering: principles, practice, and projects (pp. 119-149). Pergamon Press.

Düsterloh, U., Lux, K.H., 2010. Some geomechanical aspects of compressed air energy storage (CAES) in salt caverns. Solution Mining Research Institute. Leipzig, Germany.

Ege, J.R., 1984. Formation of solution-subsidence sinkholes above salt beds: U.S. Geological Survey, Circular 897, 11 p.

Evans, W.H., 1941. The strength of undermined strata. Trans. Inst. Min. Metall., 50, 475-500.

Fayol, M., 1885. Sur les mouvements de terrain provoques par l'exploitation des mines. Bull. Soc. L'Industrie Minerale, 2nd Series, 14: 818.

Goodman, R.E., 1989. Introduction to rock mechanics. 2nd edition, John Wiley & Sons., pp. 257-280.

Grieve, R.O., 1955. Leaching of Silurian salt beds in southwestern Ontario as evidenced in wells drilled for oil and gas. C.I.M.M. Trans., Vol. LVIII, pp. 10-16.

Hansen, F.D., Kuhlman, K.L., Sobolik, S., 2016. Considerations of the differences between bedded and domal salt pertaining to disposal of heat-generating nuclear waste. Sandia National Laboratories. Sandia, USA.

Hatzor, Y.H., Benary, R.,1998. The stability of a laminated voussoir beams: back analysis of a historic roof collapse using DDA. Int. J. Rock. Mech. Min, Sci., 35(2), 165-181.

Hewitt, D.F., 1962. Salt in Ontario. Industrial Mineral Report No. 6, Ontario Department of Mines, Toronto, ON.

Hoek, E., Brown, E.T., 1980a. Empirical strength criterion for rock masses. J. Geotech. Eng. Div., ASCE 106 (GT9), 1013-1035.

Hoek, E., Brown, E.T., 1980b. Underground Excavations in Rock, London. Instn. Min. Metall.

Hu, C., 2016. Investigation and application of voussoir beam theory for the stability evaluation of underground excavations. PhD thesis, University of Alberta, Canada.

Hydrostor Inc. & NRstor Inc. announce partnership to develop advanced compressed air energy storage projects across Canada. (2017, March 28). Retrieved from http://www.nrstor.com/daily-digest/

Intera Engineering Ltd., 2011. Descriptive geosphere site model. (NWMO DGR-TR-2011-24). Kincardine, ON: Ontario Power Generation.

Itasca Consulting Group., 2010. Universal Distinct Element Code (Version 5.00) [Computer software]. Minneapolis, Minnesota, USA.

Landes, K.K., 1945a. The Salina and Bass Island rocks in the Michigan basin. U.S. Geol. Surv., prelim, map. No. 40 (Oil and Gas Investigation Series).

Nomikos, P.P., Sofianos, A.I., 2011. An analytical probability distribution for the factor of safety in underground rock mechanics. International Journal of Rock Mechanics & Mining Sciences, 48, 597–605.

Obert, L., Duval, W., 1967. Rock mechanics and the design of structure in rock. John Wiley & Sons, Inc.

Passaris, E., Ran, J., Mottahed, P., 1993. Stability of the jointed roof in stratified rock. International Journal of Rock Mechanics and Mining Sciences & Geomechanics Abstracts, 30(7), 857-860.

Ran, J., Passaris, E., Mottahed, P., 1994. Shear sliding failure of the jointed roof in laminated rock mass. Rock Mechanics and Rock Engineering, 27(4), 235-251. doi:10.1007/BF01020201.

Sepehr, K., Stimpson, B., 1988. Roof deflections and sag in jointed, horizontally bedded strata – a numerical study. Rock Mechanics and Rock Engineering, 21, 207-218.

Shabanimashcool, M., 2012. Numerical modelling of the longwall mining and the stress state in Svea Nord Coal Mine. PhD thesis, NTNU, Trondheim.

Sofianos, A.I., 1996. Analysis and design of an underground hard rock voussoir beam roof. Int. J. Rock Mech Min. Sci. & Geomech. Abstr., 33(2), 153–66.

Sofianos, A.I., 1999. Discussion on "Stability of large excavations in laminated hard rock masses: the voussoir analogue revisited" by M. S. Diederichs and P. K. Kaiser, Int. J. Rock Mech. Min. Sci., 36(7), 991–3.

Sofianos, A.I., Kapenis, A.P., 1998. Numerical evaluation of the response in bending of an underground hard rock voussoir beam roof. Int. J. Rock Mech. Min. Sci., Vol. 35, No. 8, pp. 1071-1086.

Sterling, R.L., 1980. The ultimate load behaviour of laterally constrained rock beams. The State of the Art in Rock Mechanics, Proc. 21st U. S. Symp. Rock Mech., Rolla (ed. D. A. Summers), 533–42. University of Missouri: Rolla.

Sterling, R.L., Nelson, C. R., 1978. An experimental investigation of the ultimate strength of laterally constrained rock beams. SESA Spring Meeting, Dallas, TX.

Stimpson, B., 1989. Ultimate collapse of cross-jointed, thinly bedded, horizontal roof strata. International Journal of Mining and Geological Engineering, 7, 127-146.

Succar, S., Williams, R.H., 2008. Compressed air energy storage: theory, resources, and applications for wind power. Princeton Environmental Institute. Princeton University.

Technology Insights & EPRI PEAC Corporation., 2003. Handbook of Energy Storage for Transmission & Distribution Applications. (1001834). Palo Alto, CA: EPRI and Washington, DC: U.S. Department of Energy.

Wright, F.D., 1972. Arching action in cracked roof beams. Proc. 5th Int. Strata Control Conf., London, Pre-print 29.

Wright, F.D., 1974. Design of roof bolt patterns for jointed rock. (USBM Grant Final Report). College of Engineering, University of Kentucky, USA: National Technical Information Service, Springfield, Va.

Wright, F.D., Mirza, M. B., 1963. Stress distribution around a vertical crack in a mine roof beam. Trans. A.LM.E. 226, 174-179.

APPENDIX I – Length of Compressive Arch Line

Figure I.1 shows the arch line within voussoir beam in a Cartesian coordinate. The origin of the coordinate is located at intersection of the reaction line and mid-span joint.

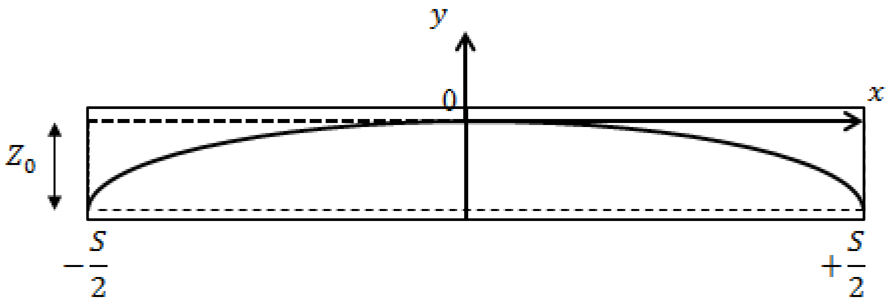

Figure I.1 Parabolic arch line in Cartesian coordinate

The arch line is assumed to form a parabolic curve

$$y = ax^2 + bx + c \tag{I.1}$$

when $x = 0$ and $y = 0$

$$c = 0 \tag{I.2}$$

when $x = \frac{s}{2}$ and $y = -z_0$

$$a(\frac{s}{2})^2 + b(\frac{s}{2}) = -z_0 \tag{I.3}$$

when $x = \frac{-s}{2}$ and $y = -z_0$

$$a(\frac{-s}{2})^2 + b(\frac{-s}{2}) = -z_0 \tag{I.4}$$

Combining equations (I.3) and (I.4)

$$b = 0 \tag{I.5}$$

$$a = \frac{-4z_0}{s^2} \tag{I.6}$$

Replacing equations (I.2), (I.5) and (I.6) into equation (I.1) gives

$$y = \frac{-4z_0}{s^2}\ x^2 \tag{I.7}$$

The length of function $y(x)$ from a to b can be determined by

$$L = \int_a^b \sqrt{1 + {y'_{(x)}}^2}\ dx \tag{I.8}$$

Thus

$$L = \int_{\frac{-s}{2}}^{\frac{s}{2}} \sqrt{1 + 4a^2x^2}\, dx = 2\ \int_0^{\frac{s}{2}} \sqrt{1 + 4a^2x^2}\, dx \tag{I.9}$$

Let's assume

$$u = arc \sinh(2ax) \tag{I.10}$$

Then

$$x = \frac{1}{2a}\ \sinh(u) \tag{I.11}$$

And

$$dx = \frac{1}{2a}\ Cosh(u)du \tag{I.12}$$

Using trigonometric identities

$$cosh^2x - sinh^2x = 1 \tag{I.13}$$

$$cosh^2 x = \frac{1+\cosh 2x}{2} \tag{I.14}$$

$$\sinh(2x) = 2\sinh x \,.\, \cosh x \tag{I.15}$$

$$\cosh\,(\text{arcsinh}\, x) = \sqrt{1+x^2} \tag{I.16}$$

and replacing equations (I.11) and (I.12) into (I.9) and using equation (I.13)

$$L = \frac{1}{a}\int cosh^2(u)\, du \tag{I.17}$$

Using equation (I.14)

$$L = \frac{1}{2a}\int (1+\cosh 2u) du \tag{I.18}$$

By calculating the integral

$$L = \frac{1}{2a}\left[u + \frac{1}{2}\sinh 2u\right] \tag{I.19}$$

Using equation (I.15) gives

$$L = \frac{1}{2a}[u + \sinh u \,.\, \cosh u] \tag{I.20}$$

Replacing equations (I.9) and (I.10) into equation (I.20)

$$L = \frac{1}{2a}[\, arc\sinh(2ax) + (2ax).\,(\cosh(arc\sinh(2ax)))\,] \tag{I.21}$$

Using Taylor series

$$arc\sinh(2ax) = 2ax - \frac{4}{3}a^3x^3 + \cdots \tag{I.22}$$

Replacing equation (I.22) into (I.21) and using equation (I.16)

$$L = \frac{1}{2a}\left[2ax - \frac{4}{3}a^3x^3 + 2ax.\sqrt{1 + 4a^2x^2}\,\right] \qquad \textbf{(I.23)}$$

By simplification

$$L = x - \frac{2}{3}\,a^2x^3 + x\sqrt{1 + 4a^2x^2} \qquad \textbf{(I.24)}$$

Using Taylor series

$$\sqrt{1 + 4a^2x^2} = 1 + 2a^2x^2 + \cdots \qquad \textbf{(I.25)}$$

Replacing equation (I.25) into equation (I.24)

$$L = (2x + \frac{4}{3}\,a^2x^3)|\begin{matrix}\frac{s}{2}\\ 0\end{matrix} \qquad \textbf{(I.26)}$$

Then

$$L = s + \frac{1}{6}a^2s^3 \qquad \textbf{(I.27)}$$

Replacing equation (I.6) into equation (I.27), gives the final formula for length of the arch line within the beam

$$L = s + \frac{8}{3s}\,{Z_0}^2 \qquad \textbf{(I.28)}$$